Multi-element air-coupled capacitive ultrasonic transducer with dynamic focusing for non-destructive testing of materials : modelling, numerical simulations and experiments

Di Zhang

N° d'ordre : 4893

Thèse

présentée à

L'Université Bordeaux 1

ÉCOLE DOCTORALE DES SCIENCES PHYSIQUES ET DE L'INGÉNIEUR

par **Di ZHANG**

POUR OBTENIR LE GRADE DE

DOCTEUR

SPÉCIALITÉ : **Mécanique et Ingénierie**

Transducteurs ultrasonores capacitifs multiéléments à couplage air pour un contrôle non destructif à focalisation dynamique de matériaux – Modélisation, simulations numériques et expériences

---

Soutenue le : 20 Novembre 2013

Après avis de :

M. D. Cassereau, Maître de conférences (HDR), Université Pierre et Marie Curie	**Rapporteur**
M. D. Certon, Maître de conférences (HDR), Université Francois Rabelais	**Rapporteur**

Devant la commission d'examen formée de :

M. M. Deschamps, Directeur de recherche CNRS, Université de Bordeaux	**Président**
M. M. Castaings, Professeur, Université de Bordeaux	**Directeur de thèse**
M. D. Cassereau, Maître de conférences (HDR), Université Pierre et Marie Curie	**Examinateur**
M. D. Certon, Maître de conférences (HDR), Université Francois Rabelais	**Examinateur**
M. M. Rénier Maître de conférences, Université de Bordeaux	**Invité**

- 2013 -

Acknowledgements

The work presented in this thesis would not have been possible without the foresight, supervision, collaboration, and support of many people. They together have made my life at Bordeaux an educational, enjoyable, meaningful and exceptional experience.

Firstly, my great appreciate is to my supervisor, Prof. Michel Castaings, from the Ultrasons Matériaux(UM) group of Departement Acoustique Physique, Institut de Mécanique et d'Ingénierie(I2M-APy) at Université Bordeaux 1, for giving me the opportunity to study the mathematics and physics method behind ultrasonic NDT technology and for teaching me the scientific research method expected at Ph.D. level. Since I arrived Bordeaux 3 years ago after the closure of Master's study at Tongji University in Shanghai, I have studied from him to develop the air-coupled capacitive array for NDT application. He taught me how to operate the experiment instrument, how to design an experimental system for certain purpose. He also taught me how to set the numerical simulation condition then check and validate the model carefully. We worked together to finish the project. He has both exhibited great enthusiasm in driving my results forward and got me to accomplish further with well organized plans. Through the striving on this project, I get not only the corresponding knowledge in acoustic, physics and mathematics, but also fully aware the procedures to organize a research project and to work with a team. I would like to express my great appreciation for his support, patience, understanding, and responsiveness during my time at I2M. I believe that I would be happy to recall this research duration with him years after.

I would like to thank to the reviewers of the manuscript of the thesis: Dr. Didier Cassereau, from Laboratoire d'Imagerie Paramétrique(LIP) of Université Pierre et Marie Curie; Dr. Dominique Certon, from Groupe de Recherche en Matériaux, microélectronique, Acoustique, Nanotechnologies(GREMAN) of Université Francois Rabelais. They had reviewed the manuscript of the thesis carefully and pose many valuable questions to help to improve the thesis. My gratitude is to them for accepting the invitation to be the jury members of the defense.

This thesis would be dedicated to the late UM team director Prof. Bernard Hosten who had initiated the work on MEACUT (Multi-Element Air-coupled Capacitive Ultrasonic Transducer). I would like to thank Dr. Mathieu Rénier. As a member of UM team and a young lecturer in the University, he spent a lot time on supporting my thesis both in experiment and numerical simulations. He is a researcher with whom people is comfortable to talk and collaborate. His diligent work and smart ideas to solve problems impress me and further inspire me. I also give him my gratitude for his company in the lab when it is already very late in the evening. And I send my best wishes for him to keep fit. I would like to thank other group member of UM who kindly supply so many help during this project: Prof. Christophe Bacon, for his help in numerical model building and a lot of mathematical guidance in mechanical problems; The I2M engineer Christine

Biateau, for her help in experimental system building and fabrication of MEACUT; Prof. Philippe Micheau, Professeur of l'Université de Sherbrooke in Canada, during his stay in the lab he gave me lots of instruction in the field of SHM (Structure Health Monitoring) and helped me to operate and use Lecœur system; Prof. Marc Deschamp, former director of LMP (Laboratoire de Mécanique et Physique), for giving me some advice in Acoustics and caring the progress of my thesis. My special thankfulness to him to accept the invitation to be examinateur of the thesis and to the president of the denfense jury. I would like to thank all faculty, lecturers and engineers, I2M members of all teams and groups, who have given me help especially other former and current members of UM team that I have not yet mentioned, with whom I have had many useful talks: Anissa Meziane, Thomas Brunet, *et.al.* Also my thanks is to Beatrice Desoudin, Sandrine Guit, Jeremy Guitard and Cathy Blanchard for their concerns and help in the living affairs at Bordeaux.

I would like to present my special appreciation to faculties from Institute of Acoustics in Tongji University where I spent my 3 years of Master study. As a collaborator of I2M lab and my recommender to the lab, we always keep a good contact with Prof. Qian Cheng, who is now a senior researcher in the ultrasonic domain. I give my thanks to her for her kindly concerns on my life abroad and attentions on my study in I2M. As well as Prof. Yongdong Pan, who had given me suggestion and help in experiment as a group collaborator. I would like to reserve my special thanks to Prof. Menglu Qian for his kind concerns and guidance on problems in many acoustic domains. He was my supervisor at Master's step and has retired at present, but he is always my mentor in scholar and life.

This work would not have been possible without the funding provided by the China Scholarship Council as a representative of Chinese government for supporting Chinese young researchers to study and pursue their research worldwide. I would like to thank the personnels in Chinese Embassy in Paris, for their help on my living and assistance to deal with some student affairs at Bordeaux.

I would like to express my gratitude for the great conversations and valuable friendship from other former and current members of I2M, doctors and post-docs, Mohamed Masmoudi, Dilbag Singh, Thierry Kouadio, Julien Chandezon, Samuel Raetz, Samuel Rodriguez, Philippe Blanloeuil, Jérôme Dubois, Abderemane Mohamed Elarif, Maria Korotyaeva, Anton Kucenko, Benjamin Normandin, Allawa Abbas, Maroun Abi Ghanem, Lazhar Omri, Naoufel Ben Salem, Benoit Mascaro, Feng Xu, et al. For the accompany of so many friends, I am glad to have this Ph.D. experience and feel fortune to meet so many interesting people.

Résumé en Français

Transducteurs ultrasonores capacitifs multiéléments à couplage air pour un contrôle non destructif à focalisation dynamique de matériaux – Modélisation, simulations numériques et expériences.

Le contrôle non destructif (CND) de matériaux se développe fortement dans les domaines de l'aéronautique, l'aérospatiale, du transport et autres secteurs industriels, notamment avec l'essor des matériaux composites et les nouveaux procédés d'assemblages tels que, par exemple, le collage de nombreux types de matériaux. Les techniques de CND sont très variées : radiographie ou tomographie X, thermographie, magnétoscopie, ressuage, courants de Foucault, ultrasons, méthodes optiques, etc... Néanmoins, les ultrasons sont particulièrement attractifs pour plusieurs raisons : ils sollicitent mécaniquement le matériau dans lequel ils se propagent et véhiculent donc de l'information sur les caractéristiques mécaniques de ce matériau. Ainsi, en plus de pouvoir détecter et localiser des défauts tels que des fissures, des délaminages, des décollements, des zones de corrosion ou autres endommagements, ils peuvent être utilisés pour évaluer quantitativement les propriétés mécaniques du milieu ; par exemple mesurer un module d'Young, un coefficient de Poisson ou encore des modules de rigidités. On parle alors de caractérisation mécanique non destructive. Les techniques usuellement employées pour la génération et la détection d'ultrasons reposent sur l'utilisation de traducteurs ultrasonores de nature piézoélectrique (PZT). Ces traducteurs sont souvent placés en contact direct avec la pièce et couplés *via* un gel spécifique (à l'instar de traducteurs employés en échographie médicale) ou alors immergés dans de l'eau (cuve à immersion ou jet d'eau) qui assure le couplage acoustique entre ces éléments (un émetteur et un récepteur) et la pièce à inspecter. En effet, l'impédance acoustique de l'air étant très faible devant celle des milieux solides (métaux, polymères, composites, PZT...), le transfert d'énergie acoustique d'un traducteur émetteur vers un traducteur récepteur, *via* une pièce à contrôler, est très faible, ce qui a pour conséquence une réduction du rapport signal sur bruit des signaux analysés. Ce contraste d'impédance acoustique, qui se manifeste non seulement aux interfaces air/pièce à contrôler mais aussi aux interfaces traducteurs/air, est défavorable à la transmission de l'énergie acoustique à travers les interfaces. Néanmoins, les forts progrès en électronique durant les années 90, ou encore en matière de micro-usinage et

micro-assemblage, ont permis d'une part de réduire très significativement les niveaux de bruit des générateurs ou amplificateurs de signaux, et d'autre part d'optimiser la conception des traducteurs ultrasonores à couplage air. Ainsi, depuis une vingtaine d'années, on voit apparaître de réelles solutions techniques pour l'emploi de traducteurs ultrasonores à couplage air dans le domaine du CND. Ils sont très avantageux car ils ne nécessitent pas de contact ou d'immersion. Ainsi, leur utilisation permet de réduire le risque de pollution du matériau, et améliore la procédure de contrôle, qui devient plus simple, plus fiable (du fait de l'excellente reproductibilité des signaux mesurés) et ainsi moins coûteuse à mettre en œuvre.

Diverses technologies de traducteurs ultrasonores à couplage air existent : des éléments piézoélectriques avec couches d'adaptation d'impédance, des éléments piézo-composites (arrangement de tiges piézoélectriques dans une matrice céramique pour un compromis optimal entre efficacité et impédance acoustique modérée) ou encore des éléments capacitifs. Le traducteur idéal doit posséder un rendement élevé, c'est-à-dire produire une forte puissance acoustique lorsqu'une tension lui est appliquée (mode émission) ou à l'inverse délivrer une tension élevée lorsqu'il détecte une pression acoustique donnée (mode réception) ; mais il doit également opérer dans un large spectre de fréquences pour favoriser la diversité des applications de CND, ou encore pour permettre la mesure d'une information riche et optimale. Par exemple, un traducteur large bande peut émettre une impulsion temporelle de courte durée, permettant de bien discerner et bien séparer les divers échos ultrasonores produits au sein d'un matériau, facilitant alors la mesure des temps de vols de ces échos pour une meilleure localisation des diffracteurs (défauts, fond de pièce, etc...) et/ou pour une estimation plus précise des caractéristiques mécaniques du milieu de propagation. Il permet également de régler la fréquence des ultrasons envoyés à une valeur correspondant à une fréquence de résonance du milieu inspecté, pour obtenir une donnée précise. L'étendue de la bande passante de traducteurs est donc un paramètre important dans le domaine du CND. Lors d'études antérieures, les éléments capacitifs se sont révélés être les capteurs ultrasonores à couplage air possédant les bandes fréquentielles les plus larges. Par contre, ils possèdent généralement des rendements un peu plus faibles que les traducteurs à base de matériaux piézoélectriques. Ces derniers présentent en outre l'avantage de pouvoir être déclinés en capteurs plans ou focalisés alors que la mise en œuvre de transducteurs capacitifs concaves est plus délicate, comme cela a été mis en évidence dans certains articles. Afin d'obtenir des faisceaux acoustiques focalisés, une alternative consiste à utiliser des transducteurs multiéléments. Un transducteur multiéléments est un capteur constitué de plusieurs éléments actifs. A l'aide d'une électronique multivoies, un signal d'excitation différent peut être appliqué à chacun des éléments. Ainsi, en retardant les signaux d'excitation de certains éléments par rapport aux autres, il est possible de synthétiser un faisceau acoustique focalisé analogue à celui que peut émettre un transducteur concave. L'intérêt des systèmes multiéléments est que ces signaux d'excitation étant modifiables d'un tir ultrasonore à l'autre, il est possible

de focaliser le faisceau à différentes profondeurs. Ce type de transducteurs, initialement développé pour l'échographie médicale, est depuis quelques années de plus en plus utilisé pour le CND des matériaux. A l'heure actuelle, cette technologie concerne essentiellement les transducteurs piezoéléctriques utilisés au contact ou par immersion.

L'objectif de cette étude est donc le développement d'un transducteur ultrasonore à couplage air possédant une large bande passante en fréquence, un rendement élevé et pouvant être facilement focalisé, pour permettre son emploi dans un contexte très large de CND. Pour atteindre ce but, une sonde capacitive et multiélément a été mise au point, fabriquée et caractérisée. La sonde consiste en un arrangement concentrique d'éléments capacitifs entourant un disque central. Dans toute la thèse, cette sonde est notée MEACUT pour *Multi-Element Air-coupled Capacitive Ultrasonic Transducer*. Avant de la fabriquer, un modèle basé sur l'intégrale de Kirchhoff (notée KIM pour *Kirchhoff Integral Model*) est utilisé pour prédire le champ de pression acoustique (satisfaisant l'équation de Helmholtz) généré dans l'air par un disque, à partir du potentiel des vitesses en surface de ce disque. En se servant de la symétrie de révolution axiale des traducteurs (mono ou multi éléments, notés respectivement ACUT ou MEACUT), une intégrale simple de Kirchhoff (réduction de l'intégrale double de Kirchhoff traditionnelle) est employée et résolue en coordonnées cylindriques. Son expression courante contient une singularité numérique qui peut causer la discontinuité de la pression acoustique calculée dans le domaine. Une seconde expression de l'intégrale de Kirchhoff, moins courante mais supprimant cette singularité gênante, est alors utilisée. Dans ce modèle, le phénomène d'absorption des ultrasons dans l'air est pris en compte en considérant un nombre d'onde complexe dans les paramètres de calculs. La partie imaginaire de ce nombre d'ondereprésente le coefficient d'absorption des ultrasons.

Traditionnellement employé pour calculer le champ de pression acoustique rayonné par un traducteur circulaire et mono-élément, le modèle intégral est utilisé par prédire le champ de pression rayonné par une source constituée d'un ensemble d'anneaux concentriques avec un disque central. Ce champ de pression est calculé en utilisant le principe de superposition. Cette méthode, très simple, permet d'obtenir le champ rayonné par un des anneaux en soustrayant les champs de pression rayonnés par deux disques concentriques. Ainsi, la pression acoustique produite par un traducteur multiélément analogue à celui imaginé peut être simulée. Des lois de retard bien spécifiques peuvent alors être appliquées à chacun des éléments, de manière à démontrer la possibilité d'une focalisation dynamique (variable suivant la loi de retard choisie). Elles sont définies dans le domaine des fréquences ; ce sont donc des déphasages proportionnels aux retards temporels nécessaires pour faire converger l'ensemble des champs produits par les éléments, vers un point commun dans l'air. Pour valider la pression acoustique prédite par la méthode KIM, un modèle de champ rayonné par un piston circulaire, basé sur la méthode des éléments finis (modèle axisymétrique lui même consolidé par ailleurs), est construit. Les distributions axiales et latérales de la pression acoustique, obtenues par les deux modèles (KIM et FEM)

sont en très bon accord. Le principe de superposition et son application pour prédire les champs acoustiques produits par un ou plusieurs anneaux sont également validés, démontrant ainsi le potentiel de la méthode KIM pour simuler rapidement (1.5 à 15 fois plus rapide qu'un modèle FEM axisymétrique, selon le cas à traiter) le champ acoustique produit dans l'air par un MEACUT, même pour des grandes distances de propagation. Par la suite, une validation complémentaire *via* des mesures expérimentales est effectuée.

Les champs produits par les sondes multi éléments présentent, dans le cas général, des lobes latéraux secondaires (appelés « lobes de réseaux ») d'amplitude non négligeable et qui peuvent induire des artefacts peu souhaitables dans le cadre d'un contrôle par ultrasons. En effet ces faisceaux parasites peuvent nuire à l'analyse en suggérant la présence de défauts multiples en réalité absents de la pièce contrôlée. De tels lobes de réseaux sont évités lorsque la distance inter éléments est inférieure à la moitié de la longueur d'ondes émise. A l'aide de la technique de fabrication disponible au laboratoire, une telle distance est difficile à obtenir pour des transducteurs à couplage par air (la longueur d'ondes des ultrasons dans l'air est de l'ordre du millimètre aux fréquences des traducteurs utilisés). Une fois validé, l'outil numérique basé sur la méthode KIM est utilisé pour optimiser les caractéristiques de la sonde multiéléments à concevoir. L'objectif est de produire une sonde présentant des propriétés optimales : un transducteur dont les dimensions et le nombre d'éléments sont compatibles avec les applications industrielles, permettant d'obtenir des faisceaux focalisés de grandes amplitudes, présentant des faibles dimensions de la tache focale et des lobes de réseaux dont l'amplitude, suffisamment faible, ne sera pas préjudiciable à l'utilisation de ces sondes. Ainsi, le nombre d'éléments du traducteur, leur taille et leur espacement sont des paramètres qui peuvent être optimisés grâce au modèle KIM.

Une fois réalisé, le prototype MEACUT est alors testé *via* un banc de mesures ultrasonores. Le dispositif expérimental consiste à mesurer le champ acoustique en utilisant un vélocimètre laser couplé à une membrane mince (d'épaisseur $5\mu m$) en polymère placée entre le traducteur source et la sonde laser. Afin de pouvoir cartographier le champ de pression, le traducteur est monté sur un système de déplacement 3 axes. La réponse en fréquence du MEACUT a été mesurée et a révélé une très large bande passante pour ce prototype ($\approx 150\%$ à $-20dB$). Les distributions axiale et radiale du champ ont également été mesurées, et ont confirmé une faible amplitude des lobes latéraux indésirables en regard de l'amplitude du lobe central souhaité. Enfin, en choisissant convenablement la loi des retards pour les signaux d'excitation appliqués à chaque élément du MEACUT, il a été vérifié que la focalisation du MEACUT pouvait être ajustée, permettant alors de parler de traducteur à focalisation dynamique, et que la zone focale était clairement définie, de petite taille (bien plus faible que la largeur d'un faisceau produit par un ACUT ou mono-élément) et avec un niveau de pression supérieur ou égal à celui produit par un ACUT de diamètre équivalent. Les distributions des champs de pression mesurés ont été confrontées aux prédictions numériques de la méthode KIM. Les bons accords obtenus ont confirmé les validations faites par la méthode FEM, et aussi démontré que le prototype

MEACUT avait été convenablement fabriqué et que ses performances étaient en bonne adéquation avec les attentes.

Par ailleurs, dans l'optique de simuler intégralement une expérimentation de CND mettant en jeu les traducteurs ultrasonores à couplage par air, un modèle hybride a été mis en place et employé. Il fait appel à deux méthodes intégrales pour calculer les champs acoustiques dans l'air (la méthode KIM mentionnée plus haut pour prédire le champ entre le traducteur émetteur et la plaque, puis une approche plus générale pour le champ entre la plaque et le traducteur récepteur), et à la méthode des éléments finis pour simuler la propagation dans la plaque. Les conditions de continuité de la vitesse normale, et de la pression dans l'air avec les contraintes en surface de plaque, sont appliquées pour raccorder les trois étapes de calculs. Les méthodes intégrales implémentées dans ce modèle allègent considérablement les ressources et les temps de calculs, par rapport à l'utilisation d'une méthode entièrement numérique, du type éléments finis ou différences finies, par exemple. Le modèle basé sur la méthode des éléments finis (FEM) a été construit pour simuler la propagation ultrasonore au travers d'une plaque placée dans le faisceau généré par le MEACUT. Le logiciel utilisé est *Comsol Multiphysics*. Il permet d'implémenter les équations d'équilibre dynamique et les conditions de frontières souhaitées dans un formalisme très général d'équations aux dérivées partielles (mode PDE). Il offre aussi une grande flexibilité vis-à-vis de la géométrie du domaine à simuler et de son maillage. Ainsi, le modèle développé décrit la propagation d'ondes acoustiques dans une plaque constituée d'un matériau anisotrope et viscoélastique placée dans le vide (compte-tenu de la grande différence d'impédance acoustique entre l'air et la plaque, cette approximation n'engendre qu'une faible erreur sur les champs calculés). Des modules d'élasticité complexes sont employés comme données d'entrée, et les équations sont résolues dans le domaine de Fourier (à une seule fréquence). Le formalisme adopté intègre la définition de régions absorbantes qui atténuent efficacement toute onde s'approchant des bords de la plaque, en augmentant progressivement la viscoélasticité du matériau et en abaissant dans les mêmes proportions sa masse volumique, ce qui permet de maintenir son impédance acoustique la plus constante possible. La plaque ainsi simulée peut être considérée comme infiniment étendue. Le champ de pression acoustique calculé par la méthode KIM, en coordonnées cylindriques, est alors exprimé en coordonnées cartésiennes tridimensionnelles et utilisé pour définir les conditions aux limites. Ainsi, la pression simulée et produite par un traducteur ultrasonore (ACUT ou MEACUT) peut être appliquée localement sur une surface de la plaque, dans le modèle FEM. La résolution du modèle PDE, sous *Comsol*, permet alors de prédire, entre autres, le champ de déplacement résultant en tout point de la plaque. Ainsi, ce champ peut aussi être prédit en surface arrière de la plaque, dans le champ de vue d'un traducteur récepteur qui serait disposé, dans l'air, et dans l'axe du traducteur émetteur.

A partir de la composante normale de la vitesse particulaire associée, ce champ est alors utilisé comme donnée d'entrée d'un second modèle intégral, connu sous le nom

d'intégrale de Rayleigh (RIM pour *Rayleigh Integral Model*), permettant de calculer le champ de pression rayonné dans un fluide par une surface vibrante encastrée dans un baffle rigide. L'air situé derrière la plaque et la rigidité du matériau composant les plaques habituellement inspectées permettent, *a priori*, de satisfaire tout à fait les conditions requises par l'équation intégrale utilisée. Ce modèle RIM à trois dimensions (RIM 3D) provient d'une solution de la fonction de Green satisfaisant l'équation de Helmholtz-Kirchhoff. Les résultats obtenus avec RIM 3D ont tout d'abord fait l'objet d'une phase de validation. Pour cela, un modèle FEM axisymétrique a été construit, comportant une plaque dont une face est couplée à de l'air et l'autre face est totalement libre (couplée à du vide). Une excitation quasi arbitraire a été appliquée sur la face libre de la plaque et la résolution des équations PDE a permis de simuler la pression acoustique produite dans l'air. Par ailleurs, le champ simulé (par ce modèle FEM) des vitesses particulaires produites à la surface couplée à l'air a été relevé, exprimé en coordonnées cartésiennes tridimensionnelles et utilisé comme donnée d'entrée pour le modèle RIM 3D. Ce dernier a alors servi à calculer la pression produite dans l'air, en trois dimensions. Le très bon accord entre les deux jeux de pression ainsi prédits valide le modèle RIM 3D. Dans le cas ou le récepteur simulé est un MEACUT, le champ de pression acoustique peut être calculé dans l'air, et toujours à partir des vitesses normales relevées en surface d'une plaque, au niveau des surfaces des différents éléments (circulaire ou annulaires) supposés constituer ce MEACUT. Des lois de retard doivent alors être appliquées à ces champs localisés ; elles sont choisies en fonction de la distance entre la plaque et ce récepteur, de la vitesse de propagation dans l'air et de la focalisation désirée pour ce MEACUT. De la même manière que pour le MEACUT émetteur qui est simulé avec la méthode KIM, la focalisation peut être variable et ajustée selon les retards appliqués aux divers éléments du traducteur. On parle alors encore de focalisation dynamique, mais cette fois à la réception. Les champs déphasés sont ensuite sommés entre eux, ce qui permet d'établir la pression résultante détectée par le MEACUT récepteur.

Sur la base des travaux décrits précédemment, un modèle hybride KIM-FEM-RIM a été construit, en trois dimensions, en combinant les méthodes intégrales (semi)analytiques de Kirchhoff et de Rayleigh, et la méthode des éléments finis. Ce modèle complet permet de simuler intégralement une expérience utilisée en CND (connue sous le nom de C-scan) afin de repérer la présence de défauts dans une plaque. Dans la configuration dite « par transmission », cette expérience repose sur l'utilisation de deux traducteurs : un émetteur et un récepteur, qui sont placés de chaque côté de la plaque à contrôler. Elle consiste à mesurer l'amplitude du signal transmis à travers la plaque, pour différentes positions du couple émetteur-récepteur. La présence d'un défaut dans une plaque se traduit, lorsqu'il est de dimension suffisamment importante, par une chute de l'amplitude du signal transmis. Une telle expérience permet d'estimer ses dimensions apparentes dans le plan de la plaque, et ainsi d'en apprécier les conséquences sur l'intégrité de la pièce. Le modèle

permettant aussi bien de simuler des traducteurs mono-éléments (ACUT) que multiéléments (MEACUT), deux configurations de contrôle sont simulées et confrontées à des expériences : une première dans laquelle sont utilisés un ACUT émetteur et un ACUT récepteur, et une seconde mettant en jeu un MEACUT émetteur et un ACUT récepteur. Les expériences correspondantes sont réalisées sur une plaque composite (verre polyester) comportant un endommagement causé par un impact, de dimensions apparentes $30mm$ par $18mm$. La plaque est placée entre ces deux traducteurs et perpendiculairement à l'axe les joignant, puis déplacée pas-à-pas perpendiculairement à cet axe de manière à modifier la zone traversée par le faisceau ultrasonore. Dans chaque cas, les deux traducteurs ultrasonores sont disposés face à face et espacés d'une même distance. L'objectif consiste à vérifier si, pour cette application CND, l'emploi d'un traducteur MEACUT comme transmetteur (le récepteur demeurant un ACUT) améliore la résolution spatiale du C-scan, par rapport à l'utilisation classique de deux ACUTs, à quantifier cette amélioration ainsi que le rapport signal-sur-bruit associé. Cet objectif est atteint avec succès ; en effet, l'accroissement des performances du système, en termes de résolution spatiale et de rendement, est clairement démontré puisque le remplacement d'un seul ACUT par un MEACUT permet d'obtenir une image acoustique de la zone endommagée de cotés $40mm$ par $26mm$ au lieu de $80mm$ par $60mm$. Ces résultats sont parfaitement confirmés par les prédictions du modèle hybride KIM-FEM-RIM. La réalisation d'une électronique multivoies dédiée à l'utilisation de récepteurs capacitifs multiéléments est en cours, expliquant la raison pour laquelle seul l'ACUT émetteur a pu être remplacé par un MEACUT. Ces résultats confirment que l'objectif initialement fixé a été atteint, à savoir la modélisation, la simulation numérique, l'optimisation, la fabrication, la caractérisation et l'utilisation d'au moins un capteur ultrasonore à couplage par air, possédant une large bande passante en fréquence, une focalisation efficace et éventuellement variable, et un rendement suffisant pour améliorer une application existante de CND. Le prototype réalisé est un traducteur multiélément dont les performances ouvrent des perspectives prometteuses pour de futures applications de CND.

Contents

Abbreviations

NDT&E	**N**on-**D**estructive **T**esting & **E**valuation
UT	**U**ltrasonic **T**esting
FEM	**F**inite **E**lement **M**ethod
AR	**A**bsorbing **R**egion
PAD	**P**ropagation **A**ir **D**omain
DoF	**D**egree-**o**f-**F**reedom
KIM	**K**irchhoff **I**ntegration **M**ethod
RIM	**R**ayleigh **I**ntegration **M**ethod
PZT	**P**ie**z**oelectric **T**ransducers
SNR	**S**ignal-**N**oise **R**atio
LDV	**L**aser **D**oppler **V**elocimeter
ACUT	**A**ir-**c**oupled **C**apacitive **U**ltrasonic **T**ransducer
cMUT	**c**apacitive **M**icromachined **U**ltrasonic **T**ransducer
MEACUT	**M**ulti-**E**lement **A**ir-coupled **C**apacitive **U**ltrasonic **T**ransducer

Symbols

a	circular radius	mm
d	circular diameter	mm
ρ	material density	$g \cdot cm^{-3}$
C_{ij}	material stiffness tensor	GPa
Z	acoustic characteristic impedance of material	$Rayl$
K_f	bulk module of fluid	GPa
c_0	sound velocity in air	$mm \cdot \mu s^{-1}$
α	sound absorption coefficient in air	$dB \cdot m^{-1} \cdot Hz^{-2}$
$\boldsymbol{n}$	unit vector normal to the boundary	
u	particle displacement in medium	mm
ν	particle velocity	$mm \cdot \mu s^{-1}$
p	sound pressure in fluid	Pa, dB
ϕ	acoustic wave phase in fluid	rad
σ	stress in solid	GPa
j	complex number unit	$\sqrt{-1}$
f	frequency	MHz
ω	angular frequency	$rad \cdot \mu s^{-1}$
k	wave number	$rad \cdot mm^{-1}$

G	Green function
$\Re$	real part operator for complex quantity
$\Im$	imaginary part operator for complex quantity
$\mathcal{F}$	Fourier transform operator

Introduction

Thesis motivation

The motivation of this Ph.D work is the increasing demand of high-performance air-coupled ultrasonic transducers and their use for efficient NDT applications. Meanwhile, the development of an efficient numerical tool is also highly demanded in order to simulate the air-coupled acoustic wave generation, its propagation in the tested solid media and the output signal at the air-coupled receiver. Therefore, this thesis focuses on the promising capacitive air-coupled ultrasonic transducer to build a new type of multi-element transducer, to explore its use for NDT applications, and to develop an analytical-numerical hybrid tool to simulate the whole ultrasonic inspection process.

Thesis context: State-of-the-Art

Numerous non-destructive testing and evaluation (NDT&E) methods [1, 2] have emerged in recent years, involving various domains of Physics, such as X-rays [3], infrared rays [4], heat-transfer [5], magnetic field [6] or ultrasound. The advantage of these methods is that they enable the monitoring of the integrity of structures during their life, without having to destroy them. Through all the NDT methods currently used, ultrasonic NDT has its specific advantages, such as non-radioactive, non-pollution and easy implementation. The application fields of ultrasonic NDT&E are wide and varied. For instance, the aeronautic industry needs to ensure the structural integrity of components used in the manufacturing and usage period of aircrafts [7]. The demand to detect defects in sensible zones so as to avoid accident caused by mechanical failures greatly boosts the development of NDE methods and technologies. Detecting damages or corrosion zones, which may occur in toxic chemicals storage sites, is also important. The preservation in ideal conditions of oil in cylindrical tanks, as well as of nuclear fuels or wastes in concrete containers [8, 9] or in granite caves, requires frequent inspection of the structures containing these chemicals. The transport of materials, which may be dangerous, is also a topic for which the study of the integrity of pipes is required.

Generally, ultrasonic testing is based on the transmission, reflection and absorption of ultrasonic waves (bulk or guided waves) propagating in the tested object. The acoustic wave radiated by the emitter can be reflected or scattered at the defects or at boundaries

with discontinuous properties, then transmitted to the receiving transducers (single or multi-element) [10]. In the light of the acoustic wave used for the inspection process, the ultrasonic NDT could be sorted to testing based on bulk wave [11], shear wave [12], surface wave [13], guided wave [14]. For each wave type, there are specific advantages and drawbacks, and specific flaws that may be detected or not. Each detected ultrasonic signal is a signature, which depends on the interaction between the incident acoustic wave and the defect.

According to the exciting method of the ultrasound in specimen, the NDT method could be sorted to: contact transducer inspection method [15], water coupled transducer inspection [16, 17], laser generated ultrasonic inspection [18–20], Electromagnetic Acoustic Transducer (EMAT) inspection [21, 22], air-coupled transducer inspection [23, 24] *etc.*

The overall performance of an ultrasonic inspection and imaging system is mainly determined by the transducer characteristics. The transferring of acoustical energy from the transducer to the surrounding medium is essential for ultrasonic inspection. At each material boundary the amount of energy transfer is dictated by the acoustic impedances of the two materials [25] at either side of this boundary.

A common method used for ultrasonic inspection [26] is to contact a piezoelectric transducer with a couplant material and place it on the test specimen. The couplant layer needs only have a thickness of one tenth of a wavelength to affect the acoustic properties of the load as seen by the transducer. It is therefore important to choose the couplant on the basis of acoustic impedance as well as taking into account such variables as the viscosity, the acoustic impedances, the ease of removal of the couplant from the specimen surface. The contact transducer has been used in many industry applications [27]. Using the contact method has drawbacks such as the need to maintain a good degree of coupling, the roughness of the sample surface restrictions to the use of couplant, the consideration of contamination of the sample surface by the couplant, *etc.*

Another common method of coupling is to use water, either by use of an immersion tank [28] or by ensuring there is a constant flow of water around the transducer [17]. This testing method allows for automated scanning without wearing on the transducer. The acoustic impedance between the transducer and water or between the water and the tested object could ensure the appropriate energy transferring to the tested material. There are however many materials and industrial manufacture processes where the presence of water will cause damage or inconvenience. In addition the presence of water decreases the possibility of detecting surface flaws in polymer-matrices [29] and internal flaws in porous materials [30]. Materials such as foam, wood, paper products, reinforced plastics, propellants, pieces of art and many materials intended for the aerospace industry are not compatible with water. Thus the restriction of water coupling ultrasonic inspection leads to the research of the possibility and application of air-coupled ultrasonic inspection.

Air-coupled transducer and array

Air-coupled ultrasonic inspection can be considered as a non-contact or minimally-invasive method, because the coupling medium (air or another gas) is part of the natural environment and therefore non additional physical contact is required. Air-coupled ultrasound allows for rapid scanning without damage or contamination to the specimen materials. This non-contact technique could be applied to perform fast on-line inspection. The difficulty with air-coupled ultrasonic inspection lies in the huge acoustic impedance mismatch between the transducer, the air and the tested material, causing very little energy incident into the tested material and thus small signal to noise ratio at the receiver. At the interface between water and steel, approximately 35% of the signal will be transmitted, however between air and steel this figure drops to approximately 0.5% [31]. For a common ultrasonic inspection system, there are four coupling interfaces: that between the transmitting transducer and the air, that between the air and the tested material, that between the tested material and the air, and the interface between the air and the receiving transducer. Thus the design of air-coupled transducers for the detection of signals having small amplitude is essential.

Mostly, there are two types of air-coupled ultrasonic transducers: piezoelectric transducer and capacitive (electrostatic) transducer. The air-coupled transducer follows the similar fabrication method with the contact transducer, which mostly adopts piezoelectric ceramics or composite polymer as the resonance material. The piezoelectric air-coupled ultrasonic transducer (ACUT) system has been developed for decades. Traditional piezoelectric transducers [26] produce ultrasounds based on the piezoelectricity principle, which is the ability of piezoelectric materials to generate mechanical stress in response to an applied electric potential, so to convert electrical energy to mechanical energy. This kind of transducer is not suitable to directly emit ultrasound in air due to the large acoustic impedance mismatch between the transducer and the medium, which leads to a small refraction coefficient and a huge reflection coefficient, and consequently bad efficiency for emission of ultrasound in air. In air, for example, the generation of ultrasound is challenging because the acoustic impedance of air (420 $kg/(m^2s)$, *i.e.* $4.2 \times 10^{-4} MRayl$) is orders of magnitude smaller than the impedance of piezoelectric materials commonly used to excite ultrasonic vibrations (approximately $30 \times 10^6 kg/(m^2s)$, *i.e.* $30 MRayl$). The large impedance mismatch implies that piezoelectric air transducers are inherently low transmitted efficiency. So the application of piezoelectric transducer in air-coupled ultrasonic detection domain usually use a matching layer [25] between the piezoelectric and the air which has a proper thickness and characteristic impedance to increase its efficiency for emission into air.

Recent development of air-coupling piezoelectric transducer (PZT) tend to improve existing piezoelectric ceramic, piezoelectric polymer transducer configurations. For example, the performance of thickness driving piezoelectric ceramic transducers may be enhanced significantly by incorporation of multiple matching layers [32] or the addition

of a radiating membrane to facilitate energy transfer into air. Piezoelectric polymer [33] and piezoelectric ceramic-epoxy composite materials [34] also offer attractive options for airborne ultrasound by means of improved mechanical matching and in the case of the piezoelectric polymers, the ability to be configured as a flexible membrane. A series of 1–3 connectivity piezo-composites [34] transducers has been proposed and revealed good promise applications. The commercial air-coupling PZT and array [35] has been put forward as a promising NDT solution.

However, the improved matching layer solution in air-coupled PZT is inherently problematic for its frequency response performance. The principle of piezoelectric excitation decides the resonance properties, leading to transducers with very narrow frequency bandwidth. This drawback of PZT based air-coupled transducer reduces their field of NDT applications, for example, in the guided wave inspections, wide band acoustic field is required to excite multi Lamb modes. Therefore, the exploration of wide frequency band air-coupled ultrasonic transducer has been carried out for NDT application purposes.

In recent years, some broadband ultrasonic transducers have been developed using PVDF (Polyvinylidene fluoride) transducers as another air-coupled transducer solution. There has been a great deal of development work on ultrasonic devices that take advantage of the inherent properties of piezoelectric polymers [36], that is their relatively good acoustic impedance match to water and tissue, their flexible form and availability in large sheets, their broadband acoustic performance, and the uniform surface displacement across the radiating aperture. The main restrictions to the application of PVDF as a transmitter in air [37] are the relatively low coupling factor and dielectric constant [38], resulting in poor performances.

Air-coupled capacitive transducer [39] can be an alternative solution with advantages and well promising applications for NDT. Air-coupled Capacitive Ultrasonic Transducers (ACUT) have been developed over the last two decades [40], and successfully used for the contact-less inspection of composite structures. At the surface of the capacitive transducer, a metallised polymer membrane is used to reduce the acoustic impedance mismatching problem. There has been significant research interest in the development of these devices, for instance at the universities of Stanford [41], Warwick [42], Rome [43], Madrid [44], Tours [24, 45–47] and Bordeaux [48, 49]. Capacitive Micro-machined Ultrasonic Transducers (cMUTs) [50] have demonstrated significant promise for application in air-coupled NDE, but may suffer from their fragile nature.

The main advantages of capacitive transducers include a very broad frequency bandwidth and a sufficiently high sensitivity for general non-contact NDT [51]. Several manufacturing techniques have been reported, including series of coarse polishing machining V-shaped grooves [52] or circular holes through laser ablation [53], photo lithography [54], or sand blasting [55] so that obtained roughness or cavities at the surface of the metallic back-plate determine the frequency properties of the capacitive ultrasonic transducer. Also, these elements require a few-micron thick membrane deposited on the back-plate,

with metallised external surface. This membrane must be stretched for the transducer to operate, thus producing locally plane wave front and introducing difficulties in allowing the focusing of the ultrasonic beam. Consequently, because they cannot be easily focused, these capacitive elements have low spatial resolution, as a serious drawback for some NDT applications. In order to circumvent this problem, a method has been proposed using a micro-machined Fresnel zone-plate placed in the acoustic field [56]. A flexible back-plate [57] as been developed as an alternative solution, allowing the realization of concave capacitive air-coupled transducers. With micromachining fabrication technology [58] on the silicon back-plate a micro-electromechanical system for cMUT has been developed recently. However, these solutions offer fixed focusing features [59] and as many transducers as intended focusing conditions will be required for satisfying several NDT inspections. As a further development, by assembling several capacitive elements and applying properly phased delays to each of these elements, a wide-frequency band, dynamic-focusing array will be developed in this thesis work.

The limitation of single element transducer in beam controlling and spatial sensitivity promotes the emerge of phased array transducer [60]. A phased array transducer [61] consists of multiple elements, each of which is analogous to a single element transducer, capable of emitting and receiving ultrasonic waves. Ultrasonic arrays offer two key advantages over standard monolithic transducers. Firstly, a particular array is able to undertake a range of different inspections and thus is more flexible than a single element transducer. In fact, an ideal array can generate ultrasonic fields of almost infinite variety. However, they are most commonly used to produce fields similar to those from traditional single element transducers, *i.e.* plane, focused and steered beams. Secondly, most types of array can be used to produce images at each test location. This allows rapid visualisation of the internal of a structure. By controlling the pulsed time of the elements, the beam generated by the array can be electronically focused and steered. These reasons and the flexibility lead the phased arrays becoming more commonly used in ultrasonic non-destructive testing. Ultrasonic phased array transducers have been around for more than two decades, mostly in applications of many medical specialities [62]. Various ultrasonic phased arrays are also introduced in industrial applications [63]. A new ultrasonic technique combining the air-coupled capacitive technique and the phased array concept is introduced in this thesis. Under this research and application context, a new Multi-Element Air-coupled Capacitive Transducer (MEACUT) is proposed in this work.

Acoustic field simulation method

The availability of numerical models that can accurately simulate ultrasonic NDT is a continuous and demanding research topic. Many methods are used for the acoustic field calculation, and they can be classified into analytical methods, numerical methods (finite element method, finite difference method, boundary element method, *etc.*) and hybrid methods.The Finite Element Method (FEM) has been widely used to solve various kinds

of acoustic problems for years [64], due to its ability to handle complicated geometries (and boundaries), inclusion of dissimilar material properties, availability for various physical problems, *etc.*.

As their name suggests analytical techniques resolve problems by implementation of available closed form formulas while FEM employs a discretization of the medium for solving the differential equations governing the problems. The analytical methods to calculate acoustic fields include several methods such as angular spectrum method (ASM) [65, 66], Pencil method [67, 68], Multi-Gaussian beam method (MGB) [69] and Rayleigh Integral Method (RIM) [70, 71], *etc.* For the Rayleigh integration method, closed form formulas considering the shape of the transducer and transmitting condition are mathematically deduced from the general Huygens principle [72, 73]. Despite of this, mostly a regular shaped transducer or acoustic source is demanded to get an efficient mathematical integration formula. In this work, the analytical Rayleigh integral method will be developed and used to solve the ultrasonic NDT problems.

Analytical methods

The analytical integration method is basically Rayleigh integration method (RIM), the conception of which comes from Huygens principle in optics [74]. It resumes that the acoustic field in an arbitrary field point in medium is the integration of all the elements on the source which radiates spherical acoustic wave, which could be represented by a Green source function. This method can be represented that the disturbance of one point in space is the overall integration by spherical wave radiation source elements. For cases with regular shaped source or uniformed surface velocity, the integral formula could be mostly simplifies from double surface integration to single integration. These situations of acoustic field calculation greatly simplify the integration expression and increase the capability of short calculation time. The application of Kirchhoff integral method (KIM) to a disk radiator requires ideally that the acoustic medium vibrates uniformly at the front surface.

Finite element method

The finite element method, which is based on a discretization of the medium area to solve the differential controlling equation and certain boundary conditions, originated from the need to solve complex elasticity and structural analysis problems in civil [75] and aeronautical engineering [76]. The method has been developed for nearly 40 years [77], and has been used in wide range of physical and engineering area, for instance thermology, acoustics, electricity and mechanics. The capability of the FE method to meshing the unsolved area with multi-physical field has boosted its application in field coupling areas [10, 78]. As the development and the advance of computation method and computer capacity grow up, several physical problems which are time-consuming or impossible to

solve had been treated. The precision has been confirmed in various physical domains, however, the low velocity of sound in air and large number of Degrees of Freedom (DoF) have limited the use of FEM for air-coupled ultrasonic NDT simulations [79–81].

The main advantage of the finite elements approach is its capability to simulate the propagation in complex structures, with or without defects [14] and for various shapes of transducers [82] like, for instance, focused transducers or phased arrays. Almost all the acoustic simulation problems encounter the unbounded problem [83] which requires infinite space to avoid reflection from boundaries. Most numerical treatments to reach this purpose include infinite elements [84], absorbing layers [79, 85, 86], local absorbing boundary conditions [87], or boundary integration method [88].

The applications of FE methods in acoustics have boosted various commercial packages such as COMSOL, ANSYS, ABAQUS, MARC, *etc.* It is worth mentioning that most of the commercial packages have interactive user-friendly pre and post-processing tools which greatly increase their flexibility and ease of use. The choice of commercially available FE packages is also motivated by the fact that they enable new solutions to be quickly transferred to industry where these products are already or could easily be available, and where a specific unsupported research code would be difficult to maintain.

The FE package selected and used in this work is COMSOL Multiphysics [78] (formerly known as FEMLAB). The pre and post-processing packages used in this work for analytical calculation of acoustic field analysis is Matlab [89]. The software supports distributed computing with cluster computers, which is indispensable for 3D simulation for plate inspection in this work. For 3D simulations with large number of DoF which are out of the computing capacity with personal computer, the computing cluster Avakas [90] available at Université Bordeaux 1 has been adopted.

Thesis outline

This thesis focuses on the simulation of the acoustic field with numerical methods and their validations, the optimization, designing, fabrication and characterization of MEACUT, the application of this ultrasonic transducer to the NDT plate inspection and the development corresponding hybrid model to simulate the inspection process. In Chapter 1, the theoretical tools have been introduced and deduced for calculating the acoustic field pressure generated by axisymmetric transducers (*i.e.* circular, annular transducers). The numerical tools include the analytical axisymmetrical Kirchhoff integration method (KIM) and the fluid-solid coupling axisymmetric FE model. The analytical KIM model has been compared and validated with numerical FE model. In Chapter 2, the annular MEACUT has been optimized with the KIM model and designed with proper parameters in order to get the desired acoustic profile for further applications. Annular array made up of 8 elements with the same surface area has been fabricated with manufacturing technique of ACUT and characterized using laser Doppler Velocimetry to test its frequency response

and its radiated acoustic field performance. The predictions by KIM model are compared with the characterization results, revealing its capability in the simulation of the acoustic field produced by MEACUT. In Chapter 3, the analytical Rayleigh integration method (RIM) is introduced, developed in 3D cases. This 3D RIM model has been validated with a non-piston excitation axisymmetric FE model. Together, a 3D KIM-FEM-RIM hybrid model is built to simulate the whole process from an axisymmetric transmitter to the receiver in the air-coupled plate through-transmission inspection. In Chapter 4, the built MEACUT is experimentally used for inspection of a composite plate with an impact damage. The through-transmission scanning of the plate is first proceeded with a pair of single element ACUT, and then one transmitting MEACUT with one single element ACUT. The experimental results agree well with the predictions of the 3D KIM-FEM-RIM hybrid model. In the end, a conclusion of this thesis is presented including main contributions and problems, as well as the prospectives and suggestions for the future work.

Chapter 1

Numerical modelling of acoustic field produced by air-coupled transducer

1.1 Introduction

In the air-coupled ultrasonic inspection system, the air-coupled transducer aperture is axisymmetric, either circular or annular. So for decreasing the calculating amount of the acoustic field pressure produced by the air-coupled transducer, an axisymmetric approach will be adopted both for Kirchhoff integration analytical model and FE model. An efficient Kirchhoff integral method (KIM) based on Rayleigh integration method (RIM) is developed for circular and annular transducers. This Kirchhoff model uses a single integral expression to calculate the radiated field by capacitive or piezoelectric transducer in a fluid (air) that greatly simplifies the field calculation process and decreases the calculating time of the NDT system simulation in comparison to the FE model.

As a widely used numerical tool, an axisymmetric FE model is developed for the validation of the analytical method. The building of this axisymmetric FE model mainly includes the following three parts: setting of partial differential equations (PDE) formalism and boundary conditions according to the COMSOL formalism [78] which will be described further down; construction of the geometry and meshing to realise the discretization of the domains; properly setting of the absorbing region.

1.2 Kirchhoff integration method for axisymmetric transducer

The starting point for modelling of the acoustic fields radiated by transducer or scattering objects is the development of integral expressions. On geometrical aspect, the transducers used in this work are either circular or annular. To simulate the acoustic field pressure produced by these transducers, the axisymmetric integral model either for circular or for annular transmitter will be built analytically in the following sections. The

Kirchhoff integration method developed from the Huygens principle for axisymmetric source, is introduced and derived from the Helmholtz equation. The objective of this section is to develop an efficient integration formula for axisymmetric transducers.

1.2.1 Kirchhoff integral modelling for a circular piston

In theory, either Rayleigh integral or Kirchhoff integral is employed to obtain the acoustic field distribution of a transducer. However, the Kirchhoff integral is a simplification approximation of the double Rayleigh integrals. For the radiation elastic body with regular shape, in our cases, circular or annular piston transducer, Kirchhoff integral supplies a simple expression for steady wave field distribution with reasonable calculating time. Further this expression of Kirchhoff integration is easy to implement for numerical calculations. For those reasons, the Kirchhoff integral is then deduced and simplified from the impulse response of a circular radiation object.

The integration method ordinarily assume that the velocity profile across the surface of the transducer is spatially uniform, although other improved models permit some radial variation in the velocity profile. The following acoustic radiation mechanism study and experimental measurement of the acoustic field produced by a capacitive air-coupled transducer verify this precondition of the integration method. The impulse response is primarily used for pulsed mode calculations in the near-field region; however, this model is also suitable for time harmonic pressure calculations in the far field.

Two equivalent single integral expressions are described by Archer-Hall [91] and Hutchins [92] specifically for time-harmonic near-field calculations of the pressure generated by a circular piston with infinite baffle around (*i.e.* clamped condition all around the circular piston). The expression in [91] applies a cylindrical coordinate system with a movable origin to the solution of the Kirchhoff integral. These geometric manipulations convert a double integral into a simplified single integral.

The impulse response for a circular piston in time domain, defined as $h(r, z; t)$, is a function of temporal and spatial parameters in cylindrical coordinate system. It is applicable to time-harmonic acoustic pressure calculations with the Fourier transform. $H(r, z; \omega)$ is the temporal Fourier transform of the impulse response $h(r, z; t)$, which is derived as: $H(r, z; \omega) = \mathcal{F}\{h(r, z; t)\}$. Starting from a harmonic and uniform vibration of the transducer surface, the temporal velocity of the surface is $V(t) = \nu_0 e^{j\omega t}$, where ν_0 is the uniformed normal velocity at the surface of the piston, t is time. The steady-state pressure at a certain point in the propagation medium $p(r, z; \omega)$ can be derived by the equation according to:

$$p\,(r, z; \omega) = -j\omega\rho\widetilde{\nu}H(r, z; \omega) \tag{1.1}$$

where ω is the excitation angular frequency in radians per second, ρ is the density of the medium, j is the complex number unit defined by $j = \sqrt{-1}$, $\widetilde{\nu}$ is the Fourier transform of

$V(t)$. Thus $H(r, z; \omega)$ is directly proportional to the pressure distribution. The integration coordinate for the simplification of $H(r, z; \omega)$ is illustrated in Figure 1.1. A circular acoustic radiation object with radius a is located at cylindrical coordination (r, z), where the circle centre is the coordinate origin. The integration formula reflecting the spatial impulse response from the surface vibrating element follows an arc-shaped integral geometry perpendicular to the line running from the disk (source) centre, o, and the projection of an observation point *M(r,z)* onto the source surface, *i.e.* point N. Central angle corresponding to the integral arc ψ is regarded as the integration variable for taking into account the overall contribution of the surface element.

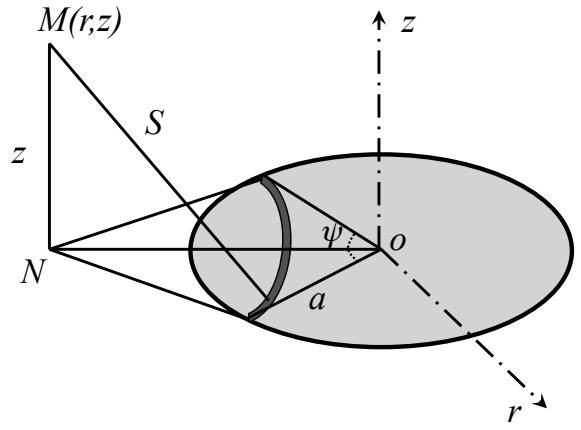

Figure 1.1. Axisymmetric coordinate system for Kirchhoff integration.

An expression on the transfer function of the circular source [91, 93] is given:

$$H(r, z; \omega) = \frac{ac}{j\omega\pi} I + \frac{c}{j\omega} e^{-j\omega z/c} \begin{cases} 1, & r < a \\ \frac{1}{2}, & r = a \\ 0, & r > a \end{cases} \tag{1.2}$$

where I is the integral expression defined by:

$$I(r, z; \omega) = \int_0^{\pi} \frac{rcos\psi - a}{r^2 + a^2 - 2arcos\psi} \times e^{-j\omega\sqrt{r^2+a^2-2arcos\psi+z^2}/c} d\psi \tag{1.3}$$

in which a is the radius of the circular transducer, c is the a complex number related to the sound speed in air, with $c = \omega/k$, k is the complex wave number with $k = k_0 + \alpha j$, where k_0 is the real wave number in air defined by $k_0 = \omega/c_0$, where c_0 is the ultrasound velocity in air, and α is the absorption coefficient of ultrasound in air which will be discussed later on. In Equation 1.2, the term $(c/j\omega)e^{-j\omega z/c}$ is multiplied by $1, 1/2, 0$ according to the location along the radial coordination r relative to the circular edge. This expression takes the contribution of the circular source integration element to obtain the spatial impulse response distribution in cylindrical coordination. However the integral in Equation 1.3 contains a numerical singularity which is encountered when $r \approx a$ and $\psi \approx 0$. This singularity is responsible for increasing the numerical errors in all spatial location

where $r \approx a$. This may result in a discontinuity in the field distribution at the radius boundary $r \approx a$. Although an improved integrand numerical method can be used such as Gauss quadrature, increasing numerical errors are generated in this expression around the location $r \approx a$. The numerical singularity problem can be eliminated by subtracting a singularity from the exponential term in the numerator of integration Equation 1.3 by $e^{-j\omega z/c_0}$. The resulting integration divides an infinitesimal number by another infinitesimal number where $r \approx a$ and $\psi \approx 0$, and reduces the error at the location around $r \approx a$. This improvement gives rise to an efficient formulation [94] of the acoustic field generated by a circular piston transducer as following:

$$H(r,z;\omega) = \frac{ac}{j\omega\pi}\int_0^{\pi} \frac{rcos\psi - a}{r^2 + a^2 - 2arcos\psi} \times (e^{-j\omega\sqrt{r^2+a^2-2arcos\psi+z^2}/c} - e^{-j\omega z/c})d\psi \quad (1.4)$$

The integration expression for the spatial impulse response in Equation 1.4 can be also derived equivalently from Green's function approach that generates a double Bessel functions in cylindrical coordination and then simplifies an integration by using Hankel transform tables [95]. The efficient integration of Equation 1.4 is derived from the Kirchhoff integral method from the Helmholtz acoustic wave equation [73]. Applying numerical integration operation in the integral, the spatial impulse response and further acoustic pressure at any spatial position can be obtained straightforwardly. Therefore, this analytical Kirchhoff integral method will be used in the following calculation of the acoustic field produced by circular air-coupled capacitive transducers.

1.2.2 Ultrasound attenuation in air with Kirchhoff integral modelling

As what has been written in the general Introduction of this work, one of the challenges for air-coupled ultrasonic inspection is the attenuation of ultrasonic wave along its propagation in air. In the Kirchhoff integration modelling, the acoustic propagation medium properties are included in the model by the medium density ρ and sound velocity c_0. The acoustic attenuation effect of wave propagation in medium can be regarded as a complex sound velocity, the imaginary part of which is related to the total effects of acoustic attenuation in medium [72, 96], such as gas viscosity, relaxation absorption and heat conduction, *etc.* [97].

For acoustic plane wave propagating in medium with single frequency, *i.e.* time-harmonic wave, its acoustic pressure is

$$p(\boldsymbol{x},t) = p_0 e^{-\alpha|\boldsymbol{x}|} e^{j(\boldsymbol{k_0}\cdot\boldsymbol{x}-\omega t)} \quad (1.5)$$

where $\boldsymbol{x}$ is the vector from the source to the spatial point, α is the acoustic absorption coefficient in air, $\boldsymbol{k_0}$ is the wave number, defined by $\boldsymbol{k_0} = 2\pi/\lambda \cdot \boldsymbol{n}$, where $\boldsymbol{n}$ is the wave

propagation direction vector, λ is the wave length. In Equation 1.5, by applying a complex wave number in the form of $k = k_0 + \alpha j$, where k_0 is the real wave number in air defined by $k_0 = \omega/c_0$, where c_0 is the ultrasound velocity in air. The complex acoustic velocity $c = \omega/k$ can be substituted into the Kirchhoff integral in Equation 1.4.

For the absorption coefficient in air under the frequency range used in NDT, an empirical power law expression energy losses of ultrasound in air has been found to be [98, 99]:

$$\alpha_{dB} = 1.64 f^2 \times 10^{-10} (dB/m) \tag{1.6}$$

where f is the frequency. From the following comparison between experimental measurement and the model taking into or not the absorption effect of ultrasound in air, this ultrasound attenuation in air under the ultrasonic range is not negligible. Thus, in the analytical model and FE model which will be described further down, this air absorption effect will be included in these models.

1.2.3 Annular superposition method for axisymmetric transducer

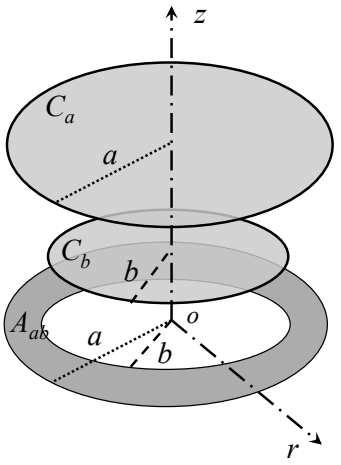

Figure 1.2. Schematic for calculating the acoustic field pressure produced by annular piston through subtracting the contribution between two circular piston.

As the pressure calculation is based on the assumption that every spot at the surface of the piston radiates spherical wave to the medium, the field generated by an annular source can be deduced through the subtraction between the acoustic fields generated by two discs whose diameters are equal to the outer and inner ones. The schematic of this process to obtain the acoustic field produced by an annular piston is shown in Figure 1.2. The acoustic field produced by annular A_{ab} is the subtraction between the fields produced by two circular C_a and C_b, *i.e.*

$$p_{A_{ab}}(r, z; \omega) = p_{C_a}(r, z; \omega) - p_{C_b}(r, z; \omega) \tag{1.7}$$

where $p_C(r, z; \omega)$ is the acoustic field pressure distribution of a circular piston obtained from Equation 1.1 and Equation 1.4. Assembling the acoustic pressure with applying certain delayed phase for each ring of the annular array, we can obtain the acoustic field pressure generated by the annular array in the frequency domain. A more general annular integration method which can be applied to calculate the field produced by the axisymmetric transducers directly is described in Appendix A.

Therefore, with the same principle, the overall pressure field produced by the annular array can be derived through the summation of the acoustic field produced by the separated circular and annular elements. Under applying certain phase delay at each element of the array, the interference effect between the element can give the total acoustic pressure field produced by the array as:

$$P(r, z; \omega) = \sum_{i=1}^{n} p_i(r, z; \omega) e^{-j\Delta\phi_i} \tag{1.8}$$

where $p_i(r, z; \omega)$ represents the respective pressure field produced by the elements of the array, and $\Delta\phi_i$ is the relative phase delay for the element corresponding to that of the reference element. The acoustic wave propagation phase emitted by elements ϕ_i can be derived by:

$$\phi_i = \frac{2\pi f}{c_0} l_i \tag{1.9}$$

in which l_i is the propagation length from the source to the targeted focusing point or beam steering target. Through superposing the pressure generated by each axisymmetric element with certain phase shifting, the total pressure field produced by an annular array can be derived analytically in Kirchhoff model.

1.3 Axisymmetric fluid-solid coupling finite element model

Acoustic theory can provide analytical solutions for the ultrasound field in homogeneous media with simple geometries, but not for sources with complicated structures, or with some defects, which can no longer be regarded as a homogeneous medium. In such situations, it is very difficult or impossible to obtain the analytical solution in the acoustical propagation domain. Under this context, a lot of numerical methods are developed to obtain approximate numerical solutions and are widely used in the ultrasonic NDT domain [64]. In another aspect, the exploration of various commercial softwares offers efficient assistance to scientific researches.

The Finite Element Method (FEM) is an example of very convenient and efficient numerical tool for solving acoustic problems. The Finite Element software used in this work for numerical calculation is COMSOL-Multiphysics [78]. Matlab [89] is used as coding language for developing post processing routines connecting with COMSOL. In

this section, an axisymmetric fluid-solid coupling FE model is developed to predict the acoustic field generated by air-coupled circular and annular transducers. This model takes into account of the practical boundary conditions and propagation medium properties. It is used to validate and evaluate the accuracy and efficiency of the analytical KIM model.

This work of simulation with FEM mainly includes the following three parts: settings of partial differential equations (PDE) and boundary conditions according to COMSOL formalism, construction of the model and mesh, and improvement in the absorbing region used in frequency domain. Since all the variables and expressions in FE model are defined and calculated in frequency domain, the model uses a stationary solver in frequency range for easy analysis of its acoustic field properties in frequency domain.

1.3.1 COMSOL axisymmetric PDE formalism

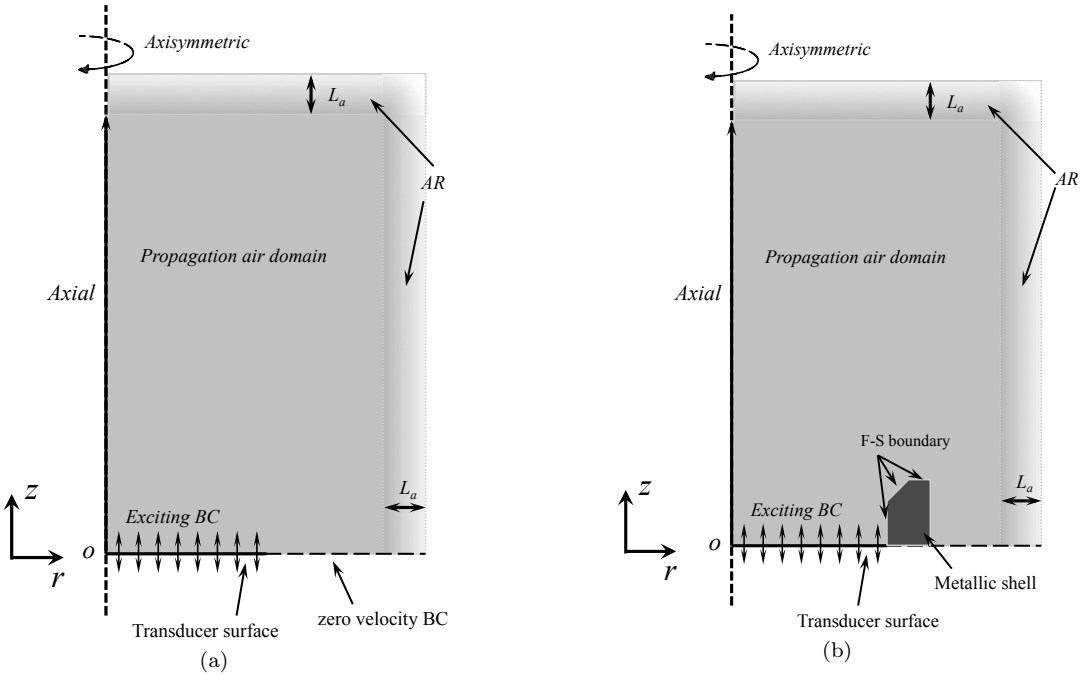

Figure 1.3. Schematic of the axisymmetric fluid-solid coupling finite element model. The excitation source of the transducer is simulated with a exciting boundary condition(BC) setting. Around the propagation air domain(PAD), the absorbing region(AR) is set to absorb the incident wave and avoid the reflection. (a): Circular FE axisymmetric line source model. (b): FE axisymmetric Fluid-Solid coupling model considering effect of metallic shell of transducer.

The schematic figure of the axisymmetric fluid-solid coupling FE model is shown in Figure 1.3. This model bases on the axisymmetric coordinate system with the spatial variables (r, z). The capacitive transducer which is modelled to a line boundary excitation source and metal shell block (as shown in Figure 2.1(b)) has been place at the bottom of the propagation air domain with surrounding absorbing region. Two FE axisymmetric

models are studied in this work either for validation of the KIM model (currently developed) or for comparison with experimental measurement results (in Chapter 2). In Figure 1.3(a), the boundary condition (BC) within the transducer exciting area is simplified as a line source, while at other section of the boundary, zero velocity BC is set nearby to that line source to simulate the same baffled acoustic condition as that considered with KIM model. In Figure 1.3(b), a metallic shell domain is added to the model for simulation of the actual metallic shell behaviour with the real capacitive transducer. At the boundary condition of the metallic shell, the fluid-solid coupling boundary conditions need to be set to simulate the reflection and scattering of the acoustic wave in air. These boundary conditions should be properly written both from the solid domain to fluid domain and from the fluid domain to solid domain in Comsol formalism.

Thus COMSOL is operated with Multiphysics mode by defining two types of domain: one deformable solid domain and one compressible fluid domain with equations in coefficient PDE formalism. The FE model is proceeded in frequency domain, representing a harmonic continuous propagating wave in the fluid and solid domains.

The general coefficient time-independent form of PDE in COMSOL should be identified to its physical mathematical model. This PDE formalism is:

$$\begin{cases} -\nabla \cdot (c\nabla u + \alpha u - \gamma) + \beta \cdot \nabla u + au = f & in \quad \Omega \\ \boldsymbol{n} \cdot (c\nabla u + \alpha u - \gamma) + qu = g & on \quad \partial\Omega \\ hu = m & on \quad \partial\Omega \end{cases} \tag{1.10}$$

where u represents time-independent variables to be determined in the domain Ω and at the boundary $\partial\Omega$. For this model, in the fluid domain it should be acoustic pressure in air, p, and in solid domain it should be displacement variable vector, $\boldsymbol{u} = \{u_r, u_z\}$, representing the displacement components along r and z directions in cylindrical system. f is the bulk source force enforced on the domain. The symbol ∇ is the vector differential operator defined as:

$$\nabla = \left(\frac{\partial}{\partial x_1}, \cdots \frac{\partial}{\partial x_l}, \cdots \frac{\partial}{\partial x_n} \right) \tag{1.11}$$

where n is the number of space dimensions, and $x_1, \ldots, x_n$ are the orthogonal spatial variables. In our model, $n = 2$, and spatial coordinate is (r, z). The first equation in Equation 1.10 defined in the domain Ω is the partial differential equation (PDE) for the acoustic wave propagating in this domain. The second one is Neumann boundary condition defined at boundary $\partial\Omega$, indicating the prescribed flux, such as the acoustic field energy flow through the boundary. The third boundary condition is the Dirichlet boundary condition, also referred to as a fixed boundary condition, implying that a fixed boundary variable value is prescribed at the boundary. In this axisymmetric model, the Dirichlet boundary condition is used to set the fix value to simulate the vibration of the

transducer surface, while the Neumann boundary condition is used to set the proper fluid-solid coupling boundary conditions to satisfy the physical continuity at boundaries. The dimensions of the coefficients $c, \alpha, \gamma, \beta, a, g, q, h, m$ are decided by the space dimension and the number of scalar dependent variables the problem solves. For instance, c will be a 2×2 matrix whose components are 2×2 matrices in our model.

For the axisymmetric problem, all the variables $u(r, \theta, z)$ are angular $\theta-$independent in tri-dimensional cylindrical space (r, θ, z). Thus:

$$\begin{cases} \dfrac{\partial u(r,\theta,z)}{\partial \theta} = 0 \\ u_\theta = 0 \\ u_r, u_z \neq 0 \end{cases} \tag{1.12}$$

The PDE and boundary condition formalism are discussed below separately both for air and solid in axisymmetric situation, respectively.

1.3.1.1 PDE formalism in air

In fluid domain, the non-source acoustic wave propagation equation is known as:

$$\nabla^2 p = \frac{1}{c_0^2}\frac{\partial p}{\partial t} \tag{1.13}$$

For a harmonic propagating acoustic wave, its acoustic pressure in fluid is $p = p_0 e^{j(\omega t - kx)}$. Considering a compressive fluid medium with bulk modulus K_f(in GPa, the adiabatic bulk modulus of air is $1.44 \times 10^{-4} GPa$), the acoustic wave equation of the fluid can be presented by:

$$-K_f \nabla^2 p - \rho_f \omega^2 p = 0 \tag{1.14}$$

where K_f is the bulk modulus, the inverse of which gives a material's compressibility. In fluid, the relation between bulk modulus and density gives the sound velocity by:

$$c_0 = \sqrt{\frac{K_f}{\rho_f}} \tag{1.15}$$

In θ-independent cylindrical coordinate, the acoustic wave equation is:

$$-K_f \left(r\frac{\partial^2 p}{\partial r^2} + \frac{\partial p}{\partial r} + r\frac{\partial^2 p}{\partial z^2} \right) - \rho_f \omega^2 r p = f \tag{1.16}$$

Comparing Equation 1.16 with Equation 1.10, we can decide the coefficient of PDE in fluid in axisymmetric coordinate.

$$c = K_f r; \qquad a = -\rho_f \omega^2 r; \tag{1.17}$$

and other coefficients α, γ, β, f is set to be zero in the fluid domain of the model.

1.3.1.2 PDE formalism in solid

Without loss of generality, for a homogeneous anisotropic solid, the equilibrium equations for 2D axisymmetric coordination will be deduced from its 3D cylindrical form [100] through applying the axial symmetry conditions given by Equation 1.12. The equilibrium equation Equation 1.10 for orthotropic material under cylindrical space (r, θ, z) in domain Ω is given by:

$$\begin{cases} -C_{11}\dfrac{\partial^2 u_r}{\partial r^2} - \dfrac{C_{11}}{r}\dfrac{\partial u_r}{\partial r} + \dfrac{C_{33}}{r^2}u_r - \dfrac{C_{55}}{r^2}\dfrac{\partial^2 u_r}{\partial \theta^2} - C_{66}\dfrac{\partial^2 u_r}{\partial z^2} - \dfrac{C_{13}+C_{55}}{r}\dfrac{\partial^2 u_\theta}{\partial r \partial \theta} \\ \quad + \dfrac{C_{33}+C_{55}}{r^2}\dfrac{\partial u_\theta}{\partial \theta} - (C_{12}+C_{66})\dfrac{\partial^2 u_z}{\partial r \partial z} - \dfrac{C_{12}+C_{66}}{r}\dfrac{\partial u_z}{\partial z} - \rho\omega^2 u_r = f_r \\ -C_{22}\dfrac{\partial^2 u_z}{\partial z^2} - (C_{21}+C_{66})\,r\dfrac{\partial^2 u_r}{\partial r \partial z} - \dfrac{C_{23}+C_{66}}{r}\dfrac{\partial u_r}{\partial z} - \dfrac{C_{23}+C_{44}}{r}\dfrac{\partial^2 u_\theta}{\partial \theta \partial z} \\ \quad - C_{66}\dfrac{\partial^2 u_z}{\partial r^2} - \dfrac{C_{66}}{r}\dfrac{\partial u_z}{\partial r} - \dfrac{C_{44}}{r^2}\dfrac{\partial^2 u_z}{\partial \theta^2} - \rho\omega^2 u_z = f_z \\ -\dfrac{C_{33}}{r^2}\dfrac{\partial^2 u_\theta}{\partial \theta^2} - \dfrac{C_{31}+C_{55}}{r}\dfrac{\partial^2 u_r}{\partial r \partial \theta} - \dfrac{C_{32}+C_{44}}{r}\dfrac{\partial^2 u_z}{\partial \theta \partial z} - \dfrac{C_{33}+C_{55}}{r^2}\dfrac{\partial u_r}{\partial \theta} - C_{44}\dfrac{\partial^2 u_\theta}{\partial z^2} \\ \quad - C_{55}\dfrac{\partial^2 u_\theta}{\partial r^2} - \dfrac{C_{55}}{r}\dfrac{\partial u_\theta}{\partial r} + \dfrac{C_{55}}{r^2}u_\theta - \rho\omega^2 u_\theta = f_\theta \end{cases} \tag{1.18}$$

where C_{ij} is the solid stiffness tensor. The orthogonal subscript ij are indicated as following: $1 \to r, 2 \to z, 3 \to \theta$. Noting that for isotropic materials there are only two independent stiffness components, in this case C_{11} and C_{66} are regarded as the independent components, the relations between the components are as following: $C_{11} = C_{22} = C_{33}$, $C_{44} = C_{55} = C_{66}$, $C_{12} = C_{13} = C_{23}$, and $C_{12} = C_{11} - 2C_{66}$. Applying the θ independent conditions (Equation 1.12) and the isotropic material conditions into Equation 1.18, we can get the coefficient value in PDE formalism of solid as following:

$$c = \begin{Bmatrix} c_{11} & c_{12} \\ c_{21} & c_{22} \end{Bmatrix} = \left\{ \begin{Bmatrix} C_{11}r^3 & 0 \\ 0 & C_{66}r^3 \\ 0 & C_{12}r^2 \\ C_{66}r^2 & 0 \end{Bmatrix} \begin{Bmatrix} 0 & C_{66}r^2 \\ C_{12}r^2 & 0 \\ C_{66}r & 0 \\ 0 & C_{22}r \end{Bmatrix} \right\} \tag{1.19}$$

$$a = \begin{Bmatrix} a_{11} \\ a_{12} \end{Bmatrix} = \left\{ \begin{Bmatrix} (C_{11}+2C_{13}+C_{33})r - \rho\omega^2 r^3 \\ 0 \end{Bmatrix} \begin{Bmatrix} 0 \\ -\rho\omega^2 r \end{Bmatrix} \right\} \tag{1.20}$$

$$\beta = \begin{Bmatrix} \beta_{11} \\ \beta_{21} \end{Bmatrix} = \left\{ \begin{Bmatrix} (C_{11}+C_{33})r^2 & 0 \\ 0 & 0 \end{Bmatrix} \begin{Bmatrix} 0 & 0 \\ (C_{12}+C_{23})r & 0 \end{Bmatrix} \right\} \tag{1.21}$$

$$\alpha = \left\{ \begin{array}{c} \alpha_{11} \\ \alpha_{21} \end{array} \right\} = \left\{ \begin{array}{c} \left\{ \begin{array}{cc} (C_{11}+C_{13})r^2 & 0 \\ 0 & (C_{11}+C_{23})r \end{array} \right\} \\ \left\{ \begin{array}{cc} 0 & 0 \\ 0 & 0 \end{array} \right\} \end{array} \right\} \tag{1.22}$$

$$f = \left\{ \begin{array}{c} f_1 \\ f_2 \end{array} \right\} \tag{1.23}$$

1.3.2 Boundary conditions in fluid-solid coupling model

With respect to the boundary settings, as the model schematic in Figure 1.3(a) and (b), such boundaries should be considered:

- The boundary at the bottom of propagating air domain (PAD) which simulates the vibration of transducer surface. As in Figure 1.3(a), the excitation of the transducer surface is simulated by prescribing a non-zero velocity along a section of the bottom boundary while the velocity is fixed to zero at the remaining section.
- The axial symmetry boundary that determines the symmetry of the PAD. Since the entire domain is axial symmetry at this boundary, the radial particle displacement is zero at this boundary. In other word, the acoustic energy flux along radial direction along this symmetric axis keeps zero. Thus Neumann boundary condition (*i.e.* the second equation in Equation 1.10) is applied at the symmetry boundary to prescribe the zero-flux or zero radial displacement at this boundary.
- The boundaries surrounding the PAD at the edge of absorbing region (AR) which is used to eliminate the incident wave and avoid reflections. These boundaries setting will be illustrated further in section when setting of absorbing region.
- The boundaries for the metallic shell in Figure 1.3(b). These boundaries involve the fluid-solid coupling relation to keep physical variables continuous, which is fully discussed below.

1.3.2.1 Boundary conditions from fluid

At the fluid-solid interface the particle normal displacement and normal stress must be kept continuous as physical laws. In fluid domain, the acoustic pressure is related to the particle displacement through equilibrium equation known as the Euler's equation [72]:

$$\nabla p = -\rho_f \frac{\partial \boldsymbol{v}}{\partial t} = -\rho_f \frac{\partial^2 \boldsymbol{u}}{\partial t^2} \tag{1.24}$$

For a harmonic plane wave, $\boldsymbol{v} = j\omega\boldsymbol{u}$, since the acoustic wave will be presented as $\boldsymbol{u} = u_0 e^{j(\omega t - \boldsymbol{k}\cdot\boldsymbol{x})}$. Therefore:

$$K_f \nabla p = \rho_f \omega^2 K_f \boldsymbol{u} \tag{1.25}$$

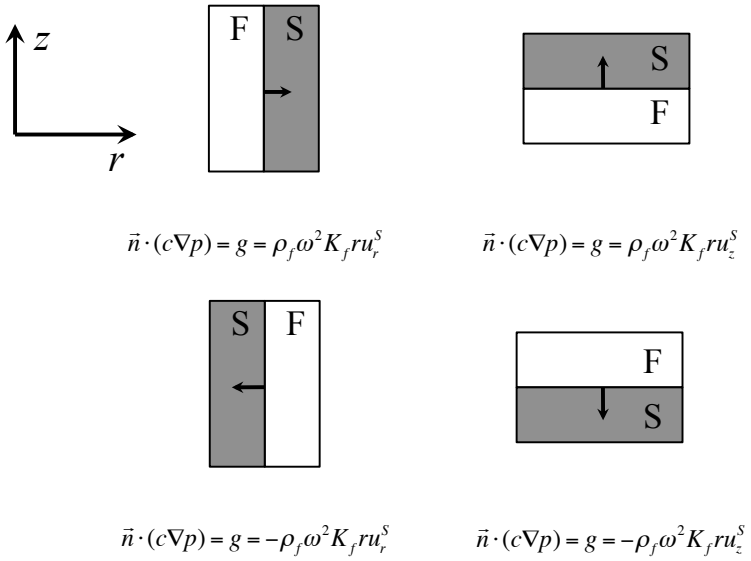

Figure 1.4. Axisymmetric fluid-solid boundary conditions from fluid domain.

The displacement at the fluid-solid interface $\boldsymbol{u}$ is equal to $\boldsymbol{u}^s$, which is the displacement of solid at the interface. The normal displacement at the interface is continuous. So the relation from the fluid is:

$$\boldsymbol{n} \cdot (K_f \nabla p) = \rho_f \omega^2 K_f \boldsymbol{n} \cdot \boldsymbol{u}^s \tag{1.26}$$

where $\boldsymbol{n}$ is the unit vector pointing from the fluid to the solid. This boundary condition can be imposed by Neumann condition in Equation 1.10. Since in fluid domain c is defined as $K_f r$, the relation should be:

$$\boldsymbol{n} \cdot (c \nabla p) = g = \rho_f \omega^2 K_f r \boldsymbol{n} \cdot \boldsymbol{u}^s \tag{1.27}$$

In axisymmetric problem with θ-independent, it can be written in the component form as:

$$g = n_r c r \frac{\partial p}{\partial r} + n_z c \frac{\partial p}{\partial z} = \rho_f \omega^2 K_f r (n_r u_r^s + n_z u_z^s) \tag{1.28}$$

where $\boldsymbol{n} = \boldsymbol{n_r} + \boldsymbol{n_z}$, so $\boldsymbol{n_r}$ and $\boldsymbol{n_z}$ are the directivity cosine in r and z directions. Examples of the axisymmetric fluid-solid boundary condition settings from fluid domain are shown in Figure 1.4.

1.3.2.2 Boundary conditions from solid

Boundary condition settings from the solid domain at the interface can be considered as the stress continuity. The normal stress in the solid must be continuous to the

pressure in the fluid, which is directly derived from the third Newton law. So the normal components of these variables at the interface can be written as:

$$\overline{\overline{\sigma}}\boldsymbol{n} = -p\boldsymbol{n} \tag{1.29}$$

where $\overline{\overline{\sigma}}$ is the stress tensor, and $\boldsymbol{n}$ is a unit vector pointing from the solid to fluid. This equation can be developed in axisymmetric coordinate system as the form of components:

$$\begin{vmatrix} \sigma_{rr} & \sigma_{rz} \\ \sigma_{zr} & \sigma_{zz} \end{vmatrix} \begin{pmatrix} n_r \\ n_z \end{pmatrix} = -pr \begin{pmatrix} n_r \\ n_z \end{pmatrix} \tag{1.30}$$

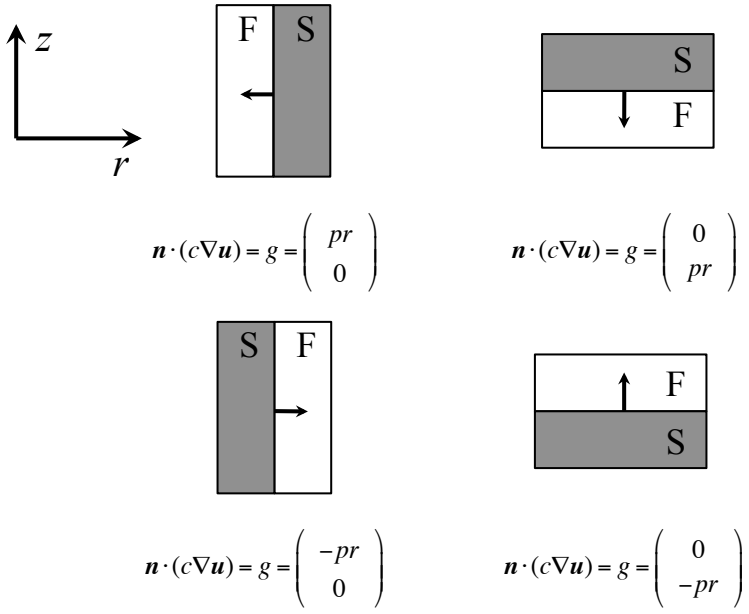

Figure 1.5. Axisymmetric fluid-solid boundary conditions from solid domain.

This equation connects the stress in solid and the pressure in fluid together at the boundary where the fluid-solid coupling relation is applied. Noting that the Neumann condition in Equation 1.10 is $\boldsymbol{n} \cdot (c\nabla u + \alpha u - \gamma) + qu = g$, the coefficient q has to be set to zero, and then the term g has to be set equal to $-p\boldsymbol{n}$, the form of which may be different in axisymmetric coordinate system depending on the orientation of the solid/fluid interface in the (r, z) coordinate axis. Several examples are shown in Figure 1.5.

1.3.3 Absorbing region

This axisymmetric FE model is performed in the frequency domain which uses stationary solver, while the echoes from the boundaries can not be eliminated by setting a window as in time domain. Therefore, absorbing regions are needed to eliminate all the reflection from the edges of the surrounding air domain to simulate an unbounded medium space in the model. Essentially, there are typically two kinds of absorbing region used in frequency domain, one is called Viscoelastic Absorbing Region (VAR) [10, 11, 101] and the

other is the Perfectly Matched Layer (PML) [11, 102–104]. As what their names imply, the VAR setting approach applies gradually increasing viscoelastic properties in absorbing medium to gradually decrease the incident acoustic wave amplitude in the region. While the later one requires a layer equal to about one wavelength of the propagating wave to be absorbed, it needs the motion equation to be added a specific damping term. Related to the work about wave propagation in air, the VAR is introduced and an improved VAR [79] setting method is discussed.

1.3.3.1 Viscoelastic Absorbing Region

Basically, the idea of Viscoelastic Absorbing Region (VAR) is to use the increasing of visco-elasticity of materials as the damping in the absorbing region. The visco-elasticity of materials is usually described by complex stiffness moduli, where the real and imaginary parts are related to the elastic and attenuation properties, respectively. The imaginary parts, which will subsequently appear in the attenuation term of displacement solutions, seem to be directly linked to attenuations in the amplitudes of waves, so VAR is set by continuously increasing the imaginary parts of the complex moduli, in order to acceleratingly absorb the waves without causing reflections from the edge of finite calculation spatial limits. The imaginary parts of moduli are set as the functions of the position within the VAR to gradually absorb the incident wave and avoid unacceptable reflection. This can be controlled by the attenuation function employed along the position direction in the AR.

In our cases, the elimination of reflections from the border of air domain can be implemented by setting an absorbing layer with the length L_a as shown in Figure 1.3. For the PAD is limited within $0 \leq r \leq r_{max}$, $z_{lower} \leq z \leq z_{upper}$, where r_{max} is the spatial limit in radial direction, z_{lower} is the lower spatial limit of PAD and z_{upper} is the upper spatial limit. the absorption is located in the area $r < r_{max} - L_a$, $z < z_{lower} + L_a$ and $z > z_{upper} - L_a$, in which L_a is the thickness of the AR.

The air bulk module K_f(in GPa) is defines as a complex module of which the real part is related to its compressibility and the imaginary part is related to the acoustic absorption coefficient in air α in Equation 1.6. The complex bulk modulus in PAD is a constant complex coefficient $K_f = \Re\{K_f\} + j\Im\{K_f\}$, where $\Re\{K_f\}$ is the real part of K_f, and $\Im\{K_f\}$ is its imaginary part. So the bulk module of air in VAR is set to:

$$K_f^{AR} = K_f + j\Re\{K_f\}A\left(\frac{d}{L_a}\right)^3 \tag{1.31}$$

in which the imaginary part of K_f^{AR} increases with power function along the position variable d (r or z in this model): from the interface between VAR and PAD to the edge position of VAR. A is a constant for the optimization use to adjust the attenuation rate of compressibility in air. By the increase of imaginary part along the absorbing region, the amplitude of incident acoustic pressure decreases as close to the borders of the domain.

This VAR setting method is useful because its mathematical formula can easily be implemented in almost any software/code. However, to attain the aim of minimizing the amplitudes of reflections to at highest 0.1% of that of the incident waves, the length of VAR can be reduced to 3 times of the ultrasound maximum wavelength in air [49].

1.3.3.2 Improved Viscoelastic Absorbing Region

Obviously, this VAR approach is to purely utilize the increasing visco-elasticity in AR to decrease the amplitude of the incident wave and avoid the reflection. Recently, an improved VAR setting formula has been proposed for varying the material properties both for the visco-elasticity and for the mass density to accelerate this absorption without unacceptable reflection. This improved VAR setting method works also relying on the increasing imaginary moduli to absorb the incident acoustic wave. While the real part of the moduli, *i.e.* bulk module of air, in our case, is gradually decreased so that the sound wavelengths in air decrease in AR. Further, this method refers the conception of PML to keep the acoustic impedance to be close between the PAD and VAR to decrease the reflection under a faster damping within the layer. Thus it greatly reduces the width of AR.

The parameters of the respective coefficient of this improved VAR are demonstrated as following:

$$K_f^{AR} = K_f \left(1 - \left(\frac{d}{L_a}\right)^3 + jA\left(\frac{d}{L_a}\right)^3\right), \quad \rho^{AR} = \rho_0 / \left(1 - \left(\frac{d}{L_a}\right)^3 + jA\left(\frac{d}{L_a}\right)^3\right) \tag{1.32}$$

where the position variable d (r or z) is defined the same with that of classic VAR in Equation 1.31. Noting that the acoustic impedance of AR is $Z^{AR} = \rho^{AR} c_0^{AR} = \sqrt{\rho^{AR} K_f^{AR}} = \sqrt{\rho_0 K_f}$, we can see the acoustic impedance keeps constant between the PAD and VAR in the fluid. This implies that the perfectly matching acoustic impedance at the interface between PAD and VAR, which will cause a full refraction and no reflection. This efficient method to set VAR greatly increase the efficiency of absorption within small width of AR. It has been demonstrated that the improved VAR will reduce the AR to 1.5 times of the wavelength to confirm the reflection from the AR less than 0.1% of the incident wave. Therefore, the following AR setting for air-coupled problem will adopt this improved VAR to deal with the unbounded acoustic propagation problems.

1.4 Validation of KIM with axisymmetric FE model

One of the purposes to develop the axisymmetric FE model is to validate the Kirchhoff model for the prediction of the acoustic field produced by circular or annular transducers. The FEM model has many advantages such as the capability to simulate the various

boundary conditions and PDE with multi physical coupling situations. These advantages are very useful to solve the acoustic problems especially for the acoustic radiation and propagation problems under various acoustic and mechanic conditions.

However, the wavelength of the ultrasound in air is very small (about 10 or more times smaller than that in solid) since the relatively slow sound velocity. Thus the FE model demands large number of meshing elements for proper discretization of the domain to be built. For wave propagation problems, the meshing should satisfy at least 4 or 5 elements for one wavelength if 2^{nd} order (quadradic) elements are used. This leads to very large number of degree-of-freedom (DoF) in the FE models which are used to solve acoustic propagation problems in air. Especially for NDT applications with large distances between the transducers and the tested specimen, FE models might become so heavy that the use of PC requires axisymmetric simplification to be applied. In most cases, even in axisymmetry conditions, the FE model can be quite time-consuming when the air domain to be modelled becomes large, *e.g.* large distance between the transducers or between these and the specimen to be tested.

Therefore, analytical methods are required for the acoustic radiation and propagation problems in air to be solved. The integration methods as that have been presented in Section 1.2, can predict the acoustic field at any distant without involving calculation of the field in the domain between the objective and the source. These integration methods then become very advantageous for applying large acoustic propagating distance in air. Further, when implementing the integration method, some numerical errors may come from the inaccurate discretization of the transducer surface, rather that from the propagation air domain.

Hence, in the following chapters, the analytical integration methods will be used to simulate and optimize the air-coupled capacitive ultrasonic array so that optimal acoustic field profile is obtained. Besides, the application of MEACUT in the plate inspection will also utilize the Kirchhoff integration method to predict the radiated field produced by the multi-element transducer. This model will further play an important role in the analytical FE hybrid model to fully simulate the acoustic NDT process.

In the following sections, the analytical integration method including the Kirchhoff model for circular transducer and annular superposition model for annular element will be compared with the results from the axisymmetric FE model for validation purposes. Further, the acoustic field produced by a 3-element annular MEACUT including a circular and 2 annular element will be calculated with analytical integration method and FE method to validate the field superposition method and compare the calculating capacity of these two models.

1.4.1 KIM model for circular transducer validation with axisymmetric FE model

Following the development of the air-coupled axisymmetric model shown in Figure 1.3(a), a piston circular transducer with radius $r = 9mm$ at frequency $f = 300kHz$ is simulated with the FE model, as shown in Figure 1.6(a). Meanwhile, the Kirchhoff model for the circular transducer presented in Equation 1.1 and Equation 1.4, is developed with Matlab [89] script, the corresponding pressure amplitude results are shown in Figure 1.6(b).

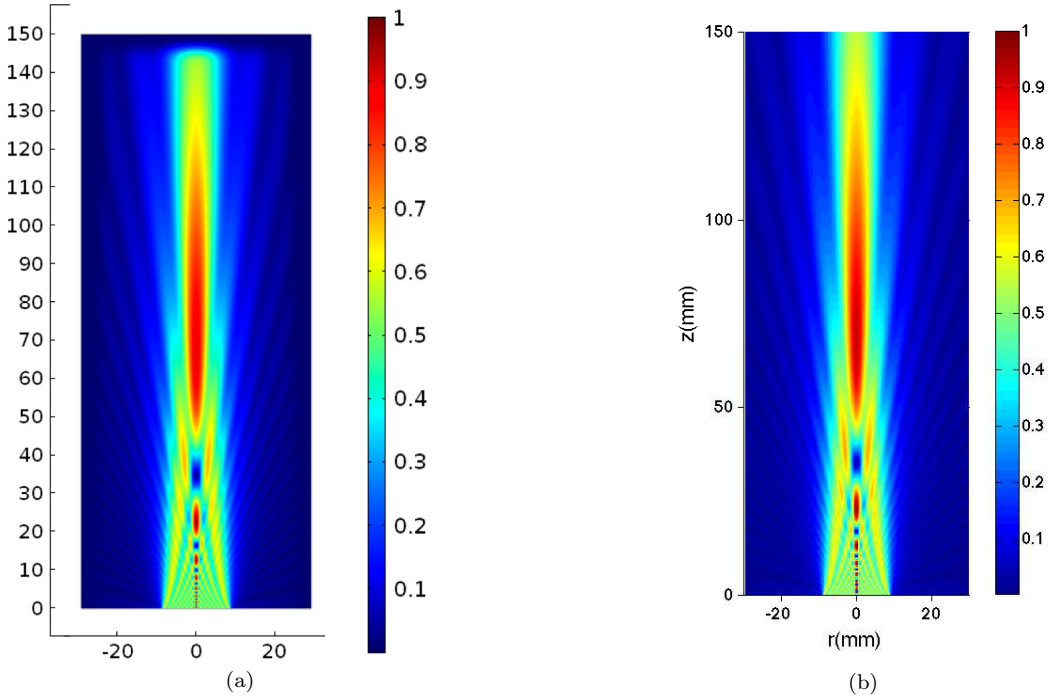

Figure 1.6. Acoustic pressure distribution for a circular air-coupled transducer with radius $r = 9mm$ at frequency $f = 300kHz$. The acoustic pressure amplitudes are normalized for comparison. (a): Normalized acoustic pressure distribution calculated with FEM; (b): Normalized acoustic pressure distribution calculated with KIM.

The axisymmetric FE model shown in Figure 1.6 presents the pressure distribution in (r, z) spatial coordinate. Using the Fresnel principle [72], the far field distance for a circular transducer is $d_f = a^2/\lambda$, where a is its radius, λ is the acoustic wavelength in air. For this transducer, its far field distance is $d_f = 71mm$. Figure 1.6(a) and (b) show that the calculating results obtained from FEM and KIM models agree well and that they both indicate the far field distance stands around $70mm$. Besides, to compare the on-axis pressure distributions obtained from these two models, their data are compared together (including near field and far field) and are shown in Figure 1.7(a). The near field zoom out comparison is shown in Figure 1.7(b), which shows the on-axis distribution from the transducer surface to 70mm.

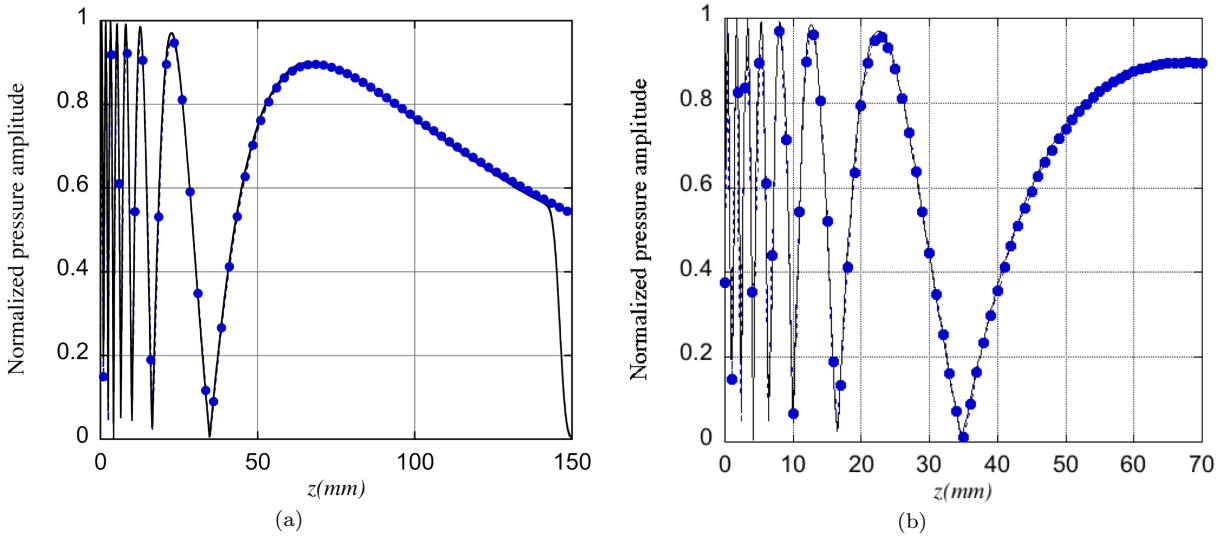

Figure 1.7. Comparison of the on-axis pressure amplitude between axisymmetric FE model (solid line –) and KIM model (dashed circle – • –) for circular transducer with radius $r = 9mm$ at frequency $f = 300kHz$. (a): On-axis pressure distribution comparison. (b): The near field comparison between the two models.

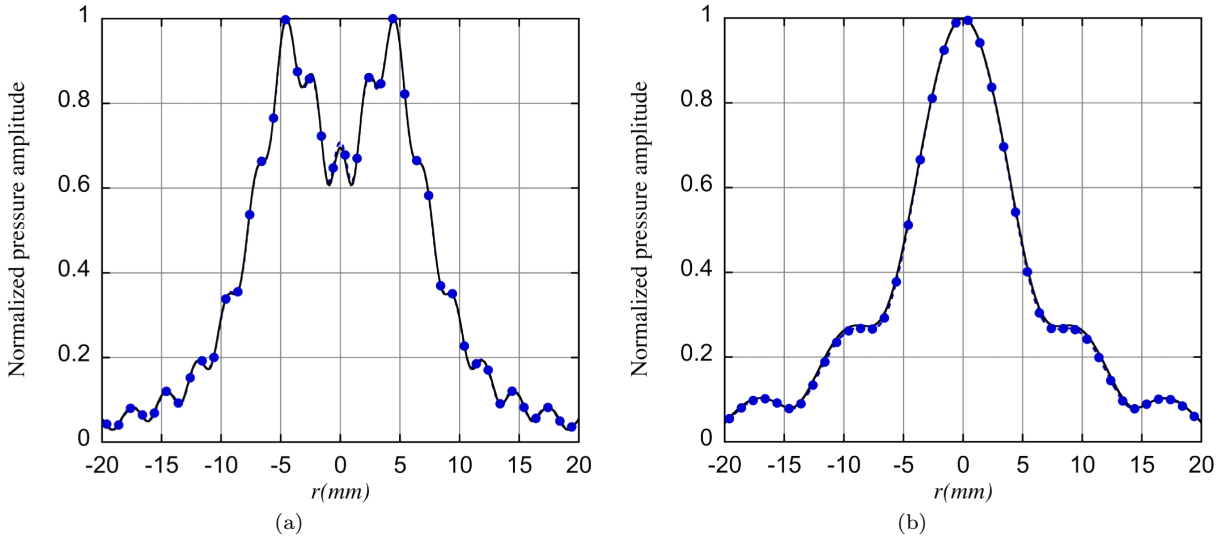

Figure 1.8. Comparison of the transverse pressure amplitude between axisymmetric FE model (solid line –) and KIM model (dashed circle – • –) for circular transducer with radius $r = 9mm$ at frequency $f = 300kHz$. (a): Near field transverse pressure amplitude at distance $z = 30mm$. (b): Far field transverse pressure amplitude at distance $z = 100mm$.

The transverse acoustic field pressure calculated with KIM is therefore validated by the axisymmetric FE model. The comparison between the near field distributions at $z = 30mm$ is presented in Figure 1.8(a), and the far field transverse pressure distribution at distance $z = 100mm$ between these two models shown in Figure 1.8(b). These two sets of distributions agree well between both models. The hypothesis and approximation made by Kirchhoff integral method to form an efficient integral formula are then validated and accepted for modelling air-coupled ultrasonic transducers.

1.4.2 KIM model for annular transducer validation with axisymmetric FE model

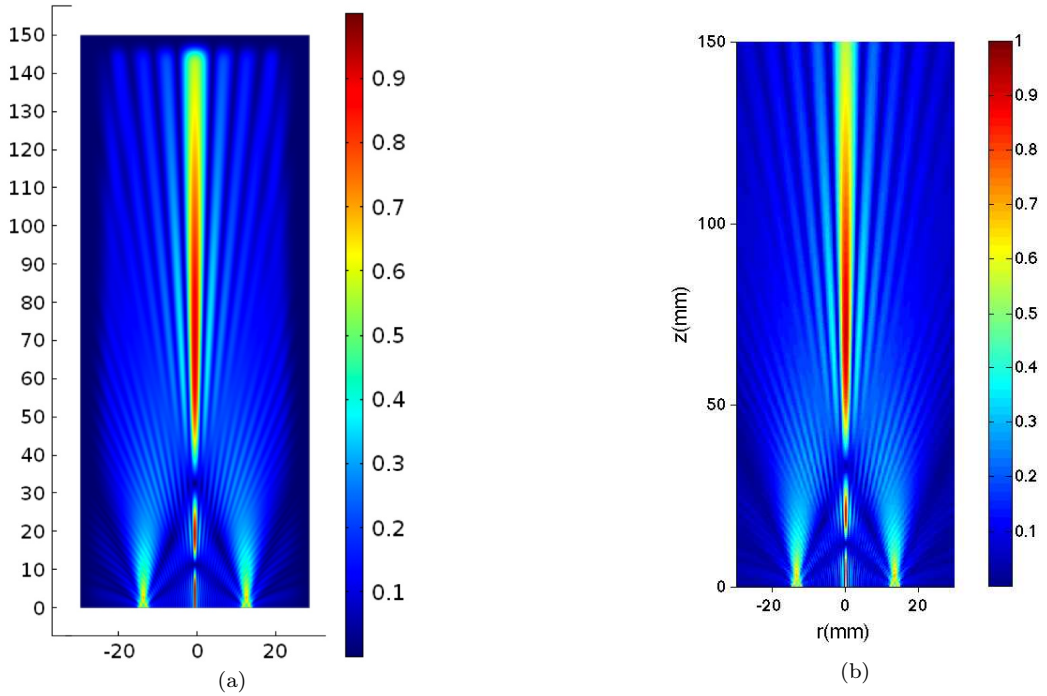

Figure 1.9. Acoustic pressure distribution produced by an annular air-coupled transducer with inner radius $r_{in} = 12mm$ and outer radius $r_{ou} = 15mm$ at frequency $f = 300kHz$: (a): Axisymmetric acoustic pressure calculated with FEM; (b): Axisymmetric acoustic pressure calculated with KIM. The acoustic pressure amplitudes are normalized for comparison between both methods.

The annular superposition model presented in Equation 1.7 is applied to predict the acoustic field produced by a ring shaped (annular) transducer. This superposition method follows the field superposition principle: the acoustic field pressure generated by an annular element is equivalent to the result subtracting the complex acoustic field pressure generated by the inner circular one from the field generated by the outer one. The inner radius of this annular air-coupled transducer is $r_{in} = 12mm$ and its outer radius is $r_{ou} = 15mm$. This model is solved for a single frequency $f = 300kHz$. The acoustic pressure distribution calculated with KIM is shown in Figure 1.9(b). Meanwhile,

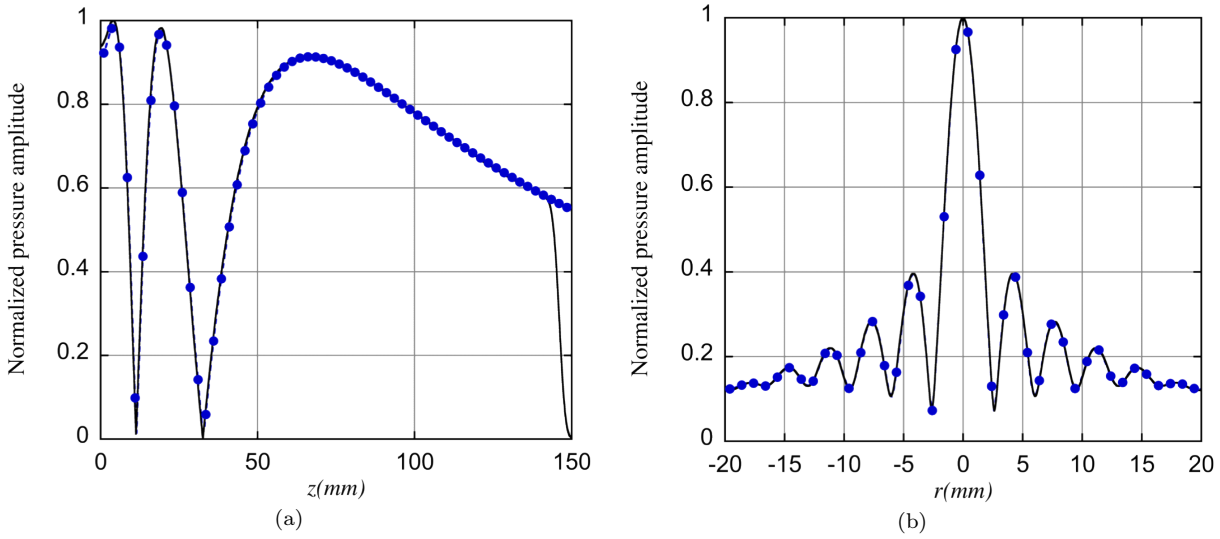

Figure 1.10. Comparison of the on-axis and transverse pressure amplitude between axisymmetric FE model (solid line –) and KIM model (dashed circle – • –) for annular transducer inner radius $r_{in} = 12mm$ and outer radius $r_{ou} = 15mm$ at frequency $f = 300kHz$. (a): On-axis acoustic pressure amplitude distribution. (b): Transverse pressure amplitude at distance $z = 80mm$.

the same physical setting is applied for axisymmetric FE model, by applying an exciting source expression at the boundary as the FE model schematic shown in Figure 1.3(a). The resulting acoustic pressure field from FE model is displayed in Figure 1.9(a). Both 2D acoustic field distributions are normalized numerically for comparison. Visually the 2D pressure distributions of these two model are shown to be in very good agreement.

On axis pressure amplitude distributions obtained by both models are compared in Figure 1.10(a), and the transverse distributions of acoustic pressure amplitude at distance $z = 80mm$ are compared in Figure 1.10(b). Both agreed comparisons indicate that the use of the KIM model with superposition method is validated by the FE axisymmetric model.

1.4.3 Superposition KIM model for a MEACUT validation with axisymmetric FE model

In the previous sections, the KIM model applied for circular and annular elements are validated and compared with FE model. The application of analytical KIM will be used to predict the acoustic field produced by MEACUT, thus a 3-element annular array including a centre circular element and 2 annular elements is modelled to investigate applicability of KIM for modelling MEACUT. With the KIM model, the acoustic field generated by circular or annular elements are calculated separately and are then linearly summed up. For this 3-element annular array, all the elements are excited in phase, *i.e.* without signal delay between elements. The total acoustic field distribution with KIM is shown in Figure 1.11(b). For axisymmetric FE model, the corresponding boundary

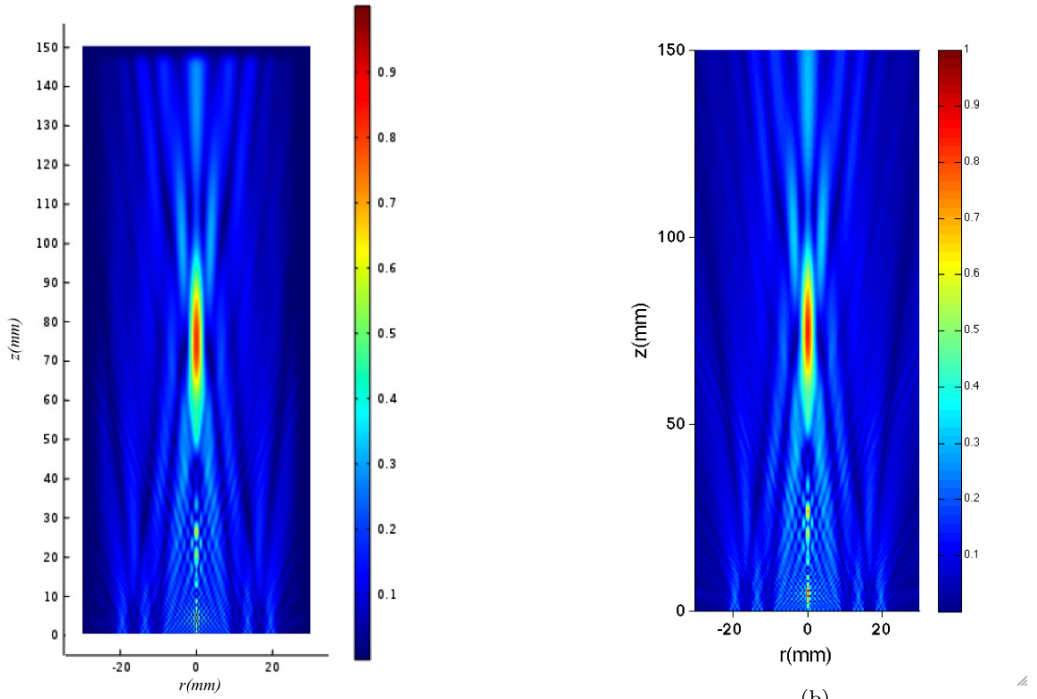

(a) (b)

Figure 1.11. Calculated acoustic pressure distribution produced by 3-element annular air-coupled transducer, the elements include centre circular element N°1: $r = 9mm$; annular elements N°2: with inner radius $r_{in} = 12mm$ and outer radius $r_{ou} = 15mm$ and N°3: $r_{in} = 18mm$ and $r_{ou} = 21mm$. (a): Axisymmetric acoustic pressure calculated with FEM; (b): Axisymmetric acoustic pressure calculated with KIM. The acoustic pressure amplitudes are normalized for comparison between both methods.

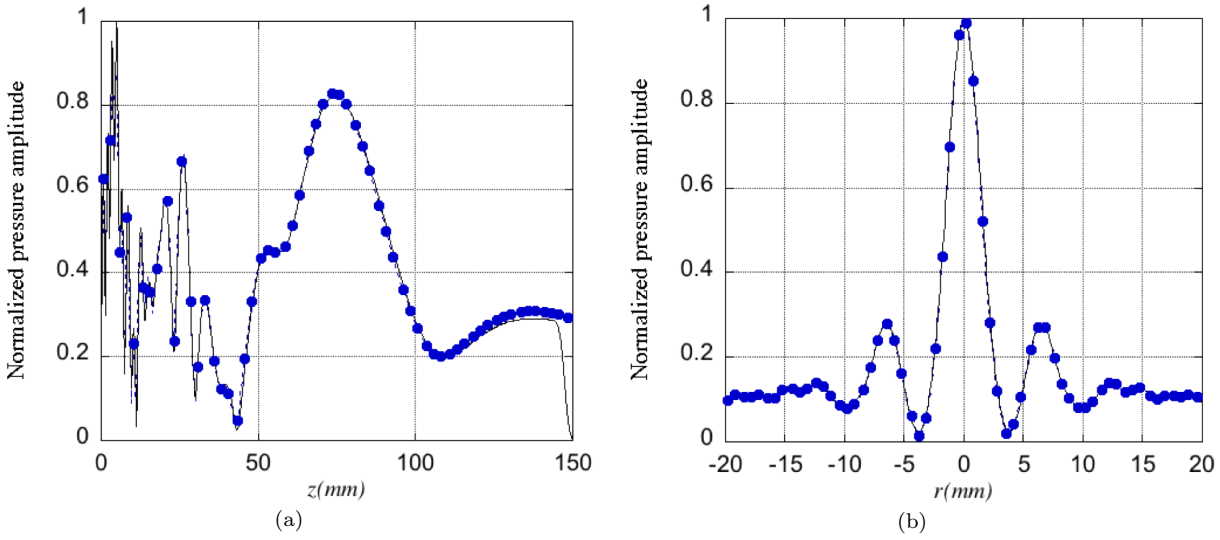

(a) (b)

Figure 1.12. Comparison pressure amplitude distribution between axisymmetric FE model (solid line –) and KIM model (dashed circle –•–) for 3-element annular array, (a): On-axis acoustic pressure amplitude distribution. (b): Transverse pressure amplitude at distance $z = 70mm$.

excitation is set to simulate the annular array. The pressure distribution calculated with FE model is shown in Figure 1.11(a). The acoustic field pattern agrees well between this two methods.

Detailed comparisons between the two models are proceeded on-axis, in Figure 1.12(a), and along transverse at $z = 70mm$, in Figure 1.12(b). The analytical and numerical results agree well for the annular array. Thus it is further validated and demonstrated of the precision and capability of analytical KIM model.

These two models, KIM and axisymmetric FE model, have been tested of calculating time under the same calculation task to compare their efficiency. The Mac used for this testing is driven by CPU: $2 \times 2.26GHz$ Quad-Core Intel Xeon and Memory: $8GB$, $1066MHz$ DDR3. The operation system of the computer is Apple Mac OS X 10.6.8. The Comsol Multiphysics (FEM package) version is 4.2a, and Matlab (programming tool of KIM) version is R2009b 64-bit (maci64). In the test of simulation of circular ACUT in Subsection 1.4.1, the area of the acoustic wave propagation air domain is $150mm \times 30mm$. The axisymmetric FE model uses the 2^{nd} order (quadratic) element and the minimum mesh size of $\lambda/4$. The FE model consists of 153954 triangular elements. The stationary solver of Comsol is MUMPS and the number of DOFs is 309169. The solution time is $14s$. Under the same precision and number of sampling point, the KIM model takes $10.6s$ in the calculation of the axisymmetric acoustic field.

During the test of simulation to 3-element MEACUT in Subsection 1.4.3, the time-consuming of FE model is still $14s$ since the same number of DOF and configurations. While, for the KIM model, it takes $38.9s$ to calculate the whole acoustic field generated by this 3-element MEACUT. This extra time-consuming of KIM is determined by the superposition calculation of acoustic pressure for each element. However, the prediction of the acoustic field of a certain section (*e.g.* transverse pressure distribution at distance $z = 100mm$) runs very fast with KIM model. The prediction of a transverse pressure distribution produced by this 3-element MEACUT takes only $0.9s$ with KIM. Therefore, the advantage of KIM is to predict the acoustic field at a certain section in the field for further optimizations or calculations. In the following chapters, the KIM model will be used to simulate the acoustic field produced by MEACUT for designing and optimization purpose and to consist a 3D hybrid model together with 3D FE model and Rayleigh integration model.

1.5 Summary

There are numerous numerical methods to calculate the acoustic field generated by ultrasonic transducers. Due to the requirement of simplification (in equations and in implementations) and high efficiency, the Kirchhoff integral method has been introduced. An axisymmetric air-solid coupling FE model is developed for the validation purposes of the analytical KIM model.

This Kirchhoff analytical integral model is validated with axisymmetric FE model both for circular transducer, annular transducer, and further a 3-element annular array. The comparisons of the on-axis and transverse pressure fields between these two models show good agreement. Thus the acoustic fields produced in air by axisymmetric transducers have been simulated and successfully validated by axisymmetric FE model. Due to the advantages of analytical method in the air-coupled ultrasonic NDT applications, such as high-efficiency, easy to implement, suitable for large distance propagation problems *etc.* the KIM will be used in the following work to simulate and optimize the air-coupled capacitive multi-element transducer and play its part in the analytical-FE hybrid model for NDT applications.

Chapter 2

Air-coupled capacitive array: simulation, optimization, building and characterization

2.1 Introduction

The objective of this chapter is to model and optimize an ultrasonic, air-coupled transmitter allowing the generation of an ultrasonic beam with variable focusing, within a wide frequency bandwidth and with high efficiency. The proposed solution is a multi-element, capacitive, array, so that the capacitive part should bring up the large frequency range, and the multi-element feature should allow dynamic focusing capabilities under appropriate phase delay control. This annular Multi-Element Air-coupled Capacitive Ultrasonic Transducer (MEACUT) is made of one central circular element and several concentric, annular elements. The designing of this MEACUT is based on the KIM method introduced in Chapter 1. This method will be used for running parametric numerical simulations and for optimising the type of annular array, their elements width and spacing between them, *etc.* Following the optimal parameters, this optimised annular MEACUT will be built and characterized. The characterization consists in measuring its frequency response properties and focused beam profiles.

2.2 Mono-element air-coupled capacitive transducer

The ultrasound emission mechanism of capacitive transducer [24] is based on the principle of an electric capacitor. The physical configuration is that of a capacitor with one back plate as the first electrode, while the other electrode is a metallised membrane which is free to vibrate as the input signal is applied on it. The backplate and membrane are separated by an air gap. In practice, the fabrication of electrostatic transducer is based on an aluminium back plate, which has been sandblasted to form a desired roughness at

its surface, as shown in Figure 2.1(a). A thin Mylar membrane (several micro meters thick) made of Polyethylene Terephtalate (PET), with the external face metallised is deposited on the rough plate. When a DC bias is applied between the back plate and the thin electrode, the membrane gets compressed tightly to the back plate due to the electrostatic force. This turns its state ready to operate. When the capacitive transducer is used as an emitter, an electrical alternative signal is applied in addition to the DC bias to the transducer between both electrodes to generate displacement of the membrane, which will cause an airborne ultrasonic wave. Conversely, as an ultrasonic wave reaches the surface of the transducer, displacement of the membrane caused by the pressure in air will change the capacitive value between the membrane and the back plate. Thus the electric extra charge is generated, which will be transformed into an electric signal through a charge amplifier for further analysis of the received ultrasonic wave.

2.2.1 Configuration and ultrasound emission principle of ACUT

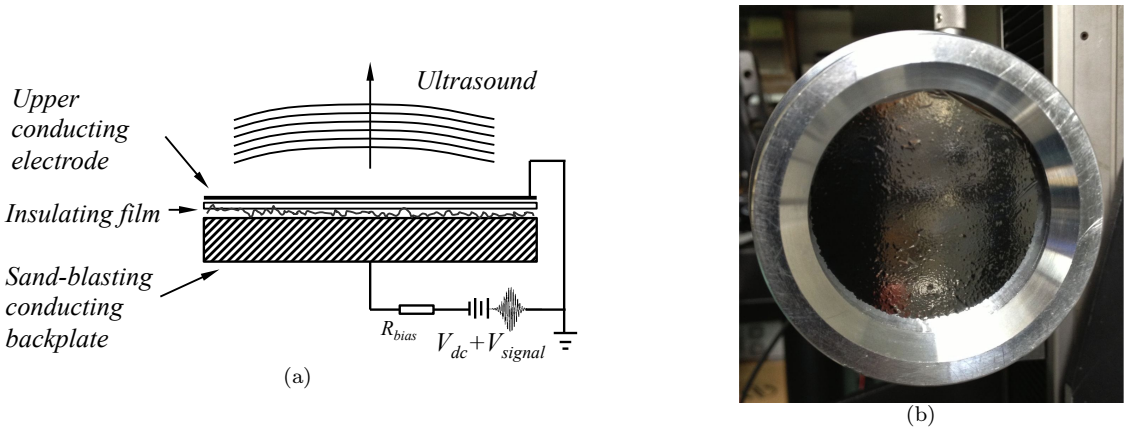

Figure 2.1. Mono element air-coupled capacitive transducer; (a): Principle structure schematic. (b): Capacitive air-coupled transducer photography.

To illustrate the ultrasound emission mechanism of air-coupled capacitive ultrasonic transducer (ACUT), the structure of the capacitive transducer needs to be fully investigated and studied. As shown in Figure 2.1, the electrodes of the capacitor consist of a thin membrane (composing the insulating film and the upper conducting membrane) and a sandblasted backplate [49, 105]. DC bias voltage and signal together is imposed between the electrodes, thus generates pressure p in the air layer depending on square of the applied voltage between the electrodes as the electric static law as following:

$$p \propto (V_{dc} + V_{signal})^2 \tag{2.1}$$

with the bias voltage V_{dc} and the alternating signal voltage V_{signal}. This DC voltage (typical value 100–200 V) is applied between the membrane and the backplate. A resistance R_{bias} is placed in series with the applied voltages to make the operation of the transducer

linear for small signals and to increase the sensitivity. The air layer between the film and backplate could be considered as a Helmholtz resonator with the thickness d_{ag}, as shown in Figure 2.2(a), and acoustic capacitance C_a, acoustic mass M_a, (*i.e.* acoustic inductance L_a), with the equivalent LRC circuit shown in Figure 2.2(b).

For a surface element S of the metal membrane with density ρ_m and thickness d_m, the corresponding volume of the air gap is $V = Sd_{ag}$, the equivalent acoustic capacitance and mass are:

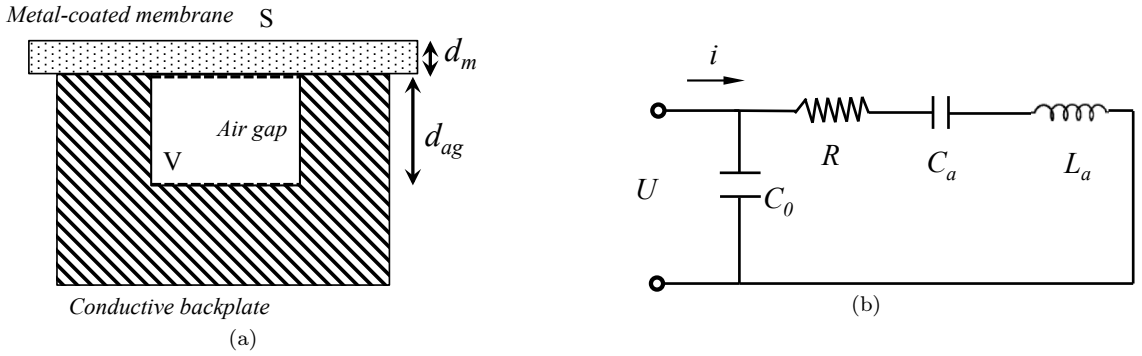

Figure 2.2. (a): Capacitive cavity model diagram of air-coupled transducer. (b): LRC equivalent circuit of the capacitive transducer.

$$C_a = \frac{V}{\rho c_0^2} = \frac{d_{ag}S}{\rho c_0^2}, \quad M_a = \frac{M}{S^2} = \frac{\rho_m d_m}{S} \tag{2.2}$$

where, c_0 is the sound velocity in air, and ρ is the density of air layer, M is the mass of the membrane covering the cavity. To tailor the frequency response of such a capacitive transducer, the resonance frequency [24, 106] of the capacitive transducer is:

$$f_0 = \frac{1}{2\pi}\sqrt{\frac{1}{L_a C_a}} = \frac{1}{2\pi}\sqrt{\frac{1}{M_a C_a}} = \frac{c_0}{2\pi}\sqrt{\frac{\rho}{\rho_m d_m d_{ag}}} \tag{2.3}$$

The model diagram shows that the frequency of the transducer depends on the thickness of the air gap between the back plate and the membrane. The air gap thickness mostly depends on the roughness process and the polarization of the capacitor induced by the bias direct voltage. Generally, highly rough back plate is for low frequency capacitor transducer due to the low resonance frequency related to big volume air gaps. While for high frequency transducer, the smooth back plate with smaller cavities is preferred. These increase the mechanical stiffness of the diaphragm by the edges of cavities. A distribution of the cavity depth can contribute to an enlargement of the frequency bandwidth of transducer according to the relationship between resonance frequency and depth of air gap in Equation 2.3.

Since the sandblasting process of the backplate surface guarantees a vast distribution of the air gap dimension, a wide frequency bandwidth transducer can be built. Comparing with piezoelectric ultrasonic transducers which rely on resonance of the piezoceramic chip,

the response frequency band of the capacitive transducer is extremely wide. In the next section, the characterization method for the air-coupled transducer will be introduced and the its frequency bandwidth will be compared with that of PZT to illustrate this difference.

The intrinsic differences between the technologies of ACUT and piezoelectric transducers lead to the necessity of defining a specific characterization procedure. In the following section, a laser-based vibrometry method is proposed to measure the frequency response and acoustic pressure distribution produced by ACUT.

2.2.2 Characterization of ACUT with laser vibrometry method

To characterize the acoustic field generated by an air-coupled transducer, an experiment setup similar to that used for measuring acoustic field in water [107, 108] is employed. The experimental setup is illustrated in Figure 2.3.

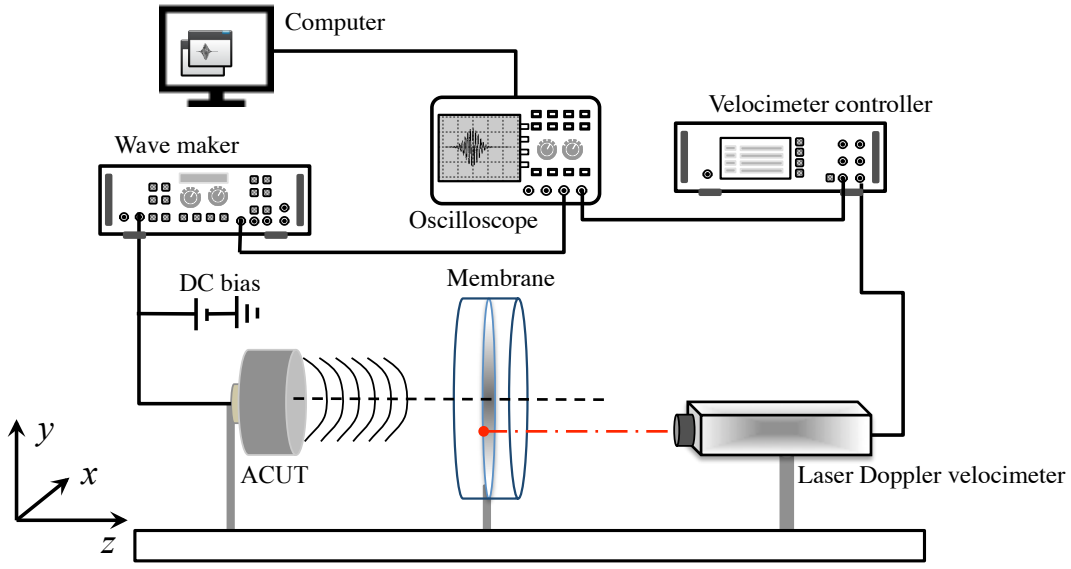

Figure 2.3. Experimental setup to characterize the Air-coupled Capacitive Ultrasonic Transducer (ACUT) with laser Doppler Velocimeter.

A thin metallized polymer membrane is placed into the acoustic field produced by the transducer to be tested to probe the local pressure in air. A laser Doppler velocimeter (LDV) (Polytec OFV-353-3001, sensitivity 5 $mm/s/V$ for a frequency bandwidth of 25 MHz) is used to measure the normal velocity at a given point on the membrane. The membrane has an acoustic impedance equal to $Z_m = 1.82 \times 10^6 Kg \cdot m^{-2} \cdot s^{-1} = 1.82 MRayl$. The impedance of the air is $Z_a = 420 Kg \cdot m^{-2} \cdot s^{-1} = 420 Rayl$. With the plane wave incident, the transmission coefficient [55] ,T_m, of a solid layer in the air is given by:

$$T_m = \frac{4 Z_a Z_m}{(Z_a + Z_m)^2 e^{-jkh} - (Z_a - Z_m)^2 e^{jkh}} \tag{2.4}$$

where h is the thickness of the thin membrane, in our experimental setup $h = 5\mu m$, and k is the wave-number of the ultrasound in the membrane. The velocity and pressure are linked in the fluid by the formula $P_a = Z_a V_a$. The particle velocity in the acoustic field is connected to the velocity of one point on the membrane by $V_m = T_m V_a$, thus the measured membrane velocity V_m gives the acoustic pressure of the given point in air by:

$$P_a = \frac{Z_a}{T_m} V_m \tag{2.5}$$

Thus the local velocity measured by the laser velocimeter is proportional to the acoustic pressure in air. The plane incident wave assumption is satisfied in this setup [55]. The transmission coefficient of the membrane is calculated with respect to the incident wave frequency as shown in Figure 2.4.

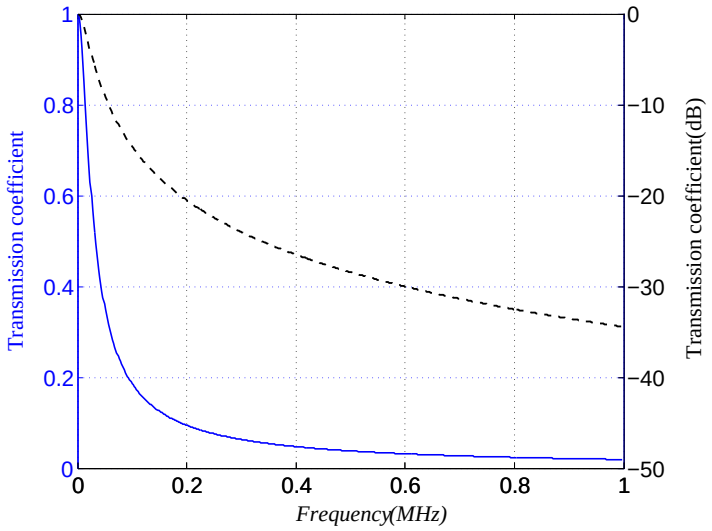

Figure 2.4. Transmission coefficient of the membrane: linear scale (solid line –) and dB scale (dashed line −−)

To compare the frequency response properties between the air-coupled capacitive transducer and PZT transducer. Two types of transducer have been characterized using the experimental set-up in Figure 2.3. To avoid near field acoustic field turbulence, the membrane should be placed at the far field distance from the emitter, which is defined as $d_f = a^2/\lambda$ for circular piston transducer. A short time duration pulse is sent to the emitter to generate an acoustic wave, which will cause the vibration at the membrane. The velocity signal detected by the LDV is a temporal signal including the frequency response information of the membrane and the acoustic field. So the temporal signal should be Fourier transformed to frequency domain, then the modulus for each frequency component need to be divided by the transmission coefficient of the membrane to get the frequency response of acoustic field. The comparison of the frequency response bandwidth of capacitive transducer and PZT is shown in Figure 2.5. For $-20dB$ attenuation criteria in frequency, the capacitive transducer reveals a frequency bandwidth of 120%

corresponding to its centre frequency, comparing with about 17% frequency bandwidth of the piezoelectric transducer.

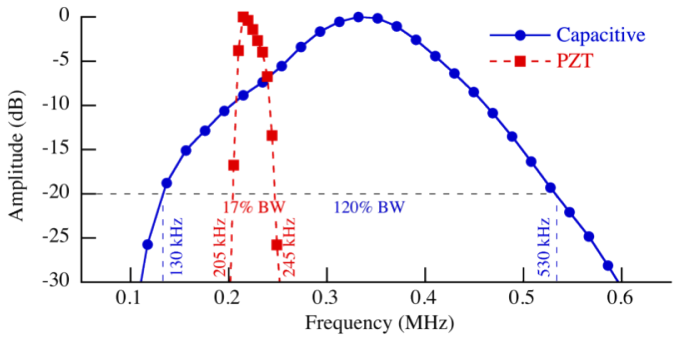

Figure 2.5. Comparison of the frequency response bandwidth of capacitive transducer and PZT.

To characterize the acoustic pressure field distribution produced by ACUT, the laser vibrometry method is used to measure the acoustic pressure profile of a single, circular, $24mm$ in radius, capacitive transducer. It is excited by a Gaussian-windowed, 10-cycle, $100kHz$ centre frequency, sine tone burst. The central frequency is chosen in order to lead to a Fresnel Distance value ($D_f = a^2/\lambda = 168mm$) that allows the scanning of both near field and far field areas with a z-axis translation stage. In the expression, a is the radius of the transducer, and λ is the wave length of ultrasound in air. Besides, the tone burst duration is chosen long enough in order to lead to a quasi-monochromatic regime, but short enough to avoid the temporal superposition of the incident wave and waves reflected between the membrane and the transducer surface.

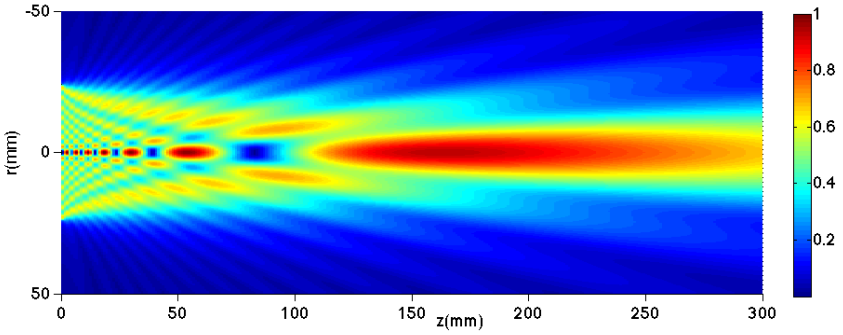

Figure 2.6. Pressure amplitude (Normalized) distribution generated by a circular piston transmitter calculated with axisymmetric Kirchhoff integration method.

Numerical method to simulate the acoustic pressure produced by the transducer is also used to predict the field distribution. As shown in Figure 2.6, the pressure field distribution of this circular mono element transducer has been calculated with KIM in Equation 1.4. The comparison of the on-axis pressure distribution along distance between the simulation and experimental measurement is given in Figure 2.7. It compares the measured, on-axis, pressure distribution together with the corresponding distribution

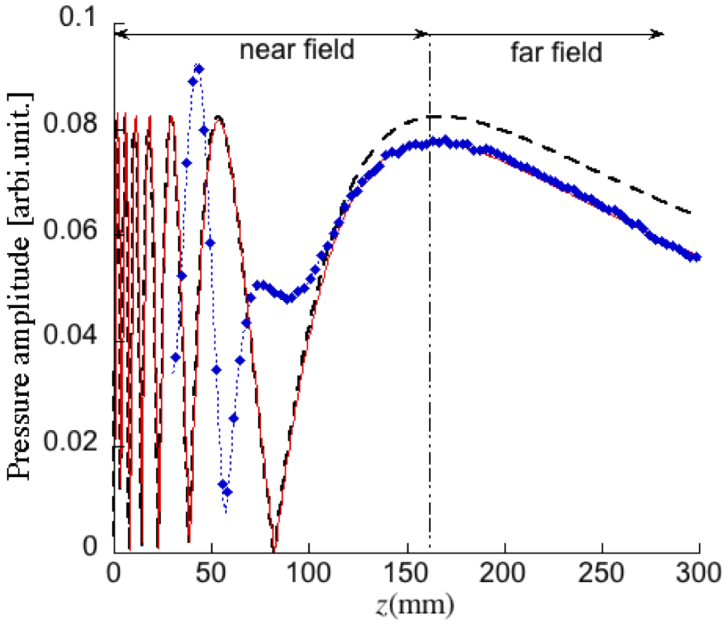

Figure 2.7. On-axis pressure amplitude distribution radiated by a circular transducer versus propagation distance z. Experimental results (dashed diamond $-\blacklozenge-$) and Analytical results with (solid line $-$) and without (dashed line $--$) attenuation effects.

predicted with and without considering attenuation in air by Equation 1.4 and Equation 1.6. The experimental Fresnel distance matches the theoretical one. By considering the amplitude decrease in the far field area, one can see that at this frequency the attenuation effects are not negligible. Thus, in the following analysis, these effects are included in the model. The analytical far field amplitude distribution matches well the experimental results. Conversely, in the near field area, discrepancies remain. The reason may lie on the non-uniform movement of the transducer surface in the experiment. In order to investigate this assumption, the velocity of the surface of the capacitive transducer, *i.e.* its membrane, has been scanned using the Laser Doppler Velocimeter over a square area. The measured velocity profile is presented in Figure 2.8. Due to its fabrication process, the capacitive transducer surface does not vibrate uniformly, and the corresponding pressure amplitude distribution, in the near field area, is found to be quite different than the piston case, which is considered in our analytical model. However, the far field distribution results more from the total contribution of the vibration of the transducer surface,than the near field, thus explaining why the experimental measurements are in good agreement with the predicted far field.

2.3 Air-coupled capacitive annular array: optimization

Phased arrays have been used for long time both as transmitter and receiver of sound waves in various NDT applications. Ultrasonic phased arrays find applications in underwater acoustics, medical imaging, ultrasonic therapy, and non-destructive testing

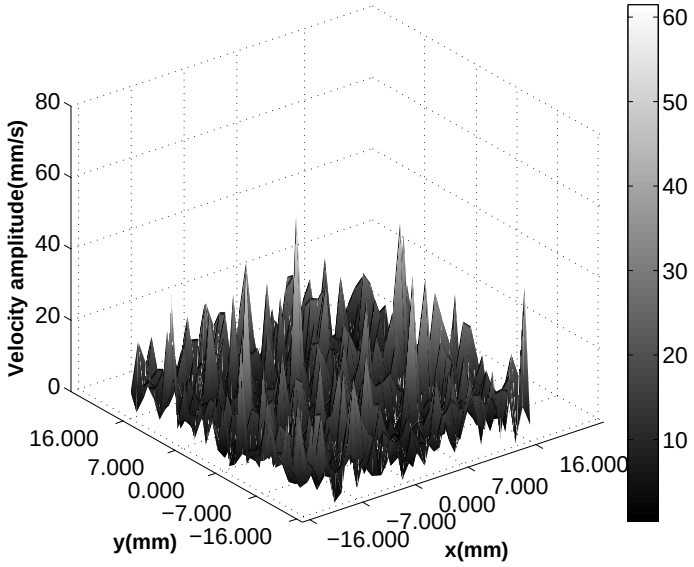

Figure 2.8. 2D scan of the velocity profile (using Laser Doppler Velocimeter) of the capacitive transducer surface: the velocity sensitivity unit is $mm/s/V$

and evaluation. Based on some phased array designing principles and trade-off of its performance, an annular array with limited dimension and number of elements is proposed for air-coupled application in ultrasonic NDT.

The most important parameters affecting the cost and performance of a phased array system are the number of elements and the inter element spacing which is essential to provide a desired angular response (focusing or beam steering for example). In a traditional periodic array, an inter element pitch of less than half wavelength is required to avoid grating lobes [109]. The grating lobes are the result of the periodicity of the element positions. They can be reduced through the use of a random or aperiodic distribution of elements, although at the expense of a reduced dynamic range. The main lobe width is dependent on the spatial extent of the array. The generation of a narrow beam usually requires a wide array.

While in airborne ultrasound application, the frequency range keeps in hundreds of kHz range to avoid great ultrasonic attenuation in air. The wavelength of the ultrasound is shorter than that in solid and in water, *i.e.* about $0.5mm - 3mm$, while those in water and solids are running around $3mm - 70mm$ between $100kHz$ and $500kHz$. For annular array with focusing performance, this requirement of pitch smaller than half wave length is not necessary since the focusing spot is along the annular elements' symmetry axis. Another array designing principle should be considered to optimize the annular array parameters to get optimal focusing beam profile performance.

The acoustic field generated by annular element can be calculated by circular element acoustic field integration Equation 1.4 and annular element integral Equation 1.7. The total pressure produced by the array can be derived by Equation 1.8. The analytical KIM

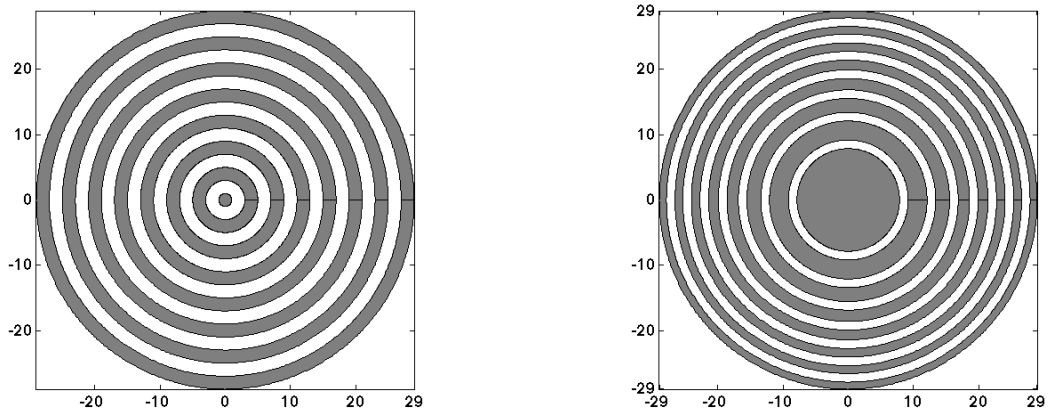

(a) (b)

Figure 2.9. Schematic profile of annular array designing where all the elements (in grey) have the same: (a) width (Type I) and (b) area (Type II).

and field superposition principle are described and validated in Chapter 1. The case of multi-element arrays is considered analytically, in order to test their focusing properties. Two types of array are studied, the schematics of which are shown in Figure 2.9(a) and (b). Both of them consist in an arrangement of 8 elements, but with different geometric sizes. The first one (named Type I) has the following geometrical parameters: a central circular element with diameter equal to $2mm$ is surrounded by 7 annular elements; the spacing between two neighbouring elements is constant and equal to $2mm$, and the width of each element is equal to $2mm$. This leads to a total diameter of the array equal to $58mm$.

The second type of annular array (named Type II) has the same total outer diameter as the first array, but its elements have all the same area. The central element is circular with a radius equal to $7.87mm$, and the 7 surrounding annular elements have different width between each other, so that their areas keep the same. The geometric parameters of these two types of annular array are given in Table 2.1.

Geometric parameters	Type I	Type II
Number of elements	8	8
Centre circular element radius(mm)	1	7.87
Element area(mm^2)	–	194.6
Annular element width(mm)	2	–
Spacing between elements(mm)	2	1.32
Array diameter(mm)	58	58
Total area(mm)	1410.6	1557

Table 2.1. Geometric parameters of annular arrays: type I and type II

For a certain wavelength, the Fresnel distance depends only on the active surface area S of the source for circular transducer: $d_f = a^2/\lambda = S/(\pi\lambda)$. For the annular element,

this Fresnel distance is defined as the far field distance which is equal to that produced by circular transducer with the same area, *i.e.* $d_a = a_c^2/\lambda$, where d_a is the far field distance of annular element, a_c is the radius of a circle with $a_c = \sqrt{r_{ou}^2 - r_{in}^2}$, r_{in} and r_{ou} are the inner radius and outer radius of the annular element respectively.

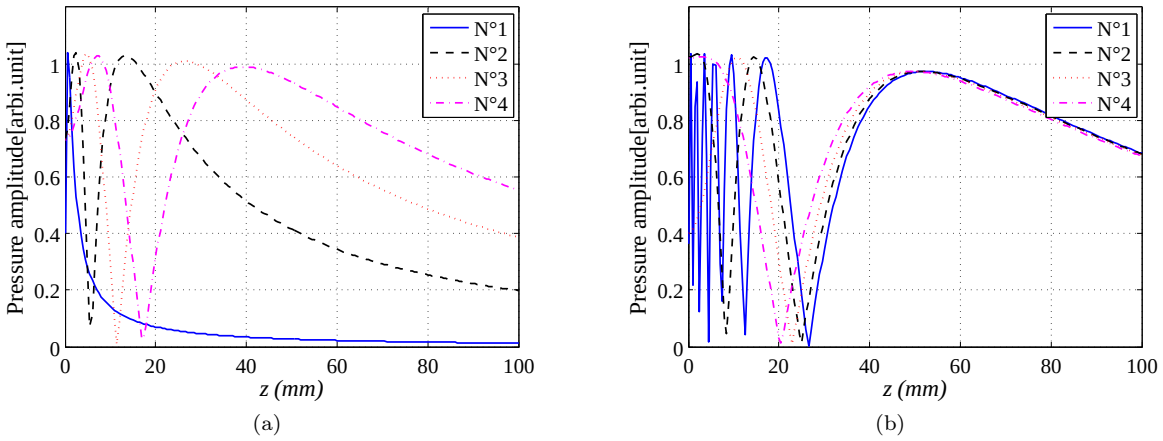

Figure 2.10. Predicted on-axis pressure distributions with annular elements N°1∼N°4: (a)type I; (b)type II. The circular or annular elements in the array are numbered from centre circular element N°1 to edge element N°8.

Thus, for the circular element and annular elements type II which are of the same area, they should have the same far field distance. This feature for axisymmetric transducer known as Fresnel principle is going to be used as the annular array designing principle. If a continuous wave is applied to each element of this same-area-element array, without any phase delay, the total pressure field will present a natural focal feature at their common focusing distance. The on-axis pressure distributions for element N°1∼N°4 of type I and type II are shown in Figure 2.10(a) and (b) respectively. Obviously, elements of type II have the same far field distance, which may be more suitable to perform optimal on-axis focusing beam feature as an annular array.

The exciting signal frequency is equal to $250kHz$, which implies a continuous wave in time domain. The fields radiated by these arrays (either array of type I or II) are derived from the fields radiated by their respective central circular element and surrounding annular elements, and phase shifts in frequency are applied before summing up these various fields together according to Equation 1.8 in order to investigate their dynamic focusing capabilities. Predicted distributions, in the (r, z) plane, of the acoustic pressure amplitude radiated by the first array (Type I) are shown in Figure 2.11. Three focal distances are considered: $z = 100mm$, $z = 150mm$, and $z = 200mm$. The pressure amplitude distributions calculated in the same conditions for the case of a Type II array are plotted in Figure 2.12. As expected, for both types of multi-element arrays, a focal spot appears at the desired location in the air.

The two configurations of annular array designing provide similar pressure amplitude at each focal distance, even if the array of type II provides slightly higher amplitude than

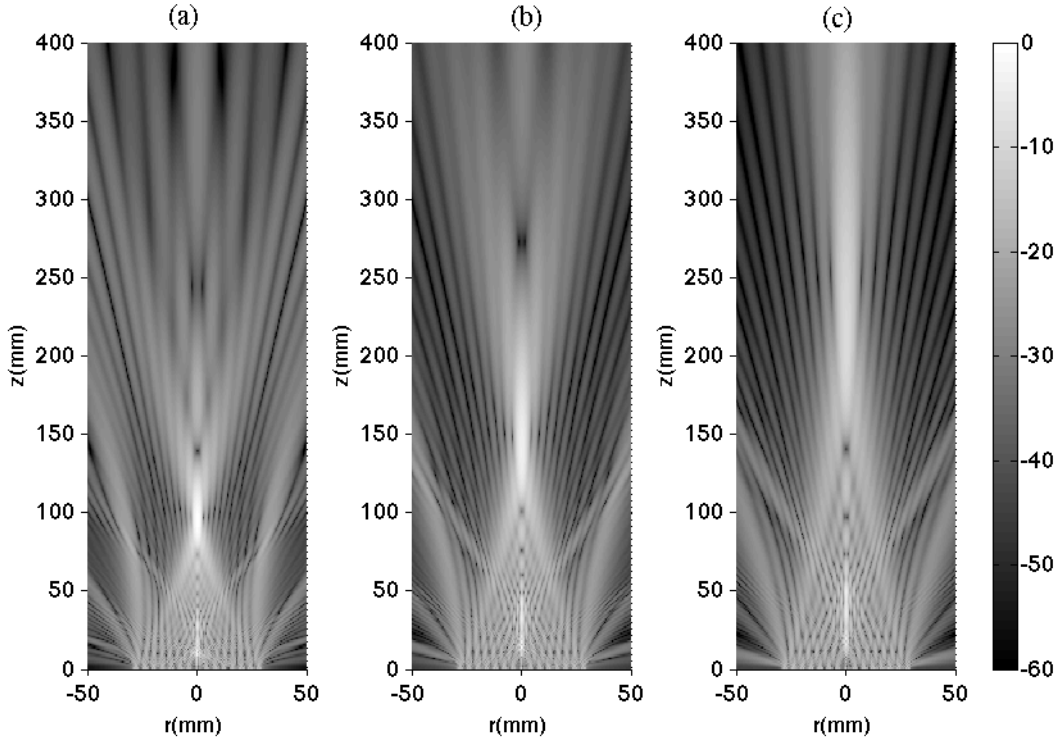

Figure 2.11. Predicted 2D distributions of acoustic pressure amplitude (in dB scale) produced in air by an 8-element annular array of type I, focusing at distances: (a) $z = 100mm$, (b) $z = 150mm$, (c) $z = 200mm$. This type of annular array is made up of elements with constant width and constant spacing.

that produced by the array of type I, at the focusing points, as shown in Figure 2.14(a) and (b). This is mainly because of a larger total acoustic emission area of type II than that of type I as shown in Table 2.1. The amplitude at the focusing point mostly depends on the total area of the active surface of the transducer which contributes to the on-axis pressure interference. Beyond the focusing distance, as the field is focused at a large distance, the pressure amplitude decreases and the lateral dimension of the focal spot increases, deteriorating the transverse spatial resolution for further use of the transducer as a materials scanner.

Acoustic pressure amplitude distributions in transverse direction are plotted in Figure 2.13, at the three previous observing focusing distances: $z = 100mm$, $z = 150mm$ and $z = 200mm$. These plots have been normalized so that amplitudes of all side lobes relative to the maximum amplitude of each plot can be compared together. For the nearest focal distance ($z = 100mm$), grating lobes are visible for the type I array, between $r = 30mm$ and $r = 40mm$, as shown in Figure 2.13(a). The width of these grating lobes is about $10mm$. Although their amplitude is about $22dB$ less than that of the focal spot amplitude of the main lobe, and these grating lobes would be away from the main lobes with the increase of focal length, such grating lobes may induce artefacts if involved in NDT measurements. Conversely, for the array of type II, these grating lobes have significantly reduced amplitudes in Figure 2.13(b). In another aspect, the width of the central main

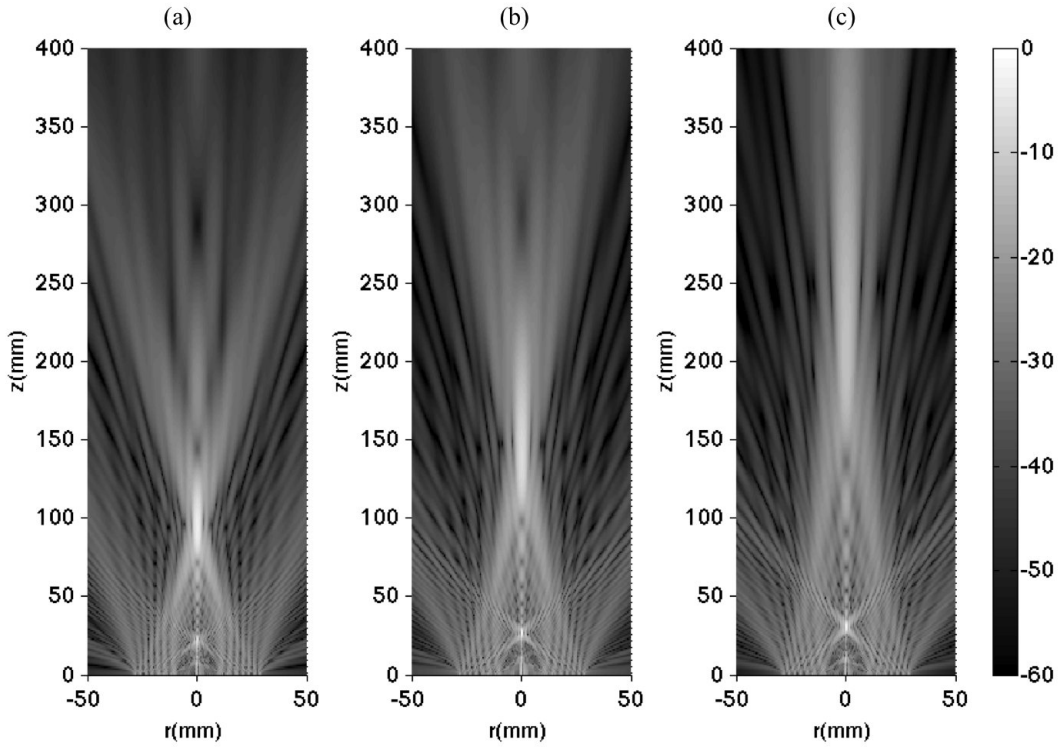

Figure 2.12. Predicted 2D distributions of acoustic pressure amplitude (in dB scale) produced in air by an 8-element annular array of *typeII* focusing at distances: (a) $z = 100mm$, (b) $z = 150mm$, (c) $z = 200mm$. This type of annular array is made of elements with constant area and constant spacing.

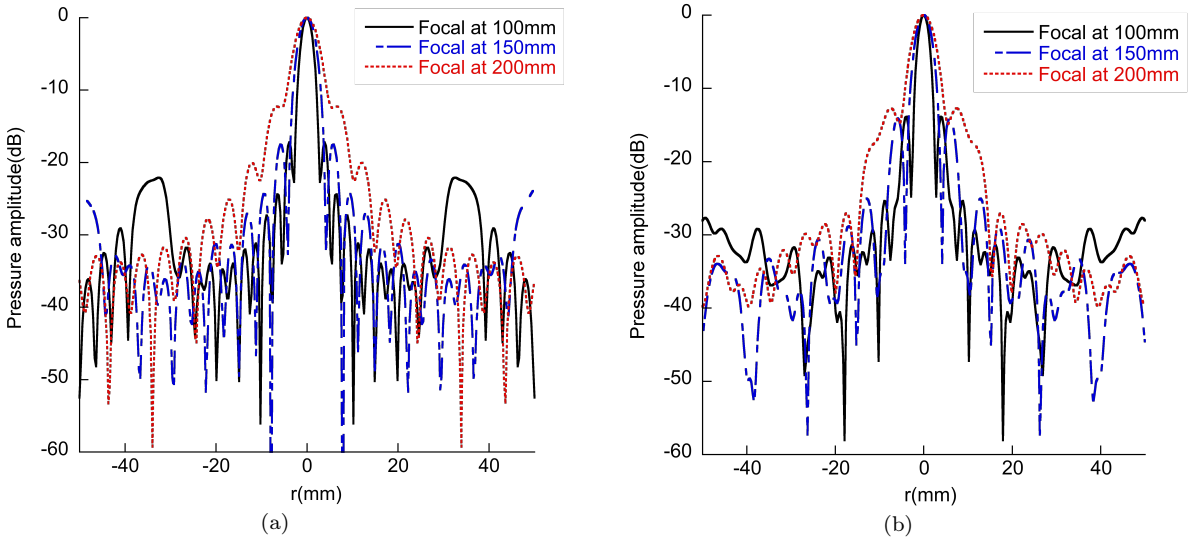

Figure 2.13. Predicted transverse distribution of pressure amplitude (in dB scale) at a distance z equal to the aimed focusing distance, for both types of 8-element annular arrays: (a) type I and (b) type II.

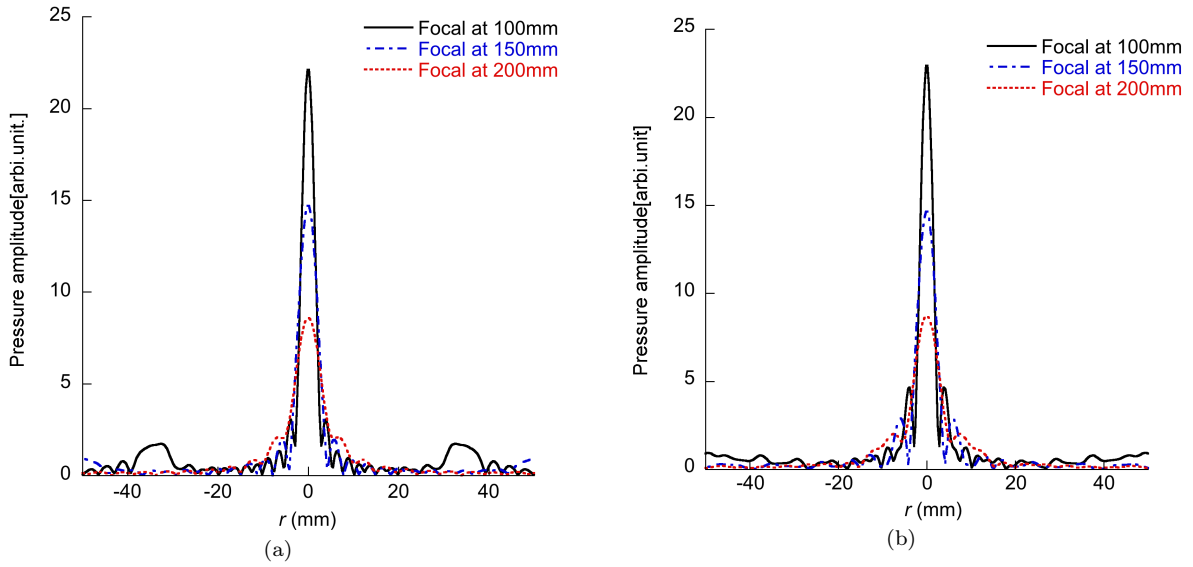

Figure 2.14. Predicted transverse distributions of pressure amplitude (in linear scale) at a distance z equal to the aimed focusing distance, for both types of 8-element annular arrays: (a) type I and (b) type II.

lobe, for MEACUT type I, is equal to $3.34mm$ for $d_f = 100mm$, $4.54mm$ for $d_f = 150mm$, and $6.34mm$ for $d_f = 200mm$. For MEACUT type II, this width is equal to $2.86mm$ for $d_f = 100mm$, $5.40mm$ for $d_f = 150mm$ and $6.67mm$ for $d_f = 200mm$. These width values have been picked-up at the level of maximum pressure amplitude down to $-6dB$. They show that both types of MEACUT produce main lobes with very similar narrow width, at any of the investigated distances. Thus according to the focusing performance of these two types, the type II of MEACUT array is more suitable for NDT applications.

Therefore the simulation results for 8-element annular arrays show that type II performs a better focal amplitude and transverse feature than the annular array type I. In the following, the annular array of type II will be built and characterized as optimized MEACUT. The type II annular array is built with the designing diagram shown in Figure 2.15 and Figure 2.9(b).

2.4 Air-coupled capacitive array: building

The Multi-Element Air-coupled Capacitive (electrostatic) Transducer(MEACUT) was fabricated by machining the aluminium back plate into several sections and by filling the spacing between elements with ultrasound-absorbing material (usually epoxy filling material for its function of mechanically support and its electric and acoustic insulation). Figure 2.15 shows its schematic and Figure 2.16 shows a photography of the fabricated prototype. To focus at a certain distance in front of the annular array, excitation signals applied to each element should be delayed as the time of flight difference to the target distance, according to the phased delay given in Equation 1.8.

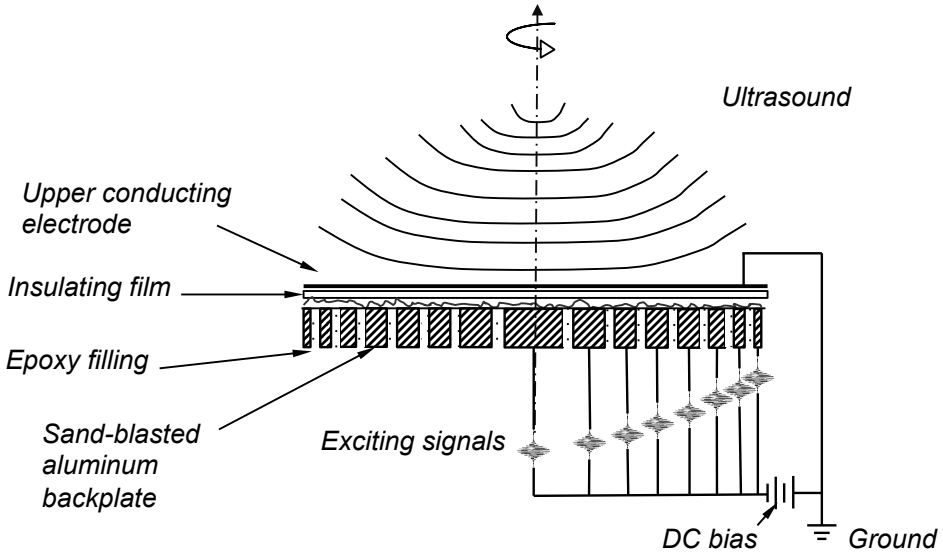

Figure 2.15. Schematic of the multi-element air-coupled capacitive annular array (Type II) and its focus feature (axial symmetrical).

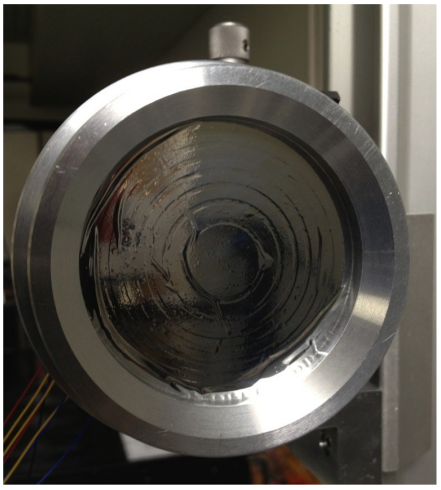

Figure 2.16. Annular MEACUT type II photography.

2.5 Air-coupled capacitive annular array: characterization

The fabricated MEACUT can be characterized with the same method as that used for the characterization of mono-element air-coupled transducer. The following schematic Figure 2.17 shows the measuring experimental setup. A Doppler velocimeter is used to measure the particle velocity at the surface of the membrane, which is placed between the annular MEACUT and the laser probe. The transducer is mounted on a horizontal rail with the membrane and the velocimeter, with a 3 dimensional scanning axes. Each element of the annular array from the transmitter is applied a $100V$ DC bias to stretch the membrane onto the backplate, *i.e.* setting the transmitter array to stand-by. The exciting feeding signals are generated by the Lecœur multichannel OPEN system [110]. This

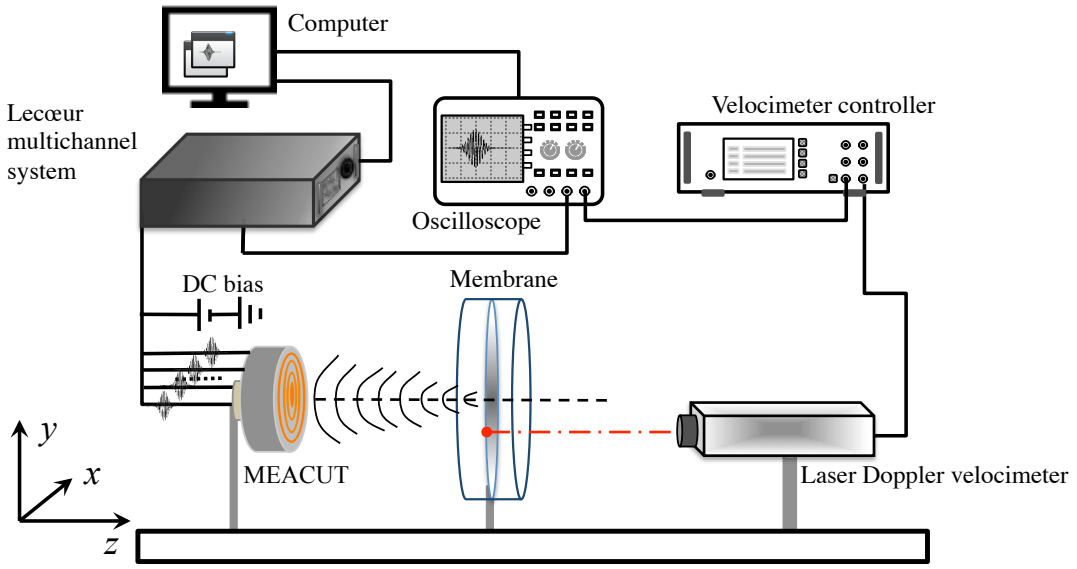

Figure 2.17. Schematic experiment setup for array transmission field characterization.

Lecœur multi-channel generation and receiving system is driven with Matlab [89] script through the application programming interface (API). It is a 128 channel transmitting and receiving processing system, operating either in pulse-echo or pitch catch mode. A function has been programmed to set the exciting signals with proper time delays, aiming to the target focusing distance for the annular array. The synchronizing signal is also generated by the Lecœur system to send to the oscilloscope which is used for measuring the velocity signal from the velocimeter controller. The laser beam is focused at a very small spot on the reflective membrane. The laser Doppler Velocimeter is mounted on a mechanical scanning platform to allow the 2 dimensional axes scanning on the membrane to have a 2D transverse scanning at the membrane surface.

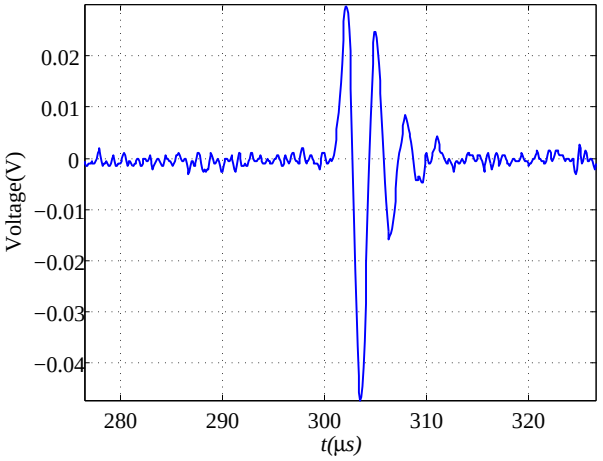

Figure 2.18. Temporal response of centre circular element N°1 at the membrane on-axis distance z =100 mm from the output of the laser Doppler velocimeter.

Acoustic field generated by the annular capacitive array has been characterized to reveal the its frequency properties. The pulse signal excitation measurement is adopted

for fast and easily to obtain the frequency response. The experimental setup shown in Figure 2.17 is now used for measuring the acoustic field frequency response of each individual element in the annular array, and of the whole array at focusing mode with phased shifting. In Figure 2.10(b), the numerical prediction of the on-axis pressure distribution reveals that the far field distance of the array elements to be around $50mm$ at frequency $300kHz$. Thus the measurement distance between the membrane and transducer is set to $100mm$, which is also at far field distance for each individual element in the array. As an example, the temporal output signal of centre circular element N°1 is shown in Figure 2.18. The output voltage is proportional to the normal velocity at the membrane, which is linked to the acoustic pressure produced by the incident wave sent by the MEACUT.

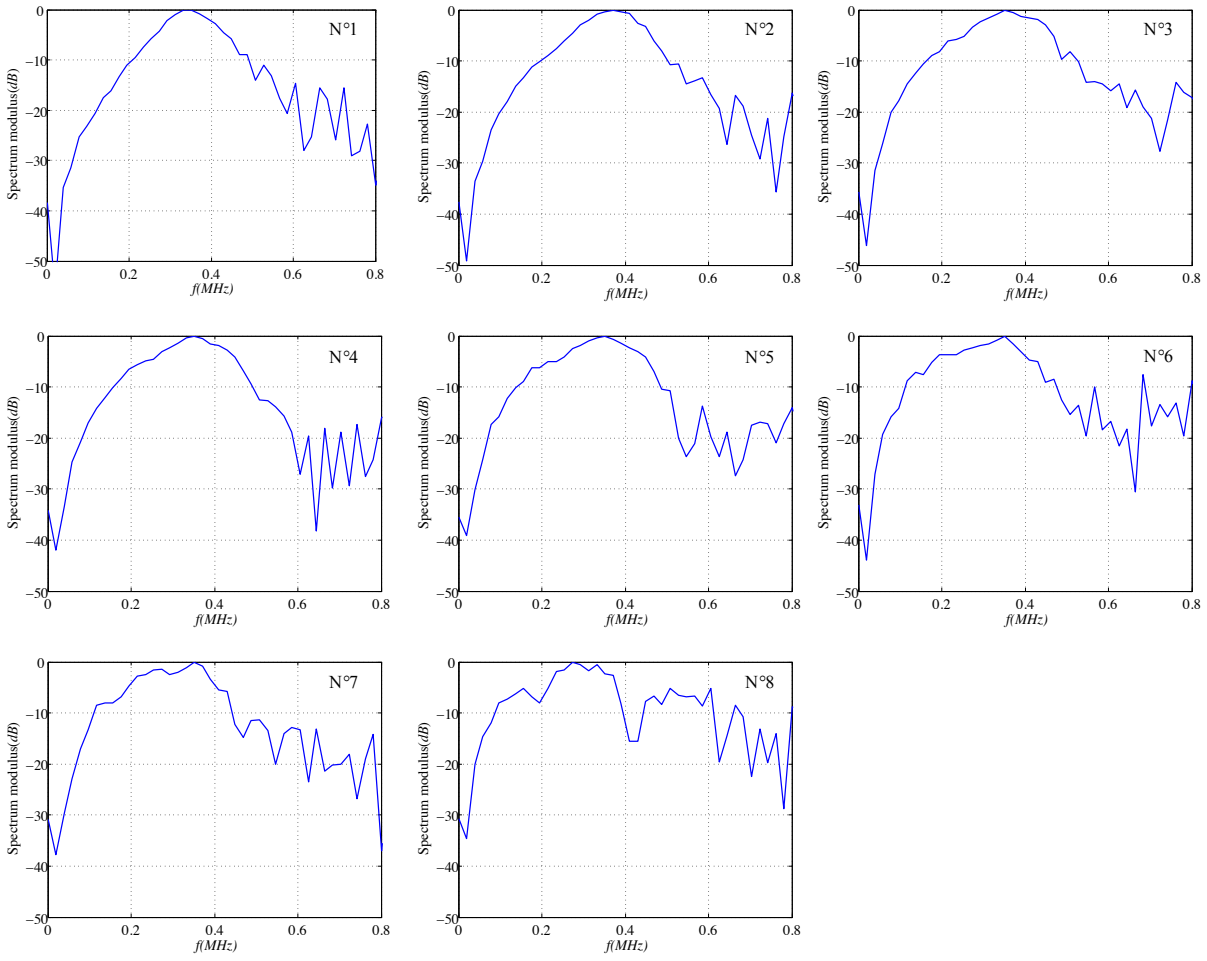

Figure 2.19. Frequency response of acoustic field in air using pulse exciting for individual element in annular MEACUT. The velocity is measureed at the surface of the testing membrane with LDV at the on-axis distance $z = 100mm$.

This temporal signal is Fourier transformed to frequency domain and converted to the frequency response of the transducer with the relation in Equation 2.5 and Equation 2.4. This method is similar to that used for obtaining the acoustic field frequency response of capacitive mono-element transducer in Figure 2.5. The frequency responses of each element in the annular array are shown in Figure 2.19. Similarly, the centre frequencies

are around $370kHz$ for each individual element of the annular MEACUT. Their centre frequency and frequency bandwidth (about 120%-180% for -20dB attenuation) are quite uniform between elements.

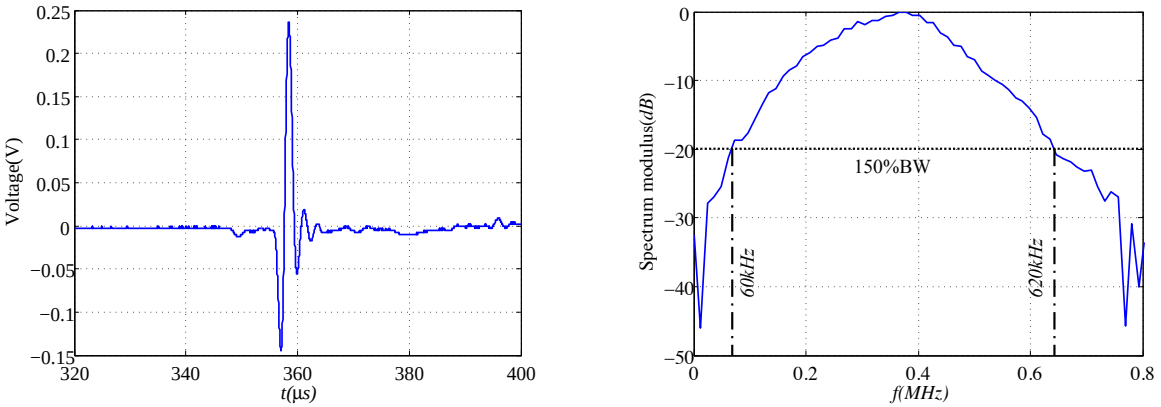

(a) (b)

Figure 2.20. Frequency response measurement using pulse excitation for MEACUT. The velocity measurement is at the surface of the membrane with LDV at the focused axis position $z = 100mm$. (a): Measured temporal output signal of LDV at the testing membrane. (b): MEACUT focused acoustic field frequency response in air.

To investigate the acoustic field frequency response produced by the annular MEACUT in focusing mode, each element of the array is phased delayed to focus at distance z=100mm. The testing membrane is also placed at this distance. The output signal is shown in Figure 2.20(a). The frequency response spectrum of the acoustic field at the focusing spot is shown in Figure 2.20(b), which reveals a very wide frequency bandwidth up to 150% bandwidth relative to centre frequency f=380kHz at the focusing spot. This measurement results demonstrate an excellent frequency bandwidth performance of the annular MEACUT.

2.5.1 Acoustic field profile generated by MEACUT

The KIM method is now used to simulate 8-element annular MEACUT of type II. Experimental measurement of the acoustic profile has been proceeded with the experimental setup described in Figure 2.17. The acoustic beams produced by each separated elements in annular array and by the whole array are investigated to characterize the acoustic performance of MEACUT applied as an transmitter.

2.5.1.1 Acoustic field profile characterization of MEACUT elements

The annular array is characterized using the laser Doppler vibrometry. For this purpose, the annular elements are excited respectively with pulse signal for measuring their radiation acoustic field in air. The temporal signals are Fourier transformed into

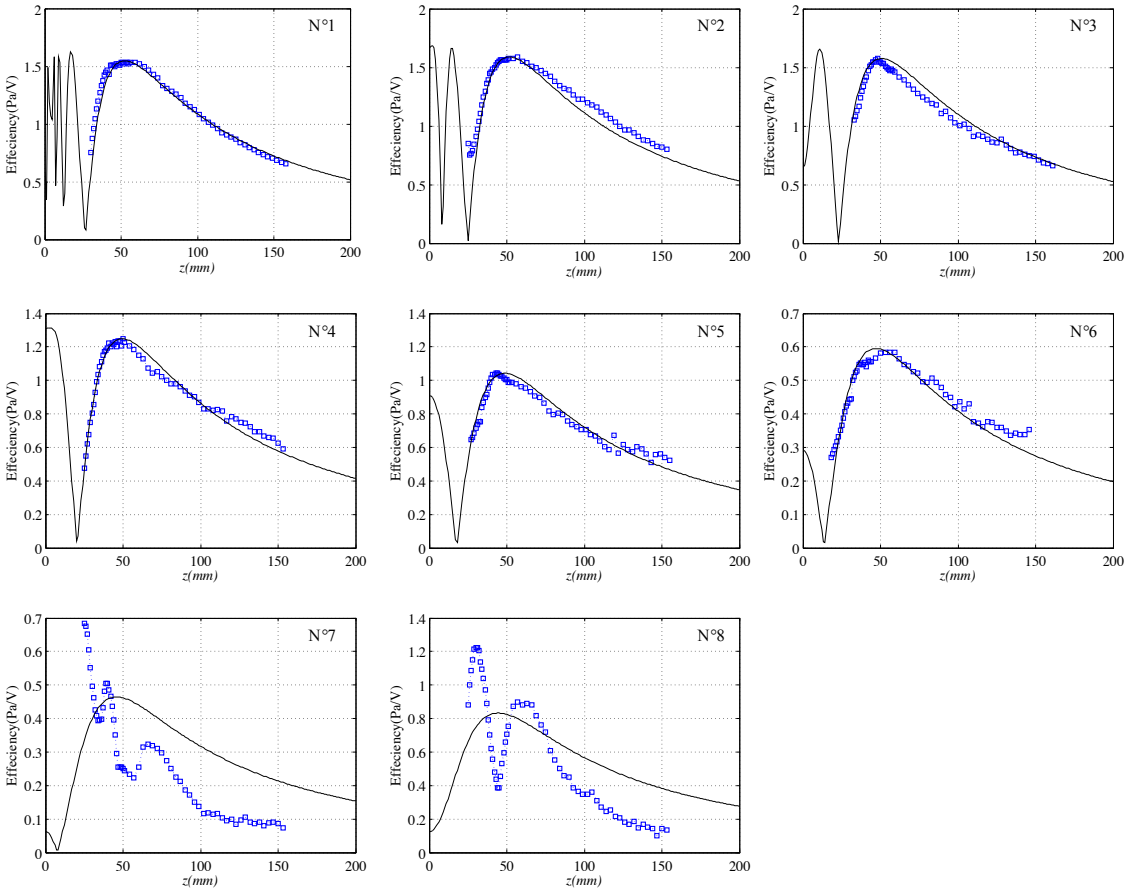

Figure 2.21. On-axis acoustic field pressure distribution produced by annular MEACUT elements at frequency $f = 300kHz$: Simulation with Kirchhoff integration method(KIM) field pressure data (solid line $-$) , on-axis measured pressure amplitude with pulse excitation (non-filling square $\square$). Element number N°1$\sim$ N°8 are numbered from its centre to the edge of the transducer.

frequency domain and converted to the pressure field response by applying Equation 2.5. The acoustic fields produced by each elements at a given frequency $f = 300kHz$ are simulated with analytical KIM model developed in Chapter 1. The type II array element dimensions are set as those described in Figure 2.9(b). All the simulations are processed at one single frequency, corresponding to time-harmonic continuous wave excitation.

The on-axis acoustic pressure fields produced by each element are shown in Figure 2.21. These elements are numbered from the centre one (N°1) of the array to that at the edge of the array (N°8). The experimental measurement results agree well with those simulated with KIM model from N°1 to N°6. However, for the two elements which are close to the transducer edge, discrepancies appear between the predicted distributions and experimental results. The acoustic field on-axis distributions for these two annular elements do not reveal near field or far field profiles as the other annular elements do. This is supposed to be coming from the acoustic wave reflection of the beams produced by these 2 elements on the metallic shell of the transducer, which is very close to them.

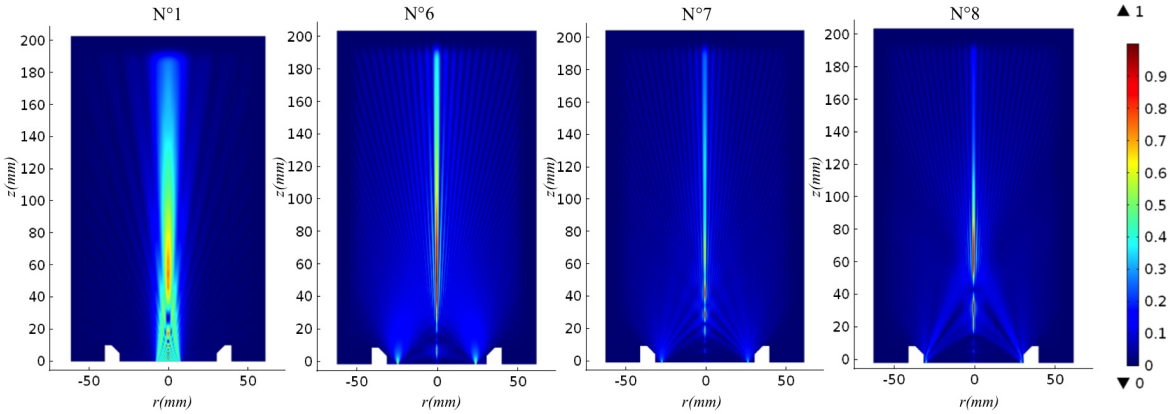

Figure 2.22. Acoustic field pressure distributions predicted by axisymmetric FE model for annular MEACUT elements at frequency $f = 300kHz$: FE model takes into account the transducer metallic shell to simulate its reflection effect on the acoustic field. Acoustic pressures are normalized for each element (N°1, N°6, N°7 and N°8) for comparison purpose.

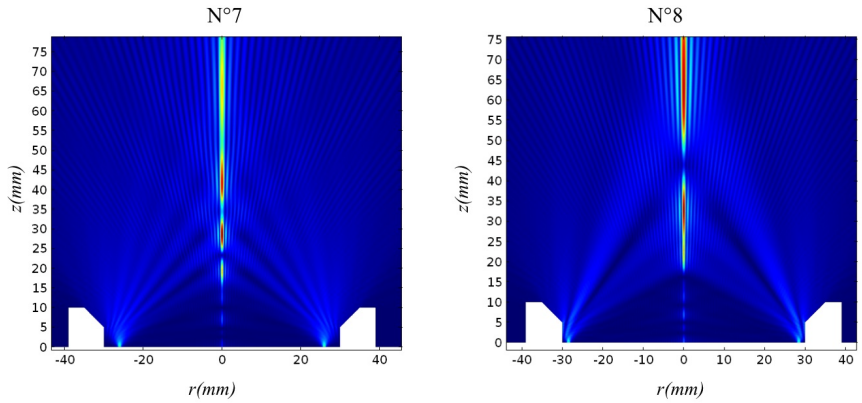

Figure 2.23. Zoom in acoustic field pressure distributions for elements N°7 and N°8 simulated with air-solid coupling FE axisymmetric model with consideration of the transducer metallic shell.

In order to check that assumption, the axisymmetric fluid-solid coupling FE model developed in Chapter 1 is used to simulate the influence of the metallic shell on the acoustic field produced by each element. This model takes into account the dimension and material properties of the metallic shell by applying air-solid coupling conditions at the interfaces. The acoustic field pressure produced by elements N°1, N°6, N°7 and N°8 are displayed in Figure 2.22. It is clear that the acoustic pressure fields produced by N°1 and N°6 are little affected by the pressure of the metallic shell, which is remote enough to produce reflections of the acoustic fields generated by these two elements. However, there are large wave reflections for the elements N°7 and N°8 from the metallic shell. Near field zoom-in displaying the pressure amplitude of these two elements is shown in Figure 2.23. This reveals non-negligible interference effect from the shell to the on-axis pressure distribution. These effects could not be negligible for these two elements which are close to the shell, which causes the discrepancies between the analytical KIM predicted

distributions and the measured data shown in Figure 2.21.

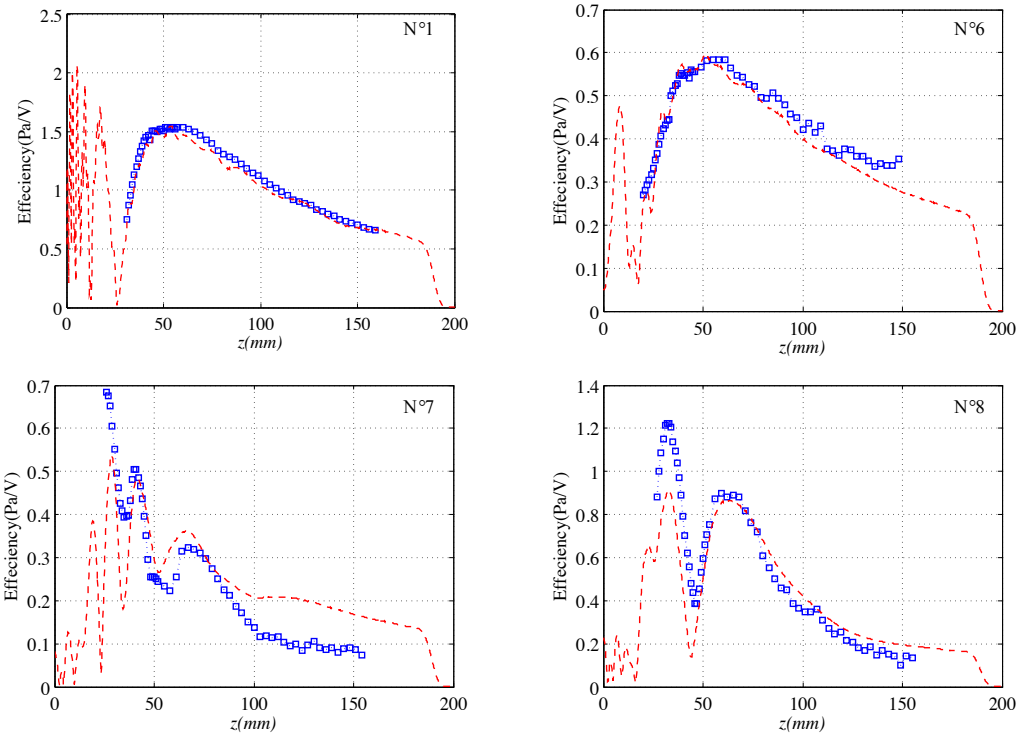

Figure 2.24. Annular MEACUT element acoustic field on-axis pressure measurement: Simulation with finite element method field pressure data (dashed line −−) , on-axis measured pressure amplitude with pulse excitation (non-filling square □). Element N°1(centre circular element), N°6, N°7 and N°8 are demonstrated as the examples.

For further validating the reflection effects from the metallic shell of the transducer, the on-axis pressure distributions predicted by axisymmetric FE model are compared with the measured data. Figure 2.24 shows these comparisons for elements N°1, N°6, N°7 and N°8. The measured acoustic fields agree well with the FE predictions. Thus for the outer two annular elements N°7 and N°8, this reflection effects from the metallic reflector is confirmed and obviously the analytical KIM method does not take this effect into account. However, since the advantages of the analytical method are significant comparing with FEM, especially for the calculation of acoustic fields in air, further investigation is going to be made to double check the applicability of the analytical KIM method to simulate the 8-element MEACUT.

2.5.1.2 Focused annular phased array acoustic field characterization

The total acoustic field generated by the annular array is the summation of all those radiated by the elements with proper time delays. Thus to obtain the total acoustic field prediction from KIM, the superposition principle in Equation 1.8 and Equation 1.9 will be used for the KIM to model each element of the array, and the acoustic beam produced by the whole array in turn.

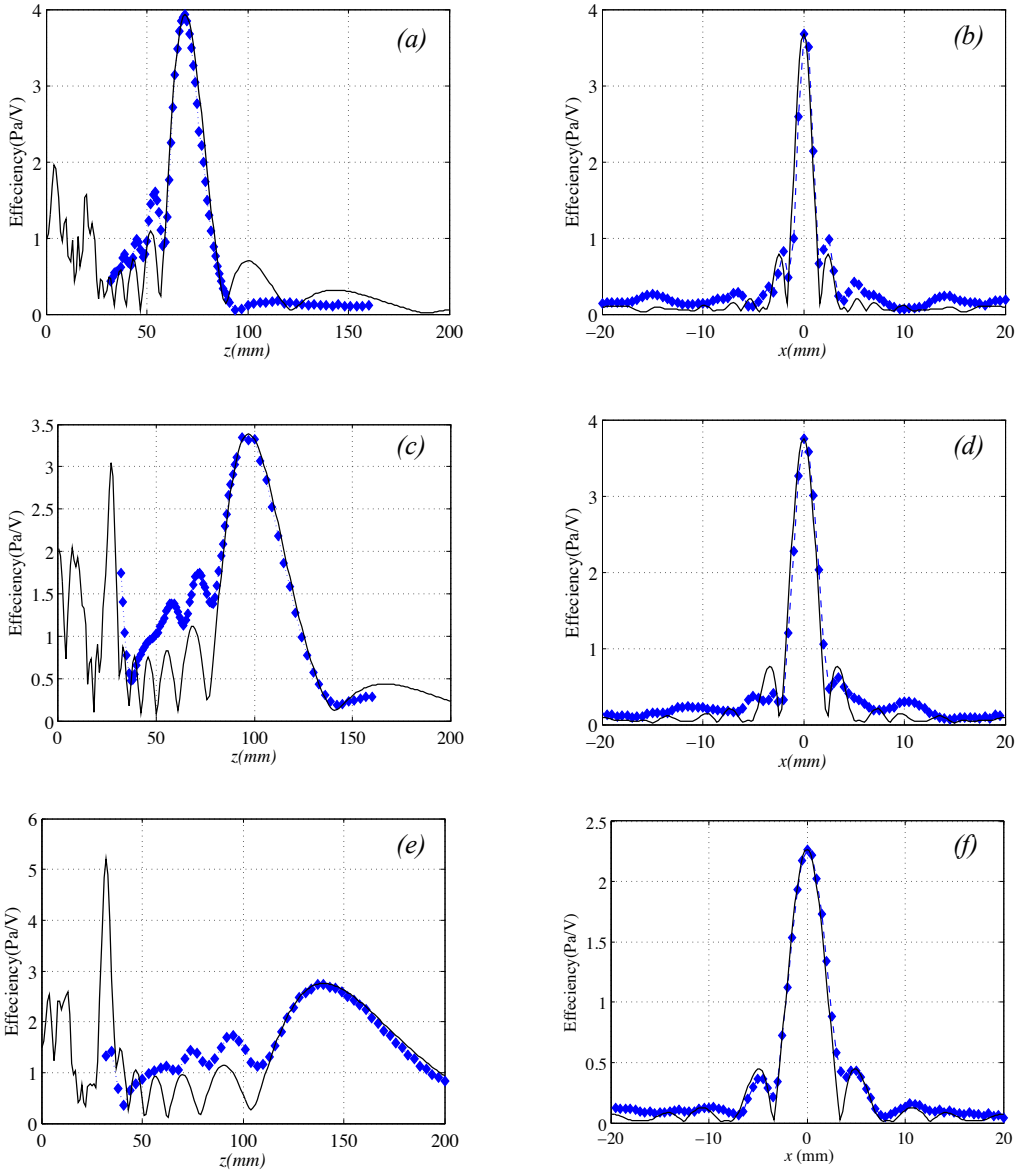

Figure 2.25. Ultrasonic field pressure distributions for 8-element annular MEACUT predicted by KIM model (solid line −) and measurements results (dashed diamond −♦−). Left column is for on-axis distribution (along z) and right column is for transverse distribution (along r) at three different monitoring distances equal to the target focusing distances, which are: (a, b) $f_l = 70mm$, (c, d) $f_l = 100mm$ and (e, f) $f_l = 150mm$.

Experimental measurement with laser Doppler velocimeter method has been processed for the characterization of the spatial focusing properties of this annular array. For the MEACUT, its focusing distance was set at $z = 70mm$, $z = 100mm$ and $z = 150mm$ successively. The on-axis pressure amplitude for these focusing distances and transverse pressure distributions at focusing distance are shown in Figure 2.25. The focusing acoustic fields pressure measured in experiments agree well with those predicted from analytical KIM model for these three distances. This confirms that the analytical KIM model can be reliably used to simulate and predict the acoustic field produced by multi-element sources and also that this annular MEACUT has been properly fabricated and behaves

as expected. Even if the transducer metallic shell is not taken into account in this model. As what we have seen previously, its effect is not negligible when only elements N°7 and N°8 are considered. However, as what has been shown in Figure 2.25, this effect can be neglected when the whole set of elements is considered.

With the same computer and software configurations as those used in Section 1.4, the efficiencies of KIM and axisymmetric air-solid FE model are compared by testing their time-consuming under the same calculation task for the 8-element MEACUT. The area of the FE model shown in Figure 2.22 is $60mm \times 200mm$, consisting of 626496 elements and 1254813 DOFs. The time-consuming for calculating the acoustic field generated by this 8-element MEACUT with FE model is $1mn4s$. While under the same discretization level and precision the KIM model takes $3mn55s$ to calculate the whole field pressure generated by 8-element MEACUT in this 2D axisymmetric area. However, if the task is to obtain the pressure at a certain section in the field (*e.g.* at the focusing distance shown in Figure 2.25), the time-consuming of FE model keeps the same while that of KIM takes $3.6s$ for the prediction of the pressure along transverse at a certain distance. Thanks to the great advantages of fast calculation, easy implementation and accuracy, this KIM model will be applied later for simulating the NDT inspection system based on the use of the MEACUT.

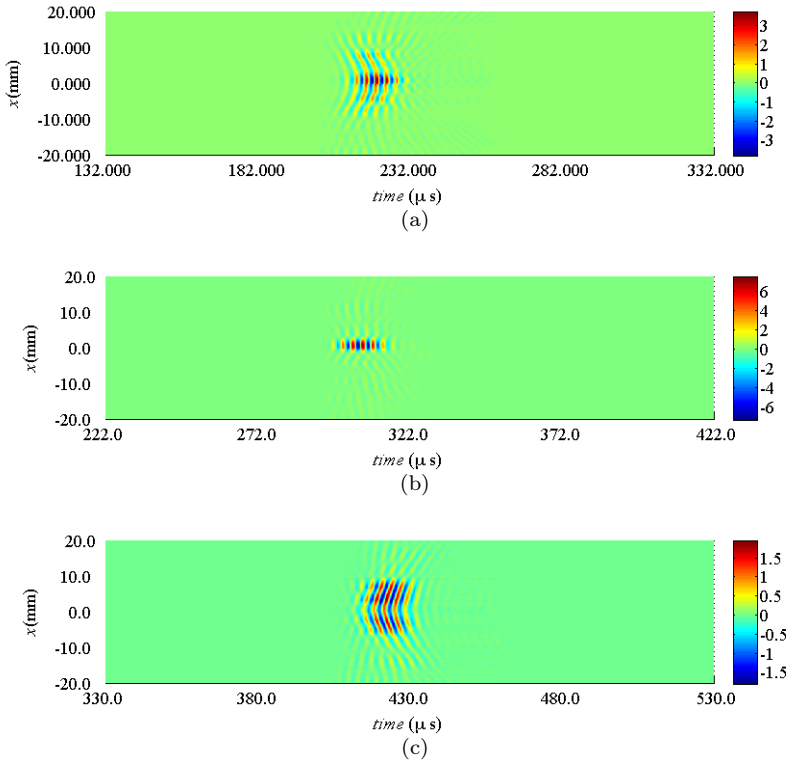

Figure 2.26. Transverse B-scan measurement for target distance $f_l = 100mm$. Vertical axes is the transverse position (along x), horizontal axes is the time elapse of the propagating wave; monitoring distance equals to (a): $z = 70mm$; (b): $z = 100mm$ and (c): $z = 130mm$.

Further, measuring the efficiency of the focusing transducer, the pressure efficiency at the focusing spot, *e.g.* $f_l = 100mm$, is $3.45Pa/V$. In the experiment, the applied voltage amplitude is $25V$, so the acoustic efficient pressure value at the focusing spot is $86.25Pa$ ($z = 100mm$). It is much higher than the acoustic pressure generated by the individual element of the array, for instance, the acoustic pressure generated by the centre element N°1, which is equal to $37.67Pa$. This acoustic pressure is sufficient for air-coupled NDT to get well recognized SNR.

The focusing acoustic field has been also characterized for its transverse wave front properties. The applied excitation signal is a 10-cycle sinusoidal Gaussian windowed tone burst to reveal the local wave front of the focusing distance. A B-scan method is used for transversely monitoring the temporal signals. These are shown in Figure 2.26, which displays the wave fronts when the target focusing distance is $f_l = 100mm$, at three different monitoring distances: $z = 70mm$ (distance shorter than the focusing target), $z = 100mm$ (distance equals to focusing target), $z = 150mm$ (distance beyond the focusing target). The beam spreading can be observed along x direction both at near and far distances. At focusing distance $z = f_l = 100mm$, the wave front profile in Figure 2.26 (b) illustrates that the beam at focal point has locally plane wave front, which is essential for some further applications, which require the plane wave condition to be satisfied.

2.6 Summary

In this chapter, the previous developed analytical KIM model has been used as a tool to simulate and optimize the annular array and to decide its dimensional parameters. Based on the numerical optimization results, the type II MEACUT with the feature of the same-area elements has been designed and built. This MEACUT then has been characterized regarding its frequency response, its acoustic field radiation profile along z(axial) and r(radial) axis. These experimental results on the acoustic field produced by the elements of the array have been compared with the analytical KIM predictions. There have been disagreements between the measured and simulated on-axis pressure distributions for the outer two annular elements. The reason for this discrepancy comes from the reflection of the field these outer elements generate on the metallic shell. By modelling the reflection influence of the shell in FE model, the on-axis pressure distributions agree well. However, the discrepancy between KIM and experimental results observed for singular elements does not significantly influence the KIM results obtained for the total phased array. Thanks to the advantages of KIM, this integral method will be used in the next chapters for modelling the acoustic field in air produced by axisymmetric MEACUT for NDT purposes.

Chapter 3

Rayleigh integration method and 3D hybrid model

3.1 Introduction

In the previous chapters, the analytical KIM method to simulate the acoustic field produced by axisymmetric transducer was introduced and validated numerically and experimentally. Then an annular MEACUT has been optimized and designed under the assistance of this numerical tool. The MEACUT has been built and characterized to investigate its frequency response and acoustic field profile performances. The experimental results showed that the MEACUT performs to be a high-efficiency, wide frequency bandwidth transducer with the capability of dynamic focusing under phase control. An overall air-coupled inspection system consists in one transmitter and one receiver, thus in this chapter, a 3D numerical method will be developed to simulate the whole system, *i.e.* both transmitter and receiver and acoustic propagation in the inspected plate.

The analytical KIM model is used to predict the acoustic field produced by the axisymmetric transmitter, while the acoustic field propagating in air from the tested sample to the receiver is predicted by a general Rayleigh integration method (RIM). The 3D RIM model will be derived from the Green's function solution of the Helmholtz-Kirchhoff integral formula at the hard boundary. The formula of 3D RIM allows an arbitrary velocity distribution input at the radiation interface (*e.g.* the rear surface of the plate), thus can be used as the numerical tool to predict the acoustic field from the plate to the air-coupled receiver. This 3D RIM model is then validated using the axisymmetric FE model by imposing a non-piston velocity distribution at the boundary which simulates the vibrating plate surface with arbitrary mode. Based on this, a 3D KIM-FEM-RIM hybrid model is proposed and built combining the integral model and 3D FE model to fully simulate NDT experiments for plate through-transmission inspection.

The schematic diagram of 3D KIM-FEM-RIM hybrid model is shown in Figure 3.1. Simulations are all performed in frequency domain to avoid calculation with numerous time steps. The process is similar to which has been realised in 2D cases (Appendix B).

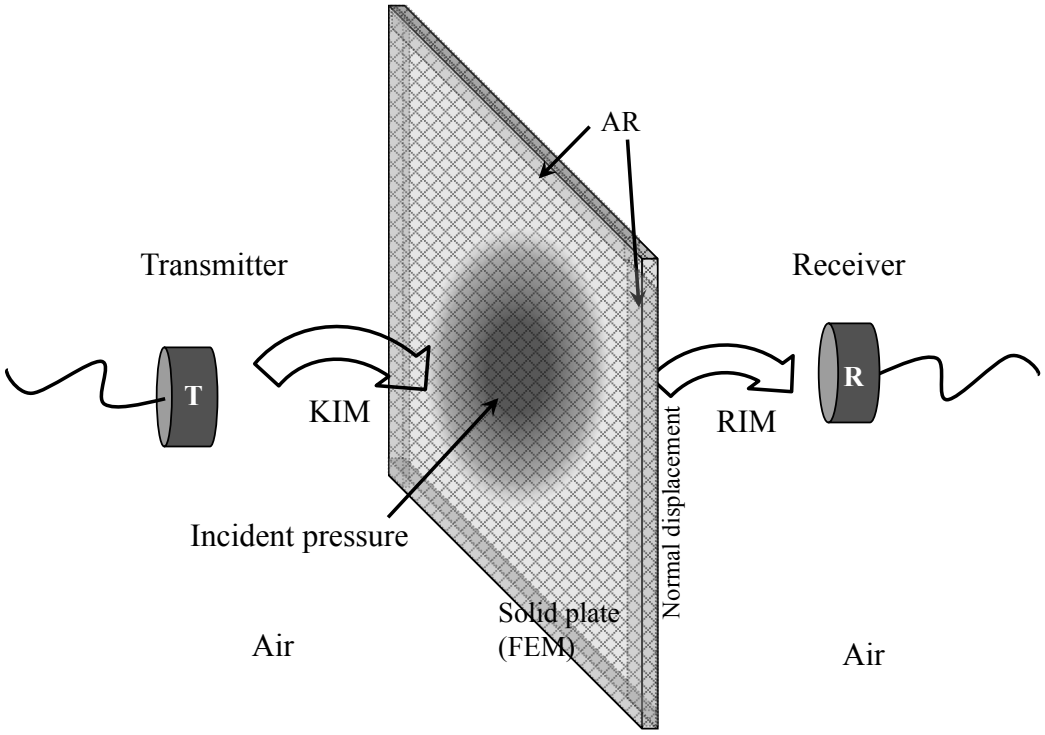

Figure 3.1. Schematic diagram of 3D KIM-FEM-RIM hybrid model.

The acoustic field produced by an axisymmetric piston transmitter (ACUT or MEACUT) is calculated with the axisymmetric KIM model, which had been developed and validated in Chapter 1. Proper phase delays need to be implemented at each element of the MEACUT to perform a desired focusing acoustic beam profile. The resulting complex pressure calculated by KIM at the solid plate front surface is extracted as a sectional pressure distribution in the field. These pressure distribution data must be mapped to impose a pressure input at the plate front surface *i.e.* convert the pressure data from cylindrical coordinate to Cartesian coordinate. As the input of the 3D solid FE model, the pressure distribution from KIM will be used as the excitation at the front surface of the plate. The displacement field in the 3D solid plate is predicted with the 3D FE model. Since all the displacement and stress in the plate can be known from the FE model, the normal displacement at the back surface of the plate can be monitored and imported to 3D RIM model to predict the acoustic field at the receiver in air. The final output signal of the receiver is then the 2D surface integration across the receiver surface area. Through those procedures of the hybrid model, the full acoustic process about the generation, propagation and receiving can be simulated from the transmitter to the receiver.

In this case, the setting of absorbing regions is of great importance, as shown in Figure 3.1, for modelling an infinity large plate and for suppressing all reflections from the plate edges in 3D situations. In 2D models wave propagation in air is either included in the model (FE model) or replaced by analytical models (RIM-FEM-RIM hybrid model) within the computing capability. While in 3D models, the simulation of the wave propagation in air is omitted from the FE part for reducing the model size and hybrid solution becomes

unavoidable. Therefore the 3D KIM-FEM-RIM hybrid model is achieved in this work for simulating the whole inspection system, which includes the air-coupled transmitter, the propagation in the air, through the tested plate component and the air-coupled receiver. However, the 2D hybrid model has also been achieved and is presented in Appendix B.

3.2 Rayleigh integration method

The concept of Rayleigh integration method comes from Huygens principle in optics [74]. It resumes that the acoustic field at an arbitrary field point in medium is the integration of all the sperical acoustic waves produced by the point of the elements on the source, which could be represented by a green source function. By involving the source function into the Helmholtz-Kirchhoff integral equation, which represents a conservation law for the wave energy flux that passes through a closed surface [111], the spatial pressure can be deduced from the knowledge of distributed acoustic pressure or displacement at the surface.

The Rayleigh integral method can describe the acoustic problem for non-uniform velocity surfaces at different boundary conditions. In the next section, this Rayleigh integral method is used for the numerical modelling of the acoustic field travelling from a plate sample to an air-coupled receiver in 3D conditions. It will be shown to be an efficient analytical method to predict the pressure in air produced by the vibrating plate.

3.2.1 Rayleigh Integral method for 3D modelling

The acoustic field generated by a harmonic source immerged in an unlimited homogeneous isotropic fluid medium is described by the Helmholtz-Kirchhoff integral equation [112]. A plane source S_0 with an arbitrary shape, is embedded in an infinite planar rigid baffle as in Figure 3.2. This boundary assumption is known as Rayleigh's approximation, which is in practice fulfilled in air acoustics when a vibrating membrane is placed into a rigid metallic shell. A general solution for the radiated acoustic pressure field is given by the Helmholtz-Kirchhoff integral formula [111]:

$$p(\boldsymbol{r}) = \iint_{S_0} \left[G^*(\boldsymbol{r}|\boldsymbol{r_0}) \frac{\partial p(\boldsymbol{r_0})}{\partial n(\boldsymbol{r_0})} - p(\boldsymbol{r_0}) \frac{\partial G^*(\boldsymbol{r}|\boldsymbol{r_0})}{\partial n(\boldsymbol{r_0})} \right] dS(\boldsymbol{r_0}) \tag{3.1}$$

in which the vector $\boldsymbol{r}$ describes the field point from the origin: $\boldsymbol{r_0} = \overrightarrow{ON}$ and $\boldsymbol{r} = \overrightarrow{OM}$, N is the point at the source surface, $p(\boldsymbol{r})$ is the acoustic pressure at point M, $n(\boldsymbol{r_0})$ is a unit vector normal to the source surface, pointing to the point in the medium. $dS(\boldsymbol{r_0})$ is a surface element, which is decided by the integration method. And $G^*(\boldsymbol{r}|\boldsymbol{r_0})$ is the Green's function for harmonic acoustic excitation.

For the radiation problem from a capacitive transducer or solid plate to the air medium that this work involves, the radiation source medium could be considered as an

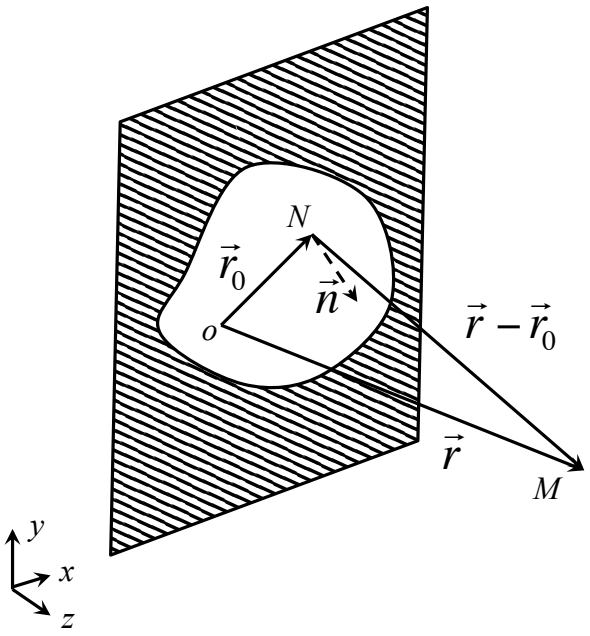

Figure 3.2. Surface source radiation Rayleigh integration model and its coordinate.

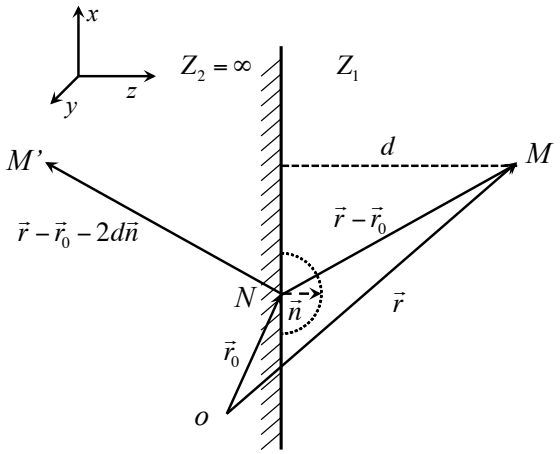

Figure 3.3. Rayleigh integral with acoustic source in a rigid plane boundary

acoustically hard boundary ($Z_2/Z_1 \simeq \infty$), as shown in Figure 3.3. Z_2 is the acoustic impedance of the source, while Z_1 is the acoustic impedance of the wave propagation medium. Thus the Green's function of this form should be considered as the summation of the point source M and its in-phase mirror source M' corresponding to the boundary:

$$G^*(\boldsymbol{r}|\boldsymbol{r_0}) = G(|\boldsymbol{r}-\boldsymbol{r_0}|) + G(|\boldsymbol{r}-\boldsymbol{r_0}-2d\boldsymbol{n}|) \tag{3.2}$$

where d is the normal distance from the observation point M to the boundary plane. We could derive the boundary radiation condition at the boundary by considering the point M is close to the boundary. For the observation point M at the boundary: $G(|\boldsymbol{r}-\boldsymbol{r_0}|) = G(|\boldsymbol{r}-\boldsymbol{r_0}-2d\boldsymbol{n}|)$. So the normal derivative of the equation disappears and relation of the pressure at Equation 3.1 takes the form:

$$p(\boldsymbol{r}) = 2\iint_{S_0} G(\boldsymbol{r}-\boldsymbol{r_0})\frac{\partial p(\boldsymbol{r_0})}{\partial n(\boldsymbol{r_0})}dS(\boldsymbol{r_0}) \tag{3.3}$$

Since the acoustic pressure existing on the surface is of no influence to the field formation in the back half-space, the Green's function at the observation point M is:

$$G(|\boldsymbol{r}-\boldsymbol{r_0}|) = \frac{exp(-jk\,|\boldsymbol{r}-\boldsymbol{r_0}|)}{4\pi\,|\boldsymbol{r}-\boldsymbol{r_0}|} \tag{3.4}$$

in which k is the wave number of acoustic wave in medium Z_1, and $k = 2\pi/\lambda = \omega/c_0$, ω is the angular frequency and c_0 is the sound velocity in medium. This equation gives the integration known as Rayleigh's formula [71], which describes the radiation of a source in a rigid baffle:

$$p(\boldsymbol{r}) = \frac{1}{2\pi}\iint_{S_0}\frac{\partial p(\boldsymbol{r_0})}{\partial n(\boldsymbol{r_0})} \times \frac{exp(-jk\,|\boldsymbol{r}-\boldsymbol{r_0}|)}{|\boldsymbol{r}-\boldsymbol{r_0}|}dS(\boldsymbol{r_0}) \tag{3.5}$$

Specifically if the radiation source, just as in the case of air-coupled problem, is more rigid than the surrounding medium and vibrates uniformly, then the displacement of the boundary plane, *i.e.* $\partial p/\partial n$ is uniformed over the boundary plane S_0, so:

$$\frac{\partial p(\boldsymbol{r_0})}{\partial n(\boldsymbol{r_0})} = -jkp_0 \tag{3.6}$$

where p_0 is the boundary pressure at the source surface. So the relation becomes:

$$p(\boldsymbol{r}) = -\frac{j}{\lambda}p_0\iint_{S_0}\frac{exp(-jk\,|\boldsymbol{r}-\boldsymbol{r_0}|)}{|\boldsymbol{r}-\boldsymbol{r_0}|}dS(\boldsymbol{r_0}) \tag{3.7}$$

According to the relation between pressure in the fluid p and particle velocity ν, with the plane wave assumption, the relation could be derived as:

$$\frac{\partial p}{\partial n} = j\omega\rho\nu_n \tag{3.8}$$

in which ν_n is the normal velocity of the particle in the medium at the interface, and ρ is the density of the medium.

In Cartesian coordinate the Rayleigh integral shown as in Figure 3.2, could be performed as following:

$$p(x,y,z) = \frac{1}{2\pi}\int_{x_0}\int_{y_0} j\omega\rho\nu_n\frac{exp(-jk\sqrt{(x-x_0)^2+(y-y_0)^2+z^2})}{\sqrt{(x-x_0)^2+(y-y_0)^2+z^2}}dx_0dy_0 \tag{3.9}$$

where the observation point (x,y,z) is in the surrounding medium, and the boundary surface is at plane $z=0$, the radiation source point is $(x_0,y_0,0)$. This is the general expression of Rayleigh integral in 3D situation, which allows the calculation of pressure distribution from the radiation of a rigid object with an arbitrary velocity distribution.

The method will be used as the prediction of the acoustic field generated by a solid plate radiating in the air, where the solid plate can be regarded as solid object with sufficient hard impedance because of the large impedance difference between it and the air media.

3.2.2 Rayleigh integration method: validation

The 3D Rayleigh integration method, as presented in Equation 3.9, is a 3D expression of the acoustic pressure generated by a rigid object with arbitrary velocity motion of its surface. This RIM model needs to be validated before any further use. Therefore, the axisymmetric FE model introduced in Section 1.3 will be used to be the validation model. This FE model, as shown in Figure 1.3(a), has been used to validate the axisymmetric KIM model in Section 1.4 and has been shown to provide good agreements with the KIM model.

To validate the 3D RIM model, a non-piston velocity distribution is imposed at the source boundary. Without loss of generality, a Gaussian-windowed sinusoidal shaped distribution *i.e.* $f(r) = e^{(-\frac{r-2}{10})^2} sin(2\pi r)$, as shown in Figure 3.4, has been imposed at the boundary in Figure 1.3(a) between the origin point and $r = 10mm$. Thus the modelled object is a circle disk with $10mm$ in radius and its surface distribution along radial is that shown in Figure 3.4.

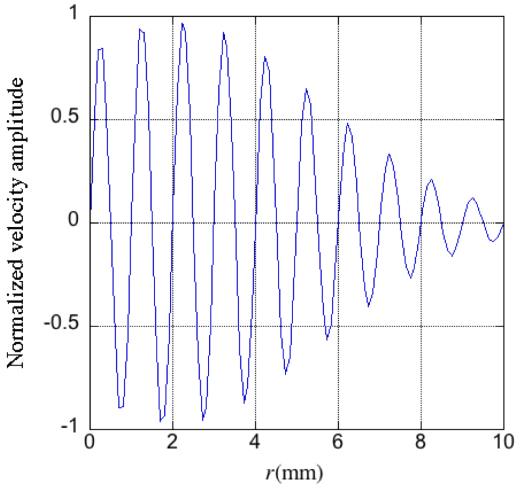

Figure 3.4. Velocity distribution imposed at the boundary as a radiating acoustic source in axisymmetric FE model.

The FE model has been solved to get the acoustic field generated by this non-piston axisymmetric disk. The calculated pressure amplitude distribution across (r, z) is shown in Figure 3.5(a). For the 3D RIM model, the velocity distribution, *i.e.* Figure 3.4, has been converted to be a 2D surface velocity distribution in (x, y) from the radial distribution along $(r, z = 0)$ and then imported to Equation 3.9 for the prediction of the spatial pressure distribution in 3 dimensional condition. A sectional distribution across (x, z) of the 3D pressure predicted by RIM is shown in Figure 3.5(b).

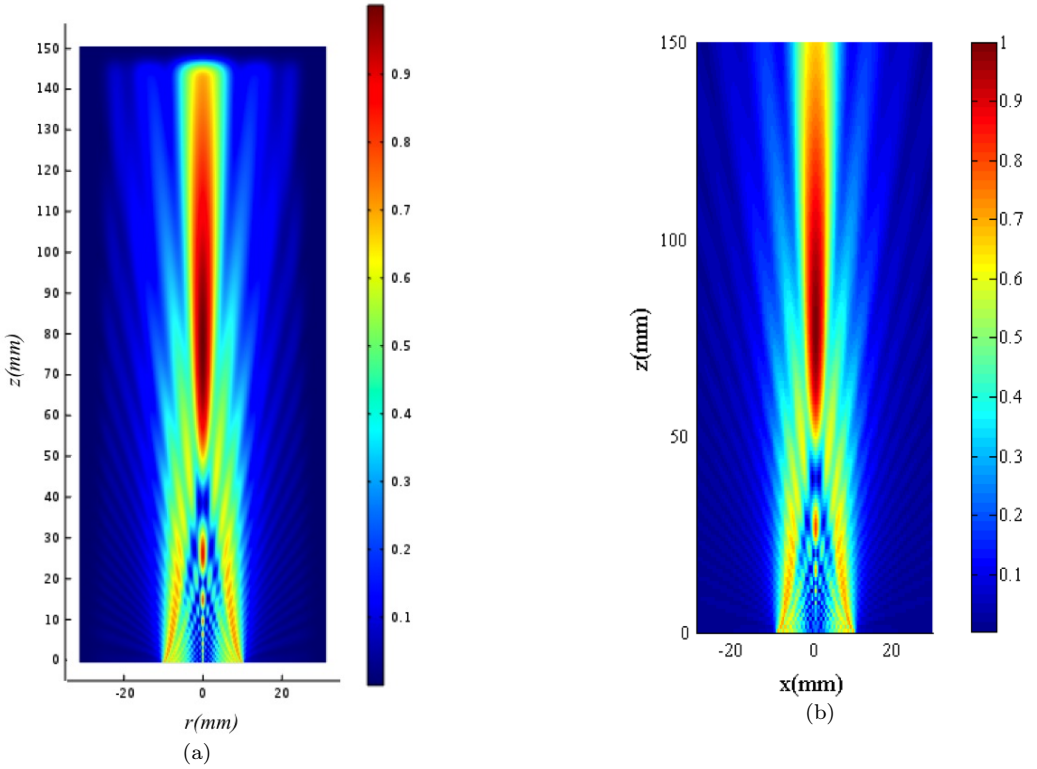

(a) (b)

Figure 3.5. Acoustic pressure distribution produced by non-piston disk source, predicted by (a): axisymmetric FE model across (r, z); (b): 3D RIM model across the section (x, z) when $y = 0$. The acoustic pressure amplitudes are normalized for comparison between both models.

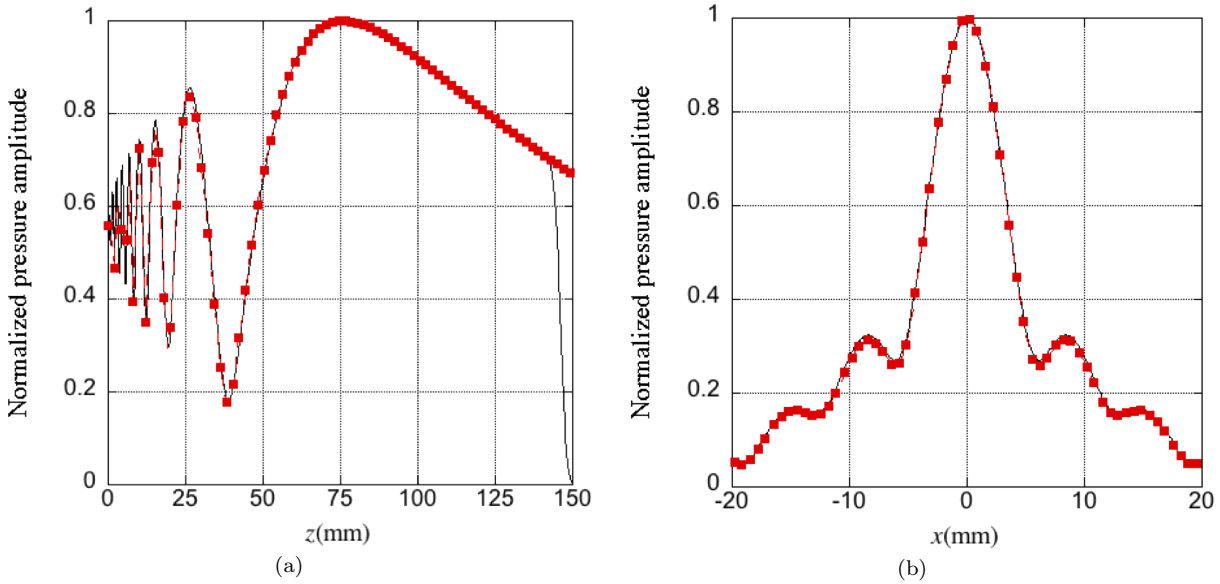

(a) (b)

Figure 3.6. Comparison of the pressure amplitude predicted by 3D RIM model (dashed square –■–) and axisymmetric FE model (solid line –) with non-piston source velocity. the on-axis (a) and transverse at distance $z = 100mm$ (b).

Visually both pressure distributions shown in Figure 3.5 agree well between the axisymmetric FE model (a) and 3D RIM model (b). For a better comparison and validation, the on-axis pressure distributions obtained from these two models are compared in Figure 3.6(a), and also the transverse pressure at distance from the active surface $z = 100mm$, in Figure 3.6(b). The predictions between the axisymmetric FE model and the 3D RIM model agree well from the point of view of field distribution.

In the aspect of calculation time, the axisymmetric FE model takes the same time with those in Section 1.4, *i.e.* $14s$, whether the source is piston or non-piston. While the 3D RIM model spends $5.6s$ for the calculation of the transverse field. For a full sectional distribution across xz plane, as in Figure 3.6(b), the RIM model takes $1396s$ to calculate the same number of sampling point as that in FE model. This is the reason why the efficient Kirchhoff model is necessary and essential in the prediction of acoustic field produced by MEACUT. However, the RIM model is needed to predict the field radiated by the rear surface of the plate, which is modelled to be a non-piston acoustic source. Through this non-piston case, the 3D RIM model is validated and can be used to be part of the 3D hybrid model, which will be developed further down.

3.3 3D KIM-FEM-RIM hybrid model

The schematic diagram of 3D KIM-FEM-RIM hybrid model has been shown in Figure 3.1. The configuration of an ultrasonic plate inspection NDT system includes: a transmitter, a solid plate and a receiver. Thus the acoustic process of these parts involving the generation, propagation and reception of acoustic waves are solved by KIM, FEM and RIM models, respectively.

3.3.1 Axisymmetric KIM model for transmitter

The acoustic field generated by ACUT or MEACUT is calculated with analytical KIM model, which had been developed and validated in Chapter 1. This axisymmetric model gives the acoustic field distribution in an axisymmetric cylindrical coordinate system under coordination variables: (r, z). Thus proper data mapping needs to be operated for those discrete pressure distribution data to convert its coordinate to 3D Cartesian system: *e.g.* (x, y, z). The incident air borne pressure distribution relative to the solid plate is a series of discrete data on the plate front surface. As a specific situation of normal incidence, the data set revolution can be done with transverse acoustic pressure distributions at a certain distance.

An example has been calculated with KIM to explain the data manipulation process, as shown in Figure 3.7. In the sub-figure (a), the axisymmetric pressure distribution is calculated with KIM, and the dashed line in the field illustrates the plate boundary position, at which the transverse acoustic pressure will be extracted; the transverse pressure distribution at distance $z = 70mm$ is shown in sub-figure (b); this transverse distribution data

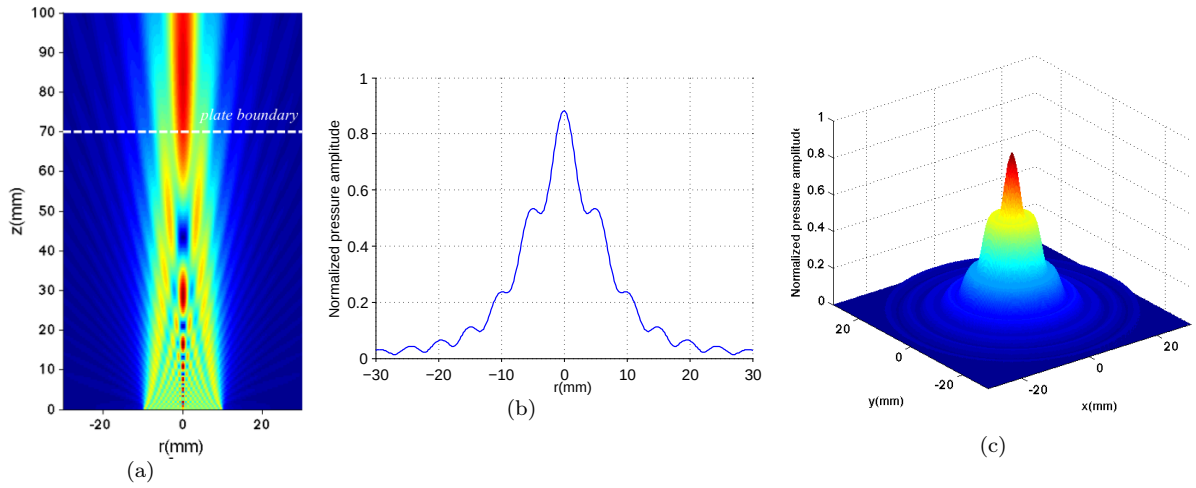

Figure 3.7. Acoustic pressure distribution data manipulation in 3D hybrid model. (a): axisymmetric distribution calculated with KIM; (b): Transverse distribution at distance $z = 70mm$; (c): distribution in Cartesian coordinate with revolution data manipulation.

will be operated with data revolution relative to its axis to generate a 2D surface discrete pressure data in Cartesian coordinate, as in (c). The 2D discrete acoustic pressure data in Figure 3.7(c) will be imported into 3D solid FE model to calculate the displacement field generated by this air-coupled transducer.

In this KIM model the radius of the mono-element transducer is $100mm$. The frequency for the model is $300kHz$. In Figure 3.7, the pressure are normalized for easy manipulating. For the further development of the hybrid model, the pressure amplitude at the far field maximum value is set to $10Pa$, which is a usual ultrasound pressure amplitude in air for ACUT.

3.3.2 3D solid FE model

As a part of the 3D KIM-FEM-RIM hybrid model, the displacement / stress field generated by incident acoustic pressure, which has been calculated with KIM above, will be solved with a full 3D solid FE model. To build the 3D FE model, the 3D Comsol formalism need to be satisfied as what had been presented in Equation 1.10. In 3D case, the coefficients in Comsol formalism are set as the following:

$$c = \begin{bmatrix} c_{11} & c_{12} & c_{13} \\ c_{21} & c_{22} & c_{23} \\ c_{31} & c_{32} & c_{33} \end{bmatrix} \quad a = \begin{bmatrix} -\rho\omega^2 & 0 & 0 \\ 0 & -\rho\omega^2 & 0 \\ 0 & 0 & -\rho\omega^2 \end{bmatrix} \tag{3.10}$$

where ρ is the material density, ω is the angular frequency of the propagation ultrasound. The orthogonal subscript ij are indicated as following: $1 \rightarrow x, 2 \rightarrow y, 3 \rightarrow z$, following the Cartesian coordinate in Figure 3.2. The coefficient components of c are given in details as following:

$$
\begin{aligned}
c_{11} &= \begin{pmatrix} C_{1111} & C_{1121} & C_{1131} \\ C_{1211} & C_{1221} & C_{1231} \\ C_{1311} & C_{1321} & C_{1331} \end{pmatrix} c_{12} = \begin{pmatrix} C_{1112} & C_{1122} & C_{1132} \\ C_{1212} & C_{1222} & C_{1132} \\ C_{1312} & C_{1322} & C_{1332} \end{pmatrix} c_{13} = \begin{pmatrix} C_{1113} & C_{1123} & C_{1133} \\ C_{1213} & C_{1223} & C_{1233} \\ C_{1313} & C_{1323} & C_{1333} \end{pmatrix} \\
c_{21} &= \begin{pmatrix} C_{2111} & C_{2121} & C_{2131} \\ C_{2211} & C_{2221} & C_{2231} \\ C_{2311} & C_{2321} & C_{2331} \end{pmatrix} c_{22} = \begin{pmatrix} C_{2112} & C_{2122} & C_{2132} \\ C_{2212} & C_{2222} & C_{2132} \\ C_{2312} & C_{2322} & C_{2332} \end{pmatrix} c_{23} = \begin{pmatrix} C_{2113} & C_{2123} & C_{2133} \\ C_{2213} & C_{2223} & C_{2233} \\ C_{2313} & C_{2323} & C_{2333} \end{pmatrix} \\
c_{31} &= \begin{pmatrix} C_{3111} & C_{3121} & C_{3131} \\ C_{3211} & C_{3221} & C_{3231} \\ C_{3311} & C_{3321} & C_{3331} \end{pmatrix} c_{32} = \begin{pmatrix} C_{3112} & C_{3122} & C_{3132} \\ C_{3212} & C_{3222} & C_{3232} \\ C_{3312} & C_{3322} & C_{3332} \end{pmatrix} c_{33} = \begin{pmatrix} C_{3113} & C_{3123} & C_{3133} \\ C_{3213} & C_{3223} & C_{3233} \\ C_{3313} & C_{3323} & C_{3333} \end{pmatrix}
\end{aligned} \tag{3.11}
$$

The fourth-order stiffness tensor C_{ijkl} can be written as a second order tensor, following the abbreviation rule [113]:

$$
C_{kl} \Rightarrow \begin{cases} C_k & \text{if } k = l \\ C_{9-(k+l)} & \text{if } k \neq l \end{cases} \tag{3.12}
$$

Using the tensor subscript abbreviation in Equation 3.12, and the symmetry axes of the material, the coefficient matrix c for homogeneous orthotropic material could be reduced to:

$$
\begin{aligned}
c_{11} &= \begin{pmatrix} C_{11} & 0 & 0 \\ 0 & C_{66} & 0 \\ 0 & 0 & C_{55} \end{pmatrix} \quad c_{12} = \begin{pmatrix} 0 & C_{12} & 0 \\ C_{66} & 0 & 0 \\ 0 & 0 & 0 \end{pmatrix} \quad c_{13} = \begin{pmatrix} 0 & 0 & C_{13} \\ 0 & 0 & 0 \\ C_{55} & 0 & 0 \end{pmatrix} \\
c_{21} &= \begin{pmatrix} 0 & C_{66} & 0 \\ C_{21} & 0 & 0 \\ 0 & 0 & 0 \end{pmatrix} \quad c_{22} = \begin{pmatrix} C_{66} & 0 & 0 \\ 0 & C_{22} & 0 \\ 0 & 0 & C_{44} \end{pmatrix} \quad c_{23} = \begin{pmatrix} 0 & 0 & 0 \\ 0 & 0 & C_{23} \\ 0 & C_{44} & 0 \end{pmatrix} \\
c_{31} &= \begin{pmatrix} 0 & 0 & C_{55} \\ 0 & 0 & 0 \\ C_{31} & 0 & 0 \end{pmatrix} \quad c_{32} = \begin{pmatrix} 0 & 0 & 0 \\ 0 & 0 & C_{44} \\ 0 & C_{32} & 0 \end{pmatrix} \quad c_{33} = \begin{pmatrix} C_{55} & 0 & 0 \\ 0 & C_{44} & 0 \\ 0 & 0 & C_{33} \end{pmatrix}
\end{aligned} \tag{3.13}
$$

Noting that for isotropic materials with only two independent stiffness components, the relation between the components is: $C_{11} = C_{22} = C_{33}$, $C_{44} = C_{55} = C_{66}$, $C_{12} = C_{13} = C_{23}$, and $C_{12} = C_{11} - 2C_{66}$. The acoustical velocities in solid c_p(longitudinal wave velocity) and c_s(shear wave velocity) [113] are related with the stiffness modules in isotropic materials by:

$$
c_p = \sqrt{\frac{C_{11}}{\rho}}, \qquad c_s = \sqrt{\frac{C_{66}}{\rho}} \tag{3.14}
$$

Thus, the wave length of longitudinal wave or shear waves in solid would be determined by their velocities with: $\lambda_p = c_p/f$, $\lambda_s = c_s/f$. As the same meshing requirement in 2D situation, the minimum mesh step in FE model should be smaller than $\lambda_{min}/4$ for 2^{nd} order elements (quadratic), in which λ_{min} is the minimum value between the wavelength of longitudinal wave λ_p and shear waves λ_s.

At the front surface of the plate, the acoustic wave in air is incident to the solid plate surface in the plate inspection configuration. For the normal incidence situation, which will be used in Chapter 4, the acoustic pressure reflection R_p and transmission T_p coefficients [113] are:

$$R_p = \frac{z_2 - z_1}{z_2 + z_1}, \qquad T_p = \frac{2z_2}{z_2 + z_1} \tag{3.15}$$

and the particle velocity reflection R_v and transmission T_v coefficients are:

$$R_v = -\frac{z_2 - z_1}{z_2 + z_1}, \qquad T_v = \frac{2z_1}{z_2 + z_1} \tag{3.16}$$

where z_1 is the acoustic characteristic impedance of the medium (air) where incident wave propagates, z_2 is that of the transmission medium (solid). Due to the very large impedance difference between them, *i.e.* $z_2 \gg z_1$, the reflection and transmission coefficients becomes $R_p \approx 1$ and $T_p \approx 2$. At the boundary, the particle velocity of incident wave and reflected wave are in reversed phase, while the acoustic pressures are in the same phase. In this approximative total reflective situation, the resultant velocity at air-solid boundary tends toward 0 while the resultant acoustic pressure tends to twice that of the incident wave, *i.e.* $p_b = 2p_{in}$, where p_b is the pressure at the boundary, p_{in} is the incident acoustic pressure.

In the 3D solid FE model, the boundary condition a the plate front surface is equivalent to that which would exist if the solid plate was placed in vacuum, due to the very large impedance difference between air and solids. So the stress imposed at the front surface of plate is set equal to twice the incident wave pressure.

Hence, the normal stress in the solid, as the counterforce of incident acoustic pressure, can be written as:

$$\overline{\overline{\sigma}}\boldsymbol{n} = -p_b\boldsymbol{n} = -2p_{in}\boldsymbol{n} \tag{3.17}$$

in which $\boldsymbol{n} = (n_1, n_2, n_3)$ is the unit outward direction vector, $\overline{\overline{\sigma}}$ is the stress tensor in solid. Equation 3.17 is similar to Equation 1.29. Noting that the Neumann boundary condition in Equation 1.10, is $\boldsymbol{n} \cdot (c\nabla u) + qu = g$ and that $\overline{\overline{\sigma}} = c\nabla u$, the coefficient q has to be set to 0, and then the term g has to be set equal to the normal stress, *i.e.*

$$\boldsymbol{g} = \begin{pmatrix} g_1 \\ g_2 \\ g_3 \end{pmatrix} = \begin{pmatrix} 0 \\ 0 \\ -2p_{in} \end{pmatrix} \tag{3.18}$$

where the components (g_1, g_2, g_3) give the designated stress value at the solid boundary in different directions. At the back interface of the plate, all the components of $\boldsymbol{g}$ are set to 0 to simulate free stress boundary condition. An oblique acoustic incident situation from air to solid is derived in the 2D version of the hybrid model, which is presented in Appendix B.

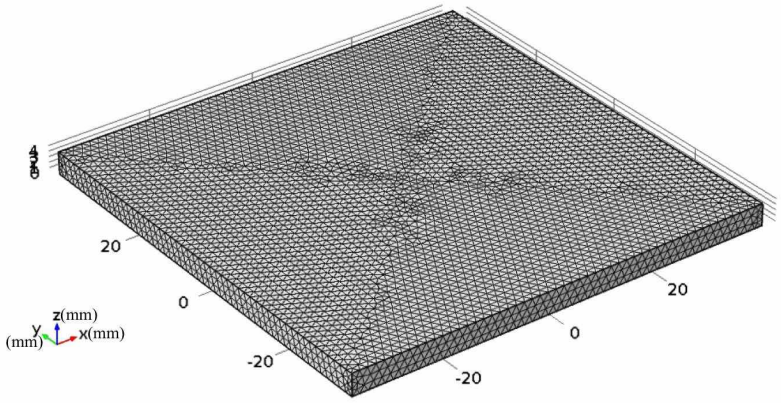

Figure 3.8. Tetrahedral meshing in 3D plate FE model.

As what has been explained in Chapter 1, the absorbing region will adopt the improved VAR to absorb the incident wave at the borders. The stiffness and density of the material setting in Equation 1.32 allows the length of the VAR to be $\approx 1.5\lambda$. This reduction of the AR greatly improves the ability of 3D model and is essential for the 3D solid FE model.

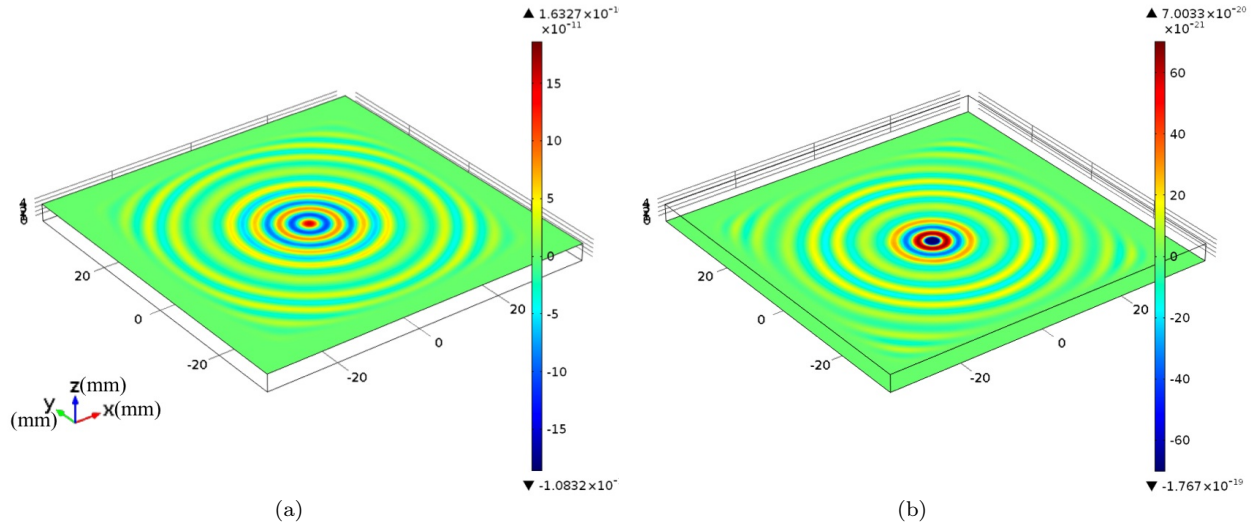

Figure 3.9. Normal displacement of the perspex plate in 3D FE model. (a): front surface; (b): back surface. The colorbar shows the real value of displacement with the unit m.

As an example, the 3D FE solid model is used to simulate a perspex plate with the size of $78mm$ in length and width, $4mm$ in thickness. Its mechanical properties are listed in Table 3.1. In the table, ρ is the material density, E is the Young's modulus, ν is the Poisson's ratio. c_0 is the sound velocity, Z is the acoustic characteristic impedance.

Material	$\rho(g/cm^3)$	E(GPa)	ν	$c_0(mm/\mu s)$	$Z(Rayl)$
Air	1.225×10^{-3}	$(1.44 + 0.0029j) \times 10^{-4}$		0.342	420
Perspex	1.17	$6.0468 + 0.1814j$	0.31	2.695	3.15×10^6

Table 3.1. Acoustic properties of air and perspex

The complex acoustic pressure, which has been calculated with KIM model and then been data manipulated as shown in Figure 3.7(c), is used as the input function at the plate front surface. This acoustic pressure at distance $z = 70mm$ away from the transducer surface, is set to be $10Pa$ as what has been explained above to simulate a realistic wave incident to the perspex plate. The frequency for the 3D FE model is set to be $300kHz$, *i.e.* equal to that of the incident wave. The wave-lengths of the longitudinal wave and shear wave are $\lambda_p = 8.98mm$ and $\lambda_s = 6.09mm$. As the requirement of improved VAR, the length of AR is $1.5\lambda_p = 13.48mm$.

The requirement of meshing for accurate results in FE calculation is at least 4 nodes within a wavelength. Thus free tetrahedral meshing in COMSOL has been used to generate tetrahedral and triangular elements at the boundaries or inside the cuboid plate. By defining the maximum meshing size is $\lambda/4$, the meshing for the plate and the AR could be sufficient to ensure required accuracy. The quadrilateral meshing of the 3D plate is shown in Figure 3.8. The number of elements of the model is 103342 and the number of DOFs is 456612. With the assistance of computing cluster Avakas [90], the computational time using Comsol stationary solver PARDISO is $54s$ under employing 1 node (12 cores per nodes) of the cluster.

The normal displacements u_3 at the front surface (a) and back surface (b) of the perspex plate are shown in Figure 3.9. For through-transmission plate inspection which is the topic of this work, the normal displacement at the plate back surface will be used as the input of the 3D RIM for further prediction of the acoustic pressure at the receiver.

3.3.3 3D RIM model for receiver

In the 3D KIM-FEM-RIM hybrid model as shown in Figure 3.1, the normal displacement of the plate back surface will be extracted for the input of the 3D RIM model. The normal displacement of plate back surface is shown in Figure 3.9(b), as the result of 3D FE model. Since the hard boundary (solid plate) comparing to the air, the velocity and displacement satisfy the following relation for harmonic wave (corresponding to a single frequency in frequency domain):

$$\nu_z = j\omega u_z \tag{3.19}$$

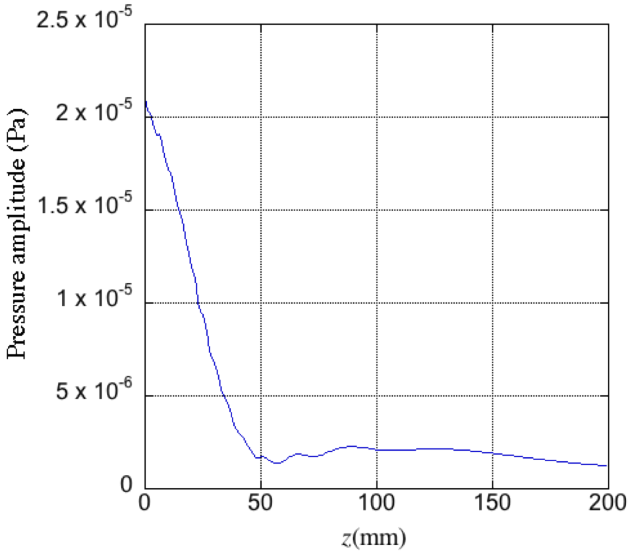

Figure 3.10. Acoustic pressure distribution on-axis at the receiver side from the plate back surface.

where u_z and ν_z are the normal displacement and velocity at the back surface of the plate respectively.

Thus the normal velocity at the back side of the plate can be obtained as the input of 3D model in Equation 3.9. The spatial distribution of the acoustic pressure from the plate to the receiver can be predicted with this expression. The on-axis pressure amplitude distribution is shown in Figure 3.10. For obtaining the response of the receiver, the acoustic pressure must be calculated all over the surface of the receiver and integrated across that surface.

3.4 Summary

In this chapter, the analytical RIM model has been introduced to simulate the acoustic field produced by a non-piston velocity distribution plane surface. The 3D RIM is derived from the Green's function at the acoustic hard boundary condition under Cartesian coordinates. This RIM method is very useful to calculate the acoustic field produced by an acoustic hard plane surface. Its implementation has been validated using the axisymmetric FE model developed in Chapter 1, and applying a non-piston distribution along the radial direction of a disk.

A 3D KIM-FEM-RIM hybrid model has been built based on the KIM model, 3D FE model and 3D RIM model for a through-transmission plate purpose. The acoustic field generated by ACUT or MEACUT with axisymmetric shape can be calculated using KIM model which had been introduced and validated in Chapter 1. The complex acoustic pressure distribution calculated with axisymmetric KIM is then manipulated using coordination conversion to form a surface discrete distribution, which is imported in turn into the 3D solid FE model. With the 3D solid FE model, displacements and stresses inside

the plate are calculated. The acoustic field in air at the receiver side can be calculated by importing the plate back surface velocity into the 3D RIM. Thus acoustic field pressure at a given spatial coordinate can be calculated with RIM. This 3D KIM-FEM-RIM hybrid model will be used to simulate the acoustic scanning of a composite plate for defect inspection, in the next chapter.

Chapter 4

Application of annular array for plate inspection

4.1 Introduction

In the previous chapters, an 8-element annular MEACUT has been designed and fabricated to get an optimized, focused, large frequency band acoustic field. This MEACUT has also been characterized and shown to have a high efficiency, a wide frequency bandwidth and a well-focused acoustic field profile. A 3D KIM-FEM-RIM hybrid model has been developed to simulate the propagation through a plate, including both finite air-coupled transmitter and receiver. The motivation of this chapter is to use the MEACUT system for a NDT application and to run numerical simulations to predict the acoustic phenomena involved in this process. Based on that, this chapter is composed of two parts: the experimental measurement to inspect a damaged composite plate and the comparison with its hybrid model predictions.

In the experiments, a composite plate with an impact damage is inspected in through-transmission mode using one single element ACUT (plane transducer) operating as the receiver and either another similar ACUT or the MEACUT built in Chapter 2, operating as the transmitter. The purpose is to scan the plate sample, and more specifically its damaged region, with both pairs of transducers, to compare together both sets of C-scan data thus obtained and to check/demonstrate that the MEACUT allows the spatial resolution of the inspecting process to be improved. Ideally, two MEACUTs should have been used as transmitter and receiver to decrease as much as possible the size of the focusing spot and so to increase the spatial resolution, though replacing one single ACUT only by a MEACUT (among the pair of ACUT traditionally employed for contact-less, ultrasonic scanning of plate-like samples) should lead to an increase in the spatial resolution. This will be checked experimentally in the following, and numerical predictions will also be made, using the 3D KIM-FEM-RIM hybrid model, to confirm the experimental results. Wave propagation in composite materials is rendered complex by the medium heterogeneity, anisotropy and viscoelasticity. However, in the used model the material is considered

as homogeneous in the low frequency regime of the ACUT or MEACUT. The damaged region is modelled by a local significant decay in the material stiffness. However, as the undamaged zone of the plate, this damaged region is locally supposed to be homogeneous. The only heterogeneity considered in that model comes from the fact that both damaged and undamaged zones have different mechanical properties. The material anisotropy and viscoelasticity are nevertheless taken into account in the whole plate FE model.

4.2 Experiments with annular ACUT/MEACUT

Ultrasonic NDT inspection experiment has been proceeded to validate the efficiency and transverse resolution of annular MEACUT. As a starting point of applying annular MEACUT in NDT, bulk waves in plate are excited using through-transmission plate inspection mode. Following this mode, transducers (ACUT or MEACUT) are placed at each side of the plate, as the transmitter and the receiver are well aligned together in the x, y plane, so that maximum amplitude is detected by the receiver as the transmitter sends the incident acoustic beam. A horizontal scanning axes is set under the plate for a line C-scan along x direction, as the experimental setup schematic shown in Figure 4.1.

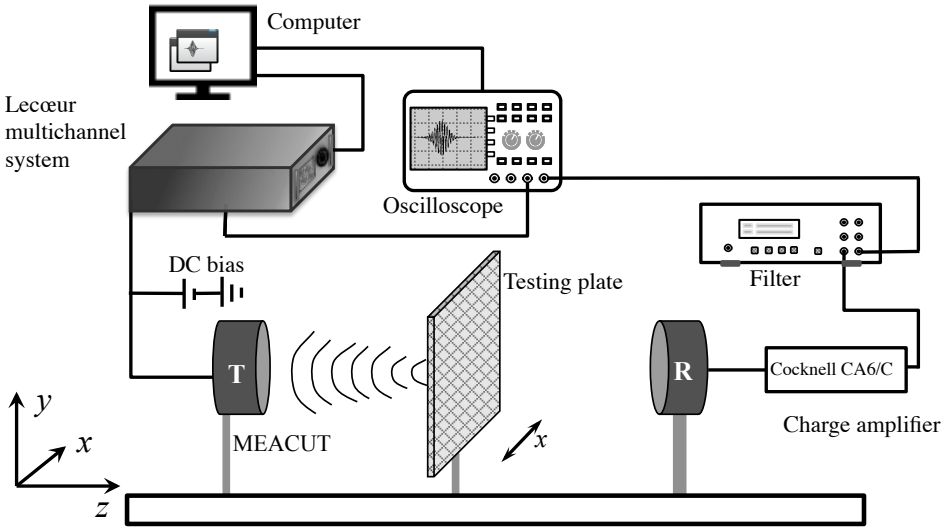

Figure 4.1. Schematic of experimental configuration for through-transmission plate inspection with transmitting annular MEACUT.

The inspected specimen is a glass-polyester reinforced composite plate with $4.5mm$ thickness, $460mm$ length and $325mm$ width. Glass-polyester composite material is generally a laminated structure composed of polymeric matrix and reinforcing glass fibres. This composite plate has an impact damage in its centre area, which is shown in Figure 4.2. It has a circular shape at the side which has been impacted (Figure 4.2(a)), but this becomes elliptical as running through the plate thickness. At the surface opposite to the impact, the damage has an elliptical shape, as shown in Figure 4.2(b). This is due to the strong anisotropy of the material. This damage has then a conical shape due to the shock wave

effect produced by the impact. This glass-polyester sample is quite transparent so making it easy the visual observation of the damage shape. This region seems to contain some micro-cracks across the thickness, as shown in Figure 4.2(b). From these observations, the size of the damage can be measured: semi-major axis (denoted a in figure) of $15mm$ and semi-minor axis (denoted b in figure) of $9mm$ at the back surface of the sample; diameter of damage is $3mm$ at the impact surface. The C-scan of the composite plate will be made across the defect, along its major axis and minor axis. The coordinate direction x is along the ellipse major axis and y is along the minor axis.

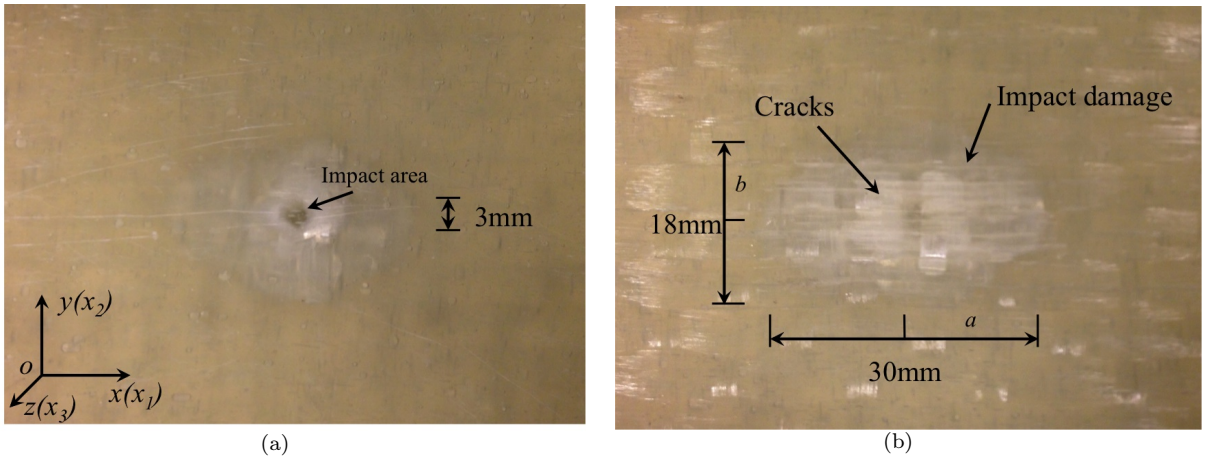

(a) (b)

Figure 4.2. Photography of the impact damage in the glass-polyester composite plate. (a): Impact surface with circle shaped damage; (b): Back surface with elliptical damage.

The excitation signal for transmitter is a Gaussian windowed 20-cycle sinusoidal tone burst. The operating frequency of the signal is tuned to the resonant frequency of the undamaged plate, in which the amplitude of the output signal at the receiver attains its maximum value. At the damaged area, this resonance is broken, causing a significant decreasing of the signal amplitude. Through that, the contrast of the signal amplitude between the damaged area and the undamaged one should be at the maximum level. This resonant frequency is measured to be $310kHz$ for the composite plate.

The output signal from the receiver is sent to the charge amplifier (Cocknell CA6/C) to convert the charge generated by the receiving ACUT to alternative voltage. The output signal from the cocknell is filtered to get better SNR. The final signal output is exported to the oscilloscope and monitored using acquisition software in computer.

4.2.1 Use of two ACUTs

For the comparison of the inspection with MEACUT, the mechanical scanning is firstly implemented using a pair of mono-element air-coupled capacitive transducers (2 ACUTs). The diameter of each transducer is $d = 50mm$ (this is very similar to the diameter of the MEACUT, which will be used further down) and their centre frequency is $f = 250kHz$. As explained in Chapter 2, these capacitive elements have very large

frequency bandwidth so that they can easily be driven between $100kHz$ and $450kHz$ with nice frequency response. The experimental configuration is shown in Figure 4.1, except that the transducers (transmitter and receiver) are two mono-elements and the signal generator is a wave maker rather than Lecœur multichannel system. The photography of this experimental setup is shown in Figure 4.3. In this experiment, the transmitting ACUT and receiving ACUT are placed parallel at opposite sides of the composite plate and at the distance of $50mm$ away from it.

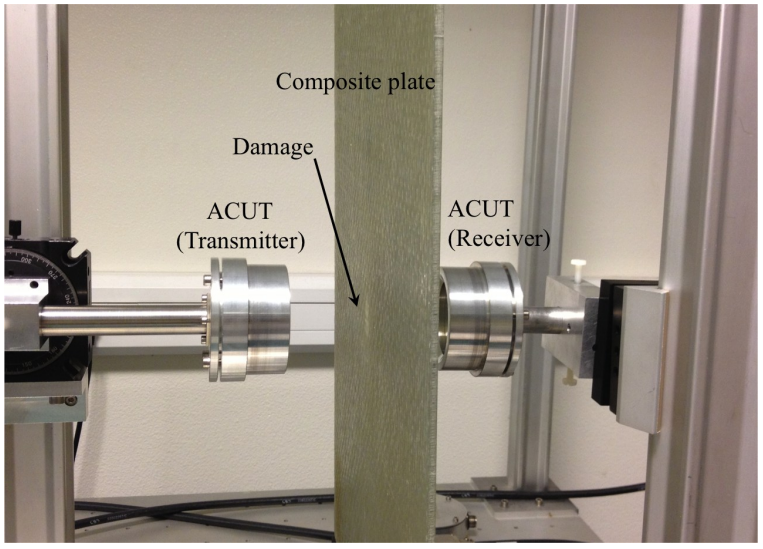

Figure 4.3. Photography of experimental setup: transmitting ACUT, receiving ACUT and composite plate placed between them.

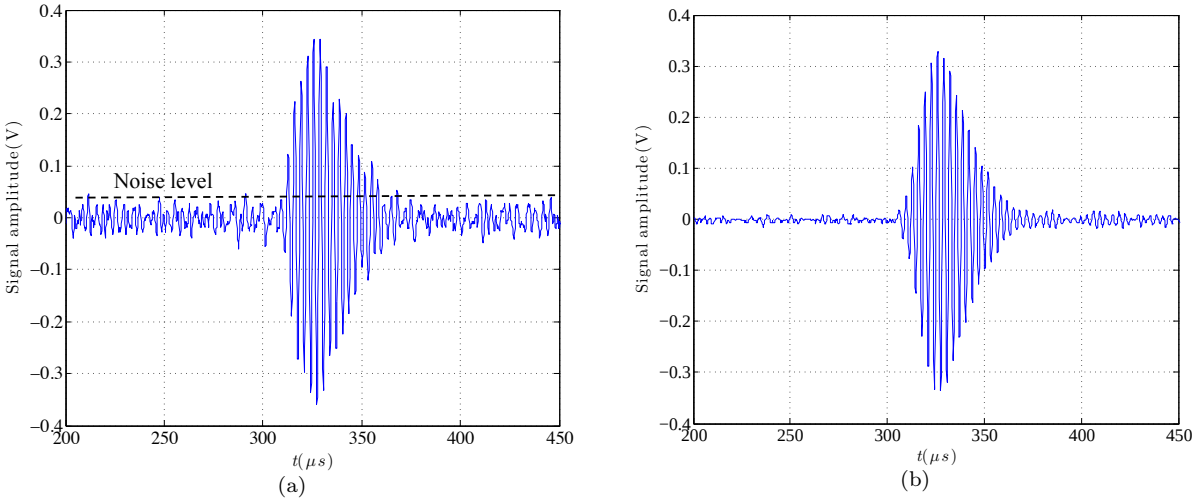

Figure 4.4. Measured temporal signals using transmitting ACUT and receiving ACUT in through-transmission mode: (a) real time and (b) 20-time averaged. Excitation signal is a Gaussian windowed 20-cycle, $310kHz$ tone burst.

The real time signal from the receiving ACUT is shown in Figure 4.4(a), while Figure 4.4(b) shows the 20-time average signal in this setting. The SNR is around $18.6dB$. The signal reveals the transmission throught an undamaged composite plate region.

4.2.2 Use of transmitting MEACUT and receiving ACUT

The multi channel Lecœur system is used as the function generator for driving the 8 channels of the annular MEACUT. In this configuration, as illustrated in Figure 4.1, the transmitter is the 8-element annular MEACUT and the receiver is a mono element transducer with diameter $d = 50mm$. The Lecœur multichannel system is driven using Matlab script. The excitation signal of the MEACUT elements is the same as that used for ACUTs, *i.e.* Gaussian-windowed, 20-cycle, $310kHz$ sinusoidal tone burst. However, each signal sent to an element of the MEACUT is delayed in time so that acoustic beams produced by all elements arrive simultaneously at the same distance equal to that between the MEACUT surface and the plate. In our experiments, this distance between the MEACUT surface and the plate is $50mm$, and the receiving ACUT is still placed at $50mm$ away past the plate.

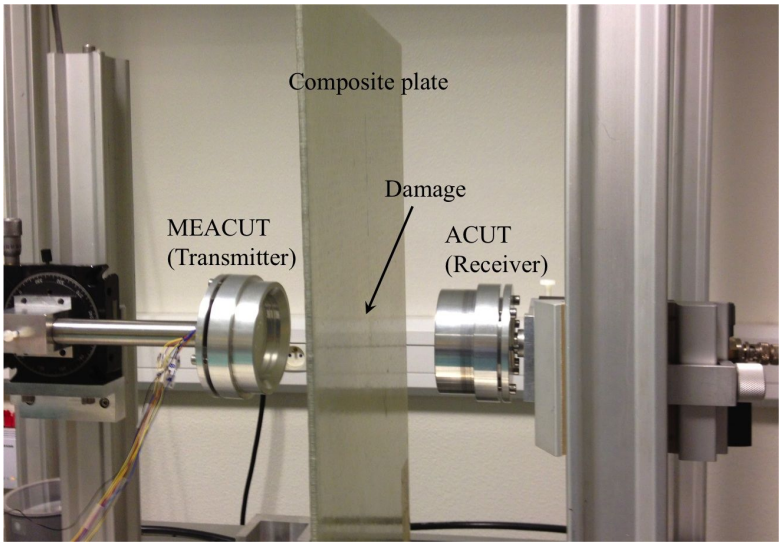

Figure 4.5. Photography of experimental setup: transmitter is 8-element annular MEACUT, receiver is an ACUT.

Output signals from the ACUT receiver (in the configuration shown in Figure 4.5 with transmitting MEACUT and receiving ACUT) have been acquired and shown in Figure 4.6. The real time signal from the receiving ACUT in this setup is shown in Figure 4.6(a), and the 100-time averaged signal is shown in Figure 4.6(b). The SNR of the real time signal is around $13.1dB$. As an example, output signals from the ACUT receiver are shown for the undamaged area Figure 4.7(a) ($30mm$ away from the centre of the impact along minor axes b) and damaged area Figure 4.7(b) ($5mm$ away from the centre of the impact along minor axes b)

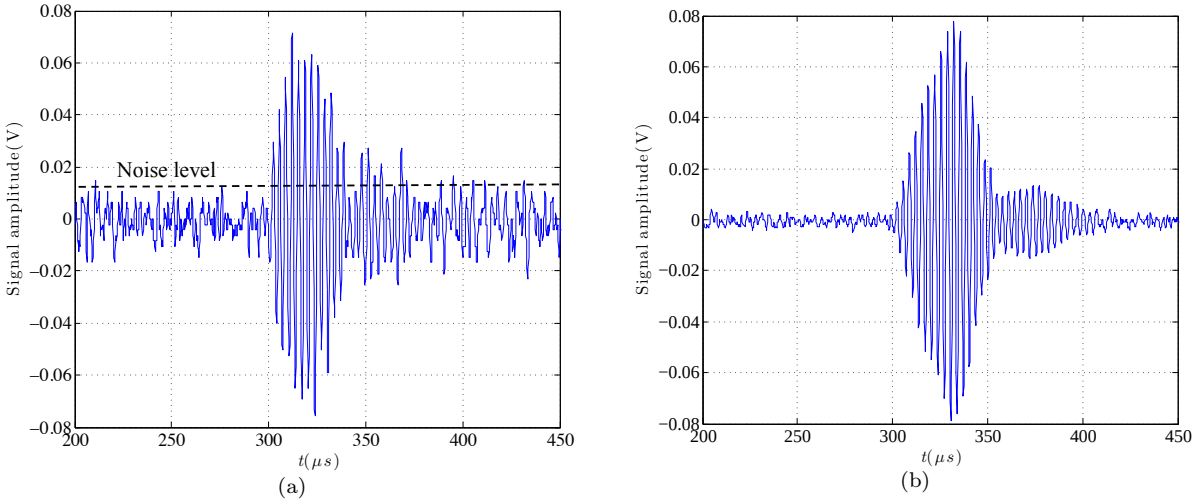

Figure 4.6. Measured temporal signals using transmitting MEACUT and receiving ACUT in through-transmission mode: (a) real time signal and (b) 100-time averaged signal.

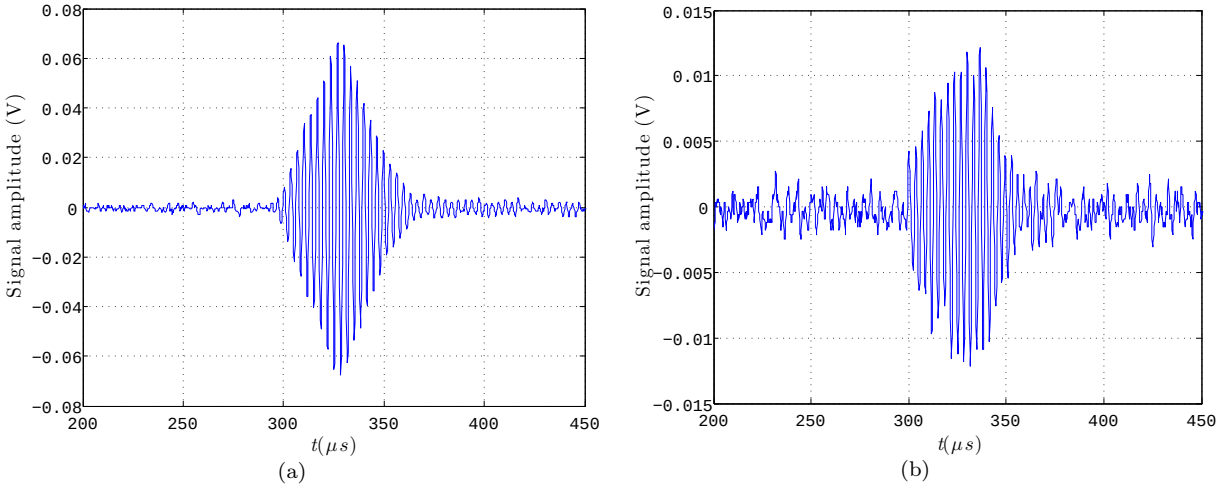

Figure 4.7. Measured signals using transmitting MEACUT and receiving ACUT in through-transmission mode: (a) undamaged and (b) damaged zones of glass-polyester composite. Excitation signal is a Gaussian windowed 20-cycle, $310kHz$ tone burst. Signals are 100 time averaged.

4.3 3D hybrid model for MEACUT composite plate inspection

To use the 3D KIM-FEM-RIM hybrid model for simulating the composite plate inspection system, the 3D FE model should be built for the composite plate, following the procedures developed in Chapter 3. The composite plate material elastic constants have been measured using a standard ultrasonic technique, and are shown in the following Table 4.1. The stiffness moduli are inferred by inversing the plane wave transmission coefficients obtained for different incident angles with the immersed technique described in

[114], and further checked by [79]. The imaginary parts of the stiffness moduli represent the material viscoelasticity, and are approximately set to 2.8% of the real parts of the stiffness moduli. The orthogonal subscript ij are indicated as following: $1 \to x, 2 \to y, 3 \to z$, as shown in Figure 4.8.

Density	$C_{ij} = C'_{ij}(1 + 2.8\%j)$ in (GPa)						
$\rho(g/cm^3)$	C'_{11}	C'_{22}	C'_{33}	C'_{44}	C'_{66}	C'_{12}	C'_{23}
1.8	40.3	14.1	15.9	3.9	3.9	6.32	2.2

Table 4.1. Glass-polyester reinforced composite plate material properties.

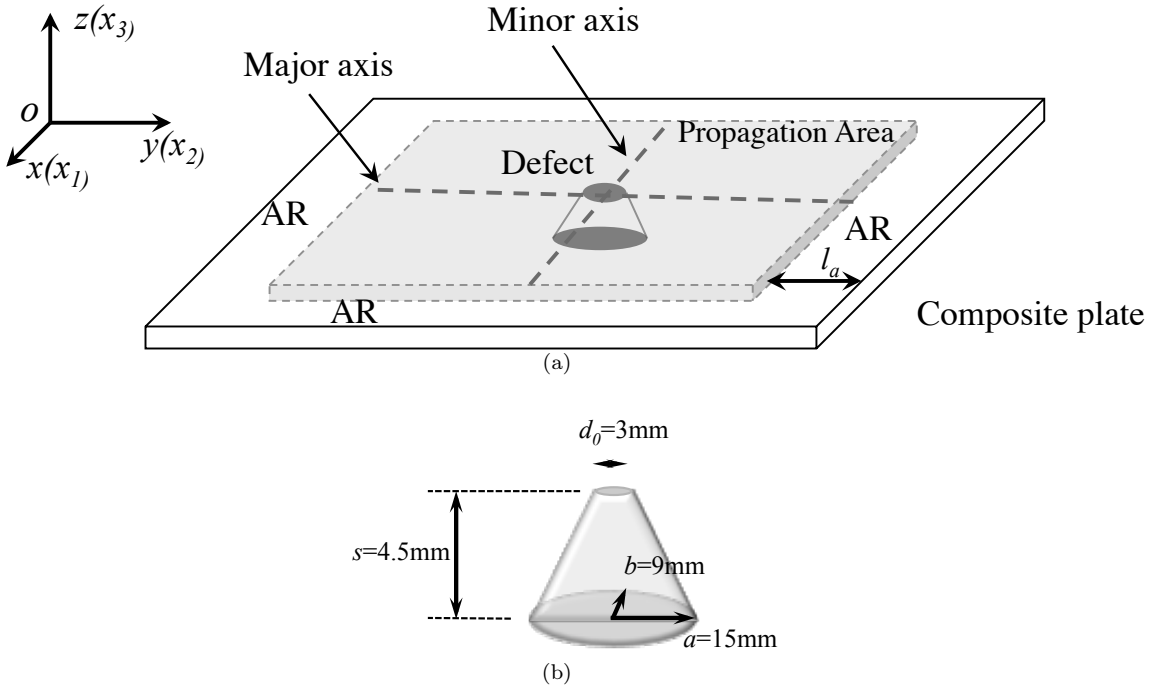

Figure 4.8. Schematic of 3D model for composite plate ultrasonic inspection (a): 3D plate FE model; (b): Geometrical shape of impact damage.

The impact damage is modelled by an elliptical truncated cone: its upper surface is a circle of diameter $d_0 = 3mm$ and bottom surface is an ellipse with its semi-major axis $a = 15mm$ and semi-minor axis $b = 9mm$ as in Figure 4.8. In FE model setting, this elliptical truncated cone is modelled with geometrical functions, which define the volume shown in Figure 4.8(b).

The distribution of delaminations and cracks within the defect happens to be inhomogeneous, while homogeneity assumption of material properties in this damaged area can greatly reduce the calculation time, as well as ensure the prediction accuracy [79]. So in the model, the defect is simulated by locally decreasing the material stiffness through the damaged region, using a space-dependent function according to the observations made on the sample. The stiffness moduli inside the damage are reduced by 80% of their nominal

values given in Table 4.1, *i.e.* $C_{ij}^{Defect} = 20\%C_{ij}$, where C_{ij} is the undamaged material stiffness moduli.

4.3.1 Axisymmetric KIM model for incident acoustic field

The 3D hybrid model for composite plate ultrasonic inspection is schematized in Figure 3.1. As explained in Section 3.3, the analytical KIM model provides the pressure field distribution incident at the front surface of the plate. This is initially calculated in axisymmetric conditions (cylindrical coordinate) and converted into 3D Cartesian coordinates, before it can be used as input data in the FE model. In the experiments, the distance between the transmitting MEACUT and the plate is set equal to $50mm$, and of course the excitations applied to each element of that MEACUT are phase-shifted so that the incident acoustic beam focuses $50mm$ away from its active surface. This is also the case in the KIM model, and the resulting pressure distribution thus predicted at the insonified surface of the plate is shown in Figure 4.9.

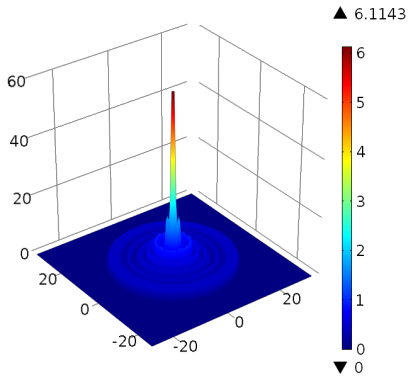

Figure 4.9. Ultrasonic pressure amplitude calculated by KIM model.

4.3.2 3D FE model for composite plate inspection

The 3D FE model to simulate the displacement / stress field of the composite plate is built following the similar method in Chapter 3. The dimensions of the model are $111mm$ in length and width, $4.5mm$ in thickness. The frequency is $310kHz$, which is the same as the resonant frequency of the plate. As the requirement of improved VAR, the length of AR is set to be $1.5\lambda_{max} = 23.6mm$. The mapped meshing is used to generate the hexahedral and quadrilateral elements in the solid, as shown in Figure 4.10. The 3D FE model contains 73205 elements.

The FE model is then solved (in the frequency domain) so that the dynamic response of the plate to the incident pressure beam applied at the front surface of the plate is calculated. As explained before, the anisotropy and viscoelasticity of the material are taken into account in that model, as well as the presence of the damaged zone. The 3D PDE formalism and boundary conditions are set properly following Equation 3.10−Equation 3.13.

The scanning of the MEACUT in the 3D FE model along the direction parallel to the plate surface *xoy* through implementing the ultrasonic pressure shown in Figure 4.9 at different positions at the plate front surface. Thus this scanning is realised with a position dependent parametric solver in 3D plate FE model. The solver in Comsol is PARDISO [78], with a parametric sweeping with 27 positions. The number of DOFs is 1948617. The calculation of this 3D FE model takes $1315s$ for the scanning along one axis (major or minor axis of the elliptical damage) with the computing cluster Avakas with 1 node (12 cores in a node).

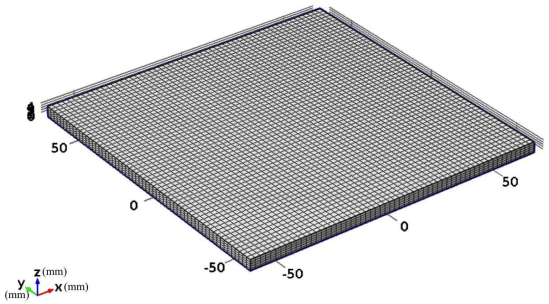

Figure 4.10. Quadrilateral meshing of the composite plate in 3D FE model.

The simulated displacements at this front surface (shown in Figure 4.11(a)) and also at the back surface of the plate (shown in Figure 4.11(b)-(d)) demonstrate the beam scattering through the plate. The anisotropy of the plate causes strong ultrasonic dispersion in solid along different directions. The back surface displacements demonstrate the scattering field by the damage at different positions. Lamb waves [115] seem also to be excited in the plate and away from the damage.

4.3.3 3D RIM model for receiver and comparison with experimental results

In the through-transmission plate inspection 3D FE model, the input is the pressure distribution data generated by the transmitter (ACUT or MEACUT) at the front surface of the plate, while the output is the normal displacement at the back surface. The displacement at the back surface provides the information for the post processing to predict the scattering field at the receiver side of air domain. 3D RIM model is applied by using the normal displacement of the plate as input data in Equation 3.9, since for a harmonic wave the normal velocity of the plate is related to its displacement by $\nu_z = j\omega u_z$, where u_z and ν_z are the normal displacement and velocity at the back surface of the plate respectively.

The pressure field behind the plate at the receiver air domain side may come from two parts: (1) directive energy transmitted through the plate and (2) radiation of guided waves propagating along the plate and away from the damage. The major percentage

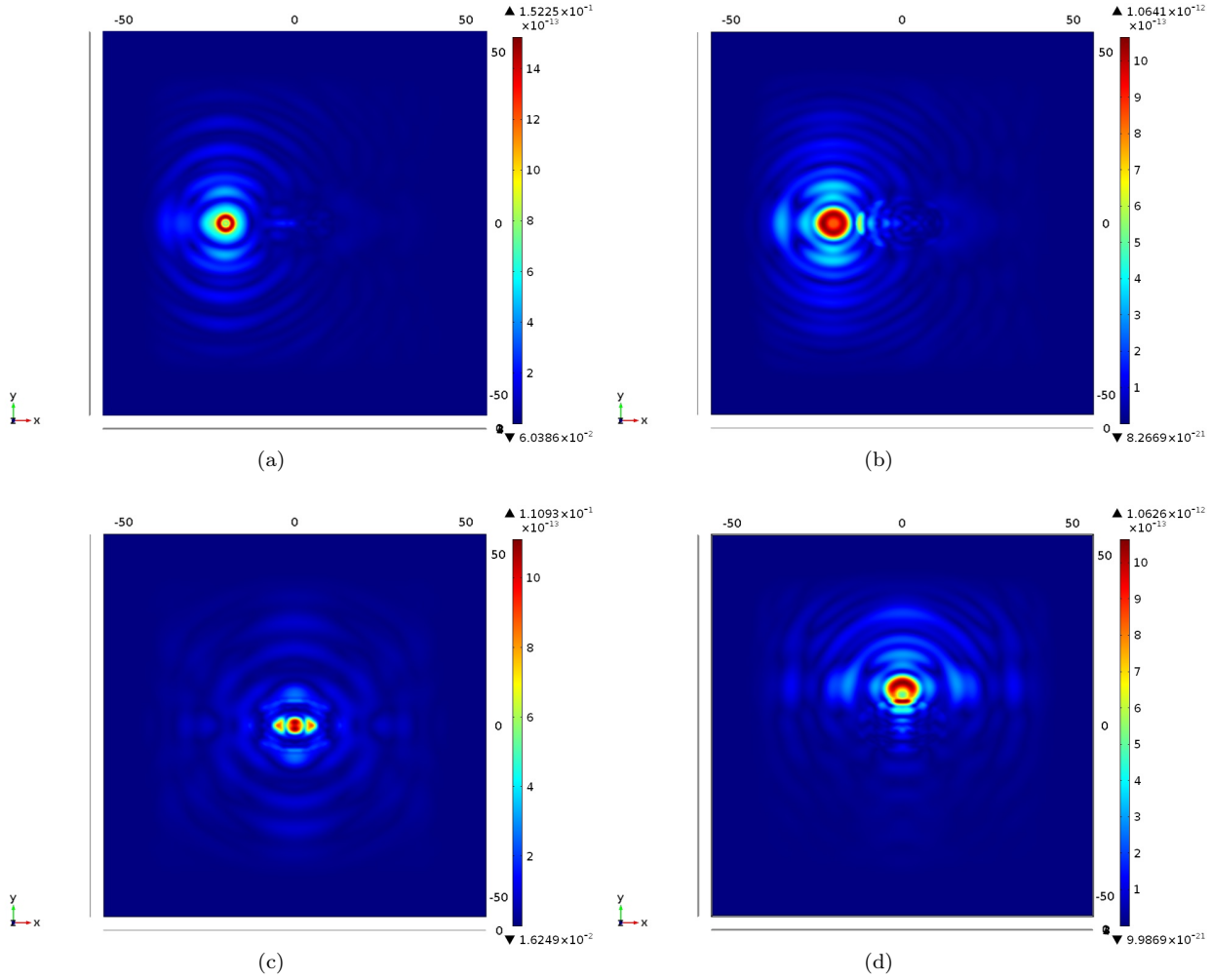

Figure 4.11. Normal displacements at the front and back surfaces of the composite plate with through-transmission plate inspection model. (a): Insonified front surface; when incident beam hits the plate at (b) $x = -20mm$ and $y = 0mm$; (c): centre point of plate; (d): $x = 0mm$ and $y = 10mm$.

of the energy transmitted past the plate is likely to be due to direct transmission. The second part is due to Lamb waves leakage into air during the propagation along the back surface of the inspected plate. The leakage of Lamb waves also includes energy scattered by the damage as shown in Figure 4.11.

The normal displacement is monitored at the back surface of that simulated plate, in the field of view of a receiving transducer (ACUT or MEACUT), which is supposed to be placed past the plate in the air. This monitored velocity is then used in turn as input data to the Rayleigh integral (RIM model) as explained in Chapter 3. This allows the pressure field to be calculated at any position in the air, and more specifically at the surface of the receiving transducer. If this later is a MEACUT, then the field is calculated at positions on the active surface of its elements (circular or annular), properly phase-shifted so that suitable focusing of that MEACUT is modelled, and all delayed responses

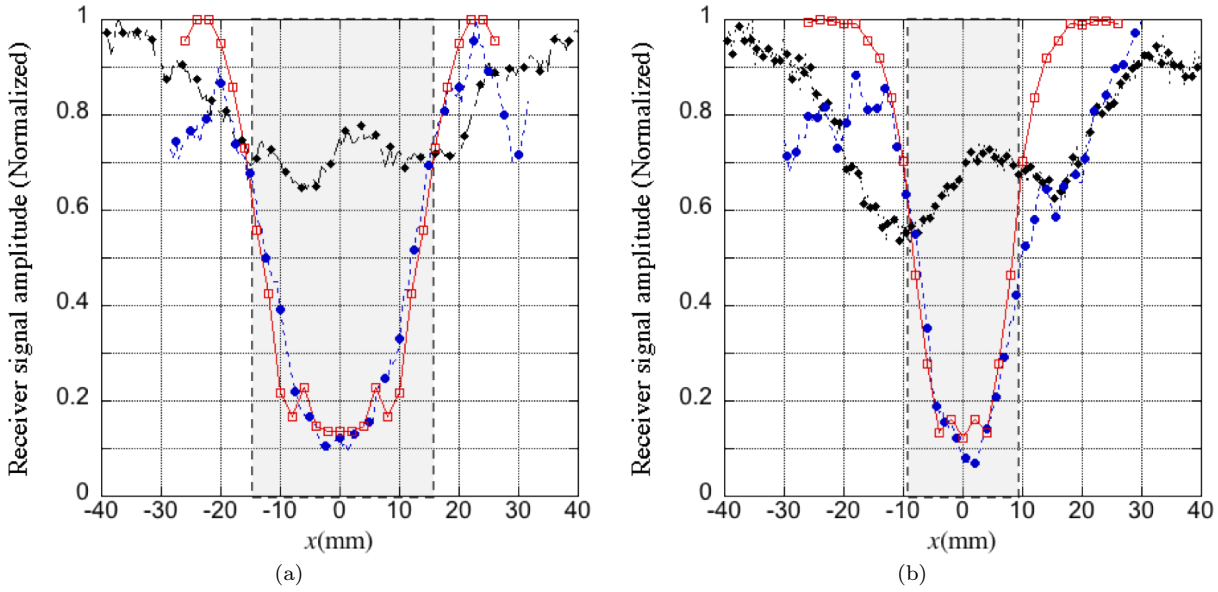

Figure 4.12. Comparison between through-transmission C-scans of the composite plate damaged zone: experimental measurement with a pair of ACUT (dashed diamond −♦−); measurement with MEACUT transmitter/ ACUT receiver (dashed − • −), simulation with 3D KIM-FEM-RIM hybrid model used for one MEACUT and one ACUT (−□). The C-scan is across the defect along its major axis (a) and minor axis (b). The signal output amplitudes from the receiver are normalized for a clear comparison.

of these elements are finally summed up together to establish the acoustic response of the MEACUT.

Signal output from receiver behind the plate at certain distance is related to the pressure received at the surface of the receiver. The receiver acoustic aperture, which controls the transverse extension of acoustic field into the receiver, is directly related to the transverse resolution of the inspection system. The final signal is proportional to the integration of the pressure across the acoustic aperture of the receiver. For a receiving ACUT, the integration is proceeded across its surface using a weighting aperture function.

The comparisons of the experimental results with a pair of ACUT as transmitter/receiver, MEACUT transmitter/ ACUT receiver, and simulation with 3D KIM-FEM-RIM model are shown in Figure 4.12, with the C-scanning along major axis (Figure 4.12(a)) and minor axis (Figure 4.12(b)) of the defect. The 3D KIM-FEM-RIM hybrid model simulates the transmitting 8-element MEACUT/receiving ACUT plate inspection process. The experimental results are in good agreement with the 3D hybrid model predictions for the MEACUT/ACUT inspection, especially with the U-shaped part of the signal along scanning axis, which reveals the presence of the damage. Visually the damaged area is $30mm$ long and $18mm$ wide (Figure 4.2(b)). In the C-scan "image" measured with a pair of ultrasonic ACUT, the acoustic dimensions are around $80mm \times 60mm$; while in that with transmitting MEACUT/ receiving ACUT, its dimensions are around $40mm \times 26mm$,

so much closer to the visual damage, thus indicating that the use of the MEACUT significantly improves the spatial resolution.

The good agreement obtained between the simulation and experimental measurement results is a complementary validation of the whole 3D KIM-FEM-RIM hybrid model. Some differences between the measured and simulated results out of the defect range may be caused by other small invisible defects or stress concentration area resulting from the shock impact on the plate. The width of the U-shaped curve, which indicates the presence of the damage, is larger than the visual width of the damage observed on the composite plate. As written before, this demonstrates that the use of one MEACUT improves the spatial resolution of the C-scan system. When comparing these numerical data with the size of the visually observed damage, *i.e.* with $30mm$ by $18mm$, it appears that the size of the measured U-shaped curve is quite close to the addition of the size of the damage and that of the incident acoustic beam on the surface of the plate. This latter is close to $50mm$ when using two ACUTs and close to $3mm$ when using one MEACUT (as the transmitter) and one ACUT (as the receiver). This phenomenon was already observed in other studies [49] and is well confirmed here. This tends to mean that using an ACUT or a MEACUT as the receiving transducer has no importance as long as one MEACUT is used for the transmitter. However, this is likely to be not totally true since the simultaneous use of two MEACUTs (one transmitter and one receiver) might improve a little bit the spatial resolution in comparison to using only one MEACUT (and one ACUT).

4.4 Summary

In this chapter, the 8-element annular MEACUT has been used for NDT usage both in numerical simulation and experiments. Experiment is proceeded either for demonstrating the use of MEACUT in ultrasonic NDT practice and for the validation of the 3D KIM-FEM-RIM hybrid model. The MEACUT is used in experiment firstly to implement the the through-transmission plate inspection. The inspected specimen is a glass-polyester reinforced composite plate with an impact damage in its centre area having an elliptical and conical shape due to the shock wave effect produced by the impact and due to the material anisotropy.

The C-scanning of the composite is along the major axis and minor axis of the damage. A pair of mono element air-coupled capacitive transducers is also used in the scanning for showing the improvement obtained in the spatial resolution when using one MEACUT instead of one ACUT. In the through-transmission ultrasonic inspection, signal frequency is essential to get a good signal to noise ratio output. The tone burst signal frequency is set to the resonant frequency of the plate to get the maximum output signal. In the damaged area, this resonance within the thickness of the composite plate is destructed because of its reduced stiffness caused by the impact. Thus the scanning gives good contrast between the damaged and undamaged regions of the plate.

The outputs of the scanning along major axis and minor axis predicted by 3D KIM-FEM-RIM hybrid model agree well with the experimental results. This agreement between measured and predicted scattered field indicates that the hybrid model might be used for simulating other NDT applications or other material plates to be scanned, *e.g.* for predicting the smallest size of damage that could be detected using a pair of MEACUT, or for designing new MEACUT with different frequencies to optimize the inspection of various types of defect, *etc.*

Conclusions and Perspectives

Conclusions

The objective of this study was the development of an air-coupled ultrasonic transducer with a wide frequency bandwidth, a high efficiency and that could easily be focused. Such characteristics should allow its use in a broad context of Non-Destructive Testing. To achieve this purpose, a capacitive multi-element probe has been designed, fabricated and characterized; this is denoted as MEACUT for Multi-Element Air-coupled Capacitive Ultrasonic Transducer. It consists in a set of concentric annular elements with a disk in the centre.

A model based on the Kirchhoff integral (KIM for Kirchhoff Integral Model) has been used to predict the acoustic pressure field generated by a disk in the air, from the velocity potential at the surface of the disk. By using the axial symmetry of usual transducers (single or multi elements, denoted ACUT or MEACUT, respectively), a sample Kirchhoff integral (reduction of the traditional double Kirchhoff integral) was used and solved in cylindrical coordinate. In this model, the absorption of ultrasound in air was taken into account using a complex wavenumber, the imaginary part of which is the absorption coefficient of air. Traditionally used to calculate the acoustic pressure field radiated by a single circular transducer, KIM was used here to predict the pressure field radiated by a source consisting of a set of concentric rings with a central disk in the centre. This pressure field was calculated using the acoustic field superposition principle. This method allowed the field radiated by one ring to be obtained by subtracting together both pressure fields radiated by two concentric disks. Thus, the acoustic pressure produced by a multi-element similar to the desired transducer could be simulated. Specific phase delay has then been applied to each element in order to demonstrate the possibility of a dynamic focusing (*i.e.* a variable focusing distance according to the phase delay settings). To validate the acoustic pressure predicted by the KIM method, an axisymmetric finite element model has been set, firstly simulating the field radiated by a circular piston. Very good agreement has been obtained between axial and lateral acoustic pressure distributions predicted by both models (KIM and FEM). The superposition principle and its application to predict acoustic fields generated by one or more rings have also been validated, thus demonstrating the potential of the KIM method for fast (about 1.5 to 15 times faster than the FEM method, depending on the type of source, which is to be modelled) and

accurate simulations of acoustic fields produced in air by a MEACUT, even for large distances of propagation. Thereafter, further validation *via* experimental measurements has been performed.

Usually, acoustic fields generated by multi-element probes may include grating side lobes of non-negligible amplitude, which can induce undesirable artefacts in the ultrasonic measurements and indicate the presence of defects, which are actually absent from the test piece. Such grating lobes can be avoided when the distance between elements is less than half the emitted wavelength. However, the laboratory manufacturing technique used for the MEACUT does not enable such sub-wavelength dimensions to be easily reached because ultrasounds in air have wavelengths of about one millimetre, at the frequencies of investigation ($\approx$ few $100kHz$). Once validated, the KIM method becomes a useful tool for optimizing the geometrical characteristics of the MEACUT so that the resulting probe has dimensions and number of elements, which are compatible with industrial applications, produces a well focused acoustic beam with a small-size focal spot, high amplitude and very little grating lobes amplitude. Thus, the KIM model has been used to optimize the transducer characteristics, the number of elements of the transducer, their size and spacing.

Afterwards, a MEACUT prototype has been built and characterized using a specific ultrasonic rig. The experimental set-up used a laser velocimeter the probe beam of which is reflected by a thin polymer membrane ($5\mu m$ thick), which was placed in the acoustic field, *i.e.* between the transducer to be tested and the laser probe. The frequency response of the prototype MEACUT was measured and showed a very wide frequency bandwidth ($\approx 150\%$ down to $-20dB$). By properly setting the time delays for the excitation signals applied to each element of the MEACUT, this was checked to produce a well-focused acoustic beam. Moreover, this focusing feature (focusing distance, extent,...) was shown to be variable according to the used phased delays (dynamic focusing feature). Besides, the axial and radial distributions of the acoustic field were also measured, and revealed very low amplitude for the unwanted side lobes compared to the amplitude of the desired central lobe. Finally, the measured pressure distributions have successfully been compared to the KIM numerical predictions. The obtained good agreements confirmed the initial validation made by the FEM method, and also demonstrated that the MEACUT prototype was properly made, and that its performances were as expected.

In the purpose of fully numerically simulate an NDT experiment, which would include air-coupled ultrasonic transducers, a hybrid model has been developed and used. This involved two integral methods for the calculation of acoustic fields in air (the above-mentioned KIM method to predict the field between the transmitter and the plate, and a more general integral approach to simulate the field between the plate and the receiving transducer), and the finite element method to simulate the propagation through a damaged plate. The continuity conditions of normal velocity and of pressure in air with stresses at the plate surface have been applied to connect the three steps of calculations. Both

integral methods implemented in this model significantly reduced the required computer resources, as well as the computation time, if comparing with the use of a fully numerical method, *e.g.* based on finite elements or finite differences, only. In this hybrid model, the FEM part built to simulate the ultrasound propagation through a plate used the commercially-available *Comsol Multiphysics* software. This allows equations of dynamic equilibrium and specific boundary conditions to be implemented in a very general formalism based on partial differential equations (PDE). With that tool, the plate was modelled as an anisotropic, viscoelastic, homogeneous medium placed in vacuum (as a good assumption of air regarding the extremely small acoustic impedance of air in comparison to that of any solid material). Complex elastic moduli have then been used as input data, and PDE equations have been solved in the frequency domain (at a single frequency, but all in three dimensions). Absorbing regions have been implemented in the FEM model to eliminate unwanted reflections from the edges, thus modelling this plate as infinitely large. The acoustic field produced by a transducer and calculated by the KIM method in cylindrical coordinates, as explained before, was then expressed in three-dimensional Cartesian coordinates and used as input data to the 3D FEM for defining specific boundary conditions representing an incident acoustic excitation. This approach allows the emitting transducer to be either a single element (ACUT) or a multi-element (MEACUT) source. Solving the PDE model in Comsol provides with displacements, strains and stresses at any point in/on the plate. Therefore, normal displacements can be monitored at the rear surface of the plate, in the field of view of a receiving transducer that would be placed in the air, and aligned with the transmitting transducer. From these normal-displacement components, the associated particle velocity distribution has been used as input data to a second integral model, known as the Rayleigh Integral Model (RIM). This served to calculate the pressure field radiated into the air by the vibrating rear-surface of the plate. This three-dimensional model (3D RIM) has first been validated using an axisymmetric FEM model. The existence of an arbitrary distribution of the normal velocity at the rear surface of the plate was shown to lead to very good agreement between both 3D RIM and FEM models. Consequently, as much faster than the FEM, the 3D RIM was used to simulate the acoustic field detected by a receiving MEACUT, applying adequate delay laws, in the frequency domain, for defining the (dynamic) focusing feature of that receiver.

Based on the work described above, the three dimensional hybrid model was set by combining both KIM and RIM integral methods and the FEM method, thus being called 3D KIM-FEM-RIM hybrid model. This model can fully simulate NDT experiments and was used here to simulate an ultrasonic C-scan experiment. This was employing two transducers: a transmitter and a receiver, which are placed on each side of the plate to inspect. It consists in measuring the amplitude of the signal transmitted through the plate for different positions of the transmitter-receiver. The presence of a defect in the plate usually results in a drop in the amplitude of the transmitted signal. This technique was then used to detect an impact damage in a Glass-Polyester composite plate, and the

experimental C-scan was fully simulated using the 3D KIM-FEM-RIM model. Firstly, both transducers were mono-elements (2 ACUTs) and then the ACUT transmitter was replaced by the prototype MEACUT. The purpose was to demonstrate the improvement in the spatial resolution provided by the use of the MEACUT. The impact damage had apparent dimensions equal to about $30mm$ by $18mm$. The resulting C-scan process led to images of that defect with sizes equal to $80mm$ by $60mm$ when both ACUTs were used, and to $40mm$ by $26mm$ when the MEACUT was used, thus clearly demonstrating the efficiency of that MEACUT, as well as its positive effect on the spatial resolution. These experimental results have been confirmed by the numerical predictions obtained with the 3D KIM-FEM-RIM hybrid model.

The original target of the thesis has then been achieved, *i.e.* setting of an efficient 3D model, running of numerical simulations for the optimization of a Multi-Element Air-coupled Capacitive Ultrasonic Transducer (MEACUT), fabrication and characterization of the prototype MEACUT, checking its wide frequency bandwidth and efficient dynamic focusing feature. Then the fabricated MEACUT was successfully used for improving the performances of an existing, ultrasonic, air-coupled, NDT technique.

Perspectives

On account of the thesis work on MEACUT both in numerical simulation and experiments, several improvements could be implemented in the further works.

The simulation model, which is based on analytical integration methods and FE method, is a completed and self-consistent numerical model for ultrasonic NDT application on plate inspection. At present, the simulation and application of plate inspection is based on through-transmission inspection mode. The 3D KIM-FEM-RIM hybrid model directly connects the displacement (or velocity) from the solid to the acoustic field pressure in air. Thus the field radiated from the back surface of the plate could be regarded as the radiation of the plate vibration. The single side inspection situation should also work using this hybrid model. Therefore, the air-coupled inspection mode at the same side of the plate could be implemented through development of the similar analytical and FE hybrid model.

Based on the perspective to extend the use of MEACUTs to other applications, for instance to single-side plate inspection mode, an experiment using Lamb waves could be made using two focused MEACUT, one as the transmitter and the other as the receiver. Various Lamb modes could be excited within a wide frequency range determined by the large frequency bandwidth of the capacitive transducer. But a pure Lamb mode could also be excited using the plane-wave feature at the focal spot of the MEACUT. The local incident plane wave would excite a certain Lamb mode, depending on its incident angle to the plate, and similarly using a receiving MEACUT for detecting this Lamb mode. The interest would be the inspection of very small zones using a contact-less (air-coupled),

single-sided (both MEACUT at the same side of the tested sample) system. However, this would work as long as the size of the focused spots is larger than the intended Lamb mode wavelength, meaning that all material samples could not be locally inspected in this way and/or that specific MEACUT should be designed and built for such purpose.

In the achieved thesis work, the manufacture technique used for the building of air-coupled capacitive transducer is mechanical machining of metallic pieces. Therefore the dimensional size of the elements cannot be at sub-millimeter scale. As the interference principle of wave field, the pitch of an array should be smaller than half wavelength in medium, *i.e.* millimetre or sub millimetre scale. That request might greatly reduce the radiation acoustic energy from the capacity transmitter and the sensitivity of the receiver. Meanwhile, the manufacturing process would be a challenge to the currently used technique. The development of air-coupled capacitive transducer in NDT application could be combined with the front edge manufacture technique using cMUT. To use micro machining mechanical manufacture process, small metallic elements could be machined and roughened of the metallic surface using photoetching or chemical corruption to embedded groove.

In the perspective of further applications of MEACUT, the focused phased array could be used for local flaw inspection or NDT imaging. This built MEACUT has been shown to have a small focal area with quite high level of pressure, thus being efficient for high-resolution imaging when scanning a damaged zone of a composite plate. It would be now interesting to confirm this efficiency for various types of materials, *e.g.* carbon-epoxy samples, metals, polymers,... and also to check the limit in the smallest detectable defect. The dynamic focusing feature could also be investigated to check whether the depth of the inspected zone of thick samples could be easily and rapidly changed by simply adjusting the phase delays applied to the elements of the MEACUT. This would allow, for instance, the scanning of one skin of a tri-layered sample, then of its core and then of the second skin, and find applications for quickly inspecting sandwich-like structures, which are widely used in industries of transport. The built MEACUT could also be used for applications in the field of material characterization, *e.g.* for locally measuring the mechanical moduli of various materials. This could be useful for checking if mechanical degradation has locally happened in the vicinity of an impacted zone.

With the previous improved technology, other form of air-coupled ultrasonic arrays could be built, such as 1D linear array or 2D matrix. These kinds of array could realize the focused acoustic beam or plane wave front with electronically controlled phased delays. Using the focused phased array mode, large pressure field could be obtained at the focal distance, while using the beam steering mode would fasten scanning process by avoiding mechanical control. Therefore the application of these capacitive arrays would greatly widen the applications of air-coupled capacitive transducers in NDT, and make the inspection faster and easier to implement.

Appendix A

Annular Integration method for calculating the acoustic field produced by axisymmetric transducers

Similar to the subtraction method from inner circular pressure to the outer circular one, the pressure field $p(r, z; \omega)$ of a circular transducer with radius $r = a$ can be considered as the summation of N concentric annuli [116]. The ith annulus has an inner radius σ_{i-1} and outer radius σ_i. As the axisymmetric coordinate shows in Figure A.1.

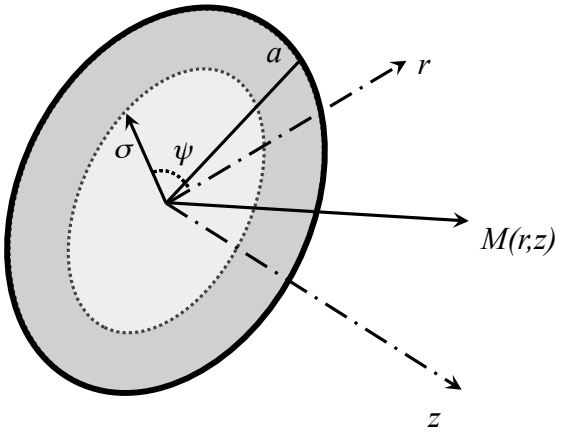

Figure A.1. Axisymmetric coordinate used in the annular superposition method, a piston of radius a is excited by a radially varying particle velocity specified by an aperture function $q(\sigma)$, where σ is the radial postition on the circular piston. The observation point $M(r, z)$ is related to the field superposition of the contribution from N annulus.

The pressure field produced by the ith annuli could be defined as $p_i = p_{\Delta\sigma_i}(r, z; \omega)$. In the annular superposition model, a radially varying particle velocity is considered to take into account the varying contribution from respective annuli to the general acoustic field as the suggestion from [92]. This contribution is specified by defining an aperture function with regard to radius, *i.e.* $q_i = q(\Delta\sigma_i)$ is the aperture function for the ith annuli.

Therefore the total field pressure radiated by a circular disc could be written in the form as:

$$P(r,z;\omega) \approx \sum_{i=1}^{N-1} p_i(q_i - q_{i+1}) + p_N q_N \tag{A.1}$$

Considering a series of uniform spacing of annuli with $\Delta\sigma = a/N$. The aperture function disappears on the boundary, so $q_N = 0$. Equation A.1 could be written as a Riemann summation:

$$P(r,z;\omega) \approx \sum_{i=1}^{N-1} -p_i \frac{q_{i+1} - q_i}{\Delta\sigma}\Delta\sigma \tag{A.2}$$

Apparently, the finer $\Delta\sigma$ is divided, the more accurate the pressure value could be estimated. When $N \to \infty$ and $\Delta\sigma \to 0$, the summation of the acoustic pressure produced by a circular transmitter becomes an integral and the differential quotient becomes a derivative, giving:

$$P(r,z;\omega) = -\int_0^a p_\sigma(r,z;\omega) q'(\sigma) d\sigma \tag{A.3}$$

where $q'(\sigma) = dq/d\sigma$ is the aperture gradient function along radial direction. In Equation A.3, the integration limit for a circular transmitter is from 0 to a. Apparently for an annuli transducer with the inner radius b and the outer radius a, as in the schematic in Figure 1.2, the integration limit should be from b to a in Equation A.3. Since variable σ is a varying radially position for a circular or annular object, the radial integrand variable should be σ for $p_\sigma(r,z;\omega)$ in Equation 1.1. Inserting the circular piston pressure expression to Equation A.3 and replacing the radius a to σ, the apodized pressure field could be deduced as following:

$$\begin{aligned} P(r,z;\omega) = &-\frac{\rho c_0 \nu}{\pi} \int_b^a q'(\sigma)\sigma \int_0^\pi \frac{r cos\psi - \sigma}{r^2 + \sigma^2 - 2\sigma r cos\psi} \\ &\times (e^{-j\omega\sqrt{r^2+\sigma^2-2\sigma r cos\psi + z^2}/c_0} - e^{-j\omega z/c_0}) d\psi d\sigma \end{aligned} \tag{A.4}$$

The double integral expression of Equation A.4 should be derived for the aperture function $q'(\sigma)$. For the easily coding and computing time consideration, a uniform piston apodization function is used in our cases. Since either for air-coupled capacitive circular or for annular transducer, the piston acoustic emission model is a sufficient hypothesis from the exciting mechanism point of views, which is in this aspect much different from that with piezoelectric transducers. Spatially uniform pressure between the annulus gives the aperture function as $q(\sigma) = H(a - \sigma)$, where $H(r)$ is the Heaviside function. So $q'(\sigma) = -\delta(\sigma - a)$, where $\delta(r)$is the Dirac delta function. The final annuli field pressure expression for the annular superposition method could be derived as below:

$$P(r,z;\omega) = \frac{\rho c_0 \nu}{\pi} \int_b^a \delta(\sigma - a)\sigma \int_0^\pi \frac{rcos\psi - \sigma}{r^2 + \sigma^2 - 2\sigma r cos\psi} \times (e^{-j\omega\sqrt{r^2+\sigma^2-2\sigma r cos\psi+z^2}/c_0} - e^{-j\omega z/c_0}) d\psi d\sigma \tag{A.5}$$

The double integral expression in Equation A.5 gives the acoustic pressure distribution produced by an annular element whose inner radius is b and outer radius is a. As a specific case of annular element, the acoustic pressure field could be deduced for a circular element through assign $b = 0$ in Equation A.5, which will go back to Equation 1.1 and Equation 1.4.

Appendix B

2D Rayleigh integration method and 2D hybrid model

Corresponding to the 3D situation of RIM model, its 2D case formula will be deduced from 3D RIM under Hankel function approximations. This 2D RIM will be a part of the 2D RIM-FEM-RIM hybrid model. This hybrid model takes advantages both from the analytical integration models and from the FE model to simplify the calculation time consuming and demonstrate the validity to extend this method to 3D situations.

B.1 Rayleigh Integral reduction from 3D to 2D model

A 2D simplification form of the Rayleigh integration is now derived for its singular integration and easy programming. For the bi-dimensional plane wave propagation, a 2D Cartesian coordinate may be considered to simplify the problem and integration dimension. Therefore the y coordinate axis in Figure 3.3 is independent with the problem solved in bi-dimensional wave propagation problem. That requires the 2D transducer/plate is long enough comparing to the wave length in air.

Following the Rayleigh integration for 3D situation as shown in the previous section, the free-space Green's function in the bi-dimensional case is:

$$g(|\boldsymbol{r}-\boldsymbol{r_0}|) = -\frac{1}{4} j H_0^{(2)}(k\,|\boldsymbol{r}-\boldsymbol{r_0}|) \tag{B.1}$$

where $H_0^{(2)}$ is the zero-order Hankel function of the second kind. The Hankel function in first term approximation (see Appendix C) leads to:

$$g(|\boldsymbol{r}-\boldsymbol{r_0}|) \approx -\frac{j}{4}\left(\frac{2j}{k\pi\,|\boldsymbol{r}-\boldsymbol{r_0}|}\right)^{1/2} e^{-jk|\boldsymbol{r}-\boldsymbol{r_0}|} \tag{B.2}$$

The normal derivative of this function is:

$$\frac{\partial g(|\boldsymbol{r}-\boldsymbol{r_0}|)}{\partial n(\boldsymbol{r_0})} \approx \frac{k}{4}\left(\frac{2j}{\pi k\,|\boldsymbol{r}-\boldsymbol{r_0}|}\right)^{1/2} e^{-jk|\boldsymbol{r}-\boldsymbol{r_0}|} cos(\boldsymbol{n}, \boldsymbol{r}-\boldsymbol{r_0}) \tag{B.3}$$

$$= jkg(|\boldsymbol{r}-\boldsymbol{r_0}|)cos(\boldsymbol{n}, \boldsymbol{r}-\boldsymbol{r_0})$$

The coordinate system for 2D cases is shown in Figure B.1, where an integration element dl is on the radiating plane. In this situation, the integration limit is from $x = a$ to $x = b$. A 2D observation point $M(z, x)$ is at the distance $s = |\boldsymbol{r} - \boldsymbol{r_0}|$ away and in the angle $cos(\theta) = cos(\boldsymbol{n}, \boldsymbol{r} - \boldsymbol{r_0})$ from the radiated element. In this coordinate the y direction represents the very large extent of the transducer and of the plate.

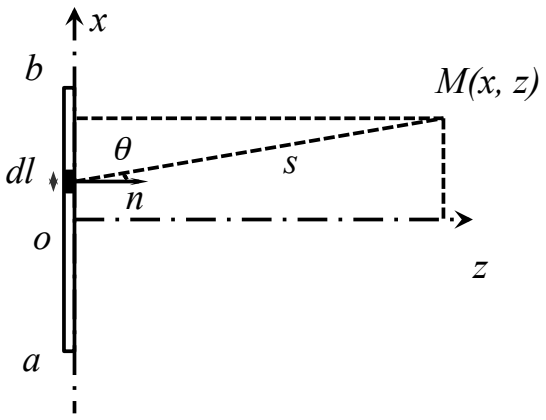

Figure B.1. 2D Cartesian coordinate system for Rayleigh integration.

The analytical solution for an acoustic transducer in 2D spatial condition could be expressed as a function of the coordinate (x, z), and can be expressed as following [71, 93, 117],

$$\begin{cases} p(x,z) = \displaystyle\int_a^b \left.\frac{\partial p}{\partial z}\right|_{z=0} \frac{e^{-jks}}{\sqrt{s}}\left[jk(1+\frac{z}{s})+\frac{z}{s^2}\right] dl \\ \left.\dfrac{\partial p}{\partial z}\right|_{z=0} = \rho\omega^2\, u|_{z=0} \\ s = |\boldsymbol{r}-\boldsymbol{r_0}| = \sqrt{z^2+(x-l)^2} \end{cases} \tag{B.4}$$

where a harmonic wave is considered to satisfy this approximation integral expression. u is the modulus of normal displacement at the active surface of the transducer or solid plate back surface, s is the distance from the source point to the observation point, and k is the wave number in fluid medium where the solid surface radiates its acoustic field. This equation will be used further down to be part of the 2D hybrid model for simulating the plate through-transmission inspection NDT system.

B.2 2D hybrid model for air-coupled plate inspection

This 2D RIM model will combine with the FE model to compose a full 2D hybrid air-coupled plate inspection model. The diagram of this 2D RIM-FEM-RIM hybrid model is shown in Figure B.2. The 2D acoustic field generated by a uniformed surface velocity piston transmitter will be calculated with 2D RIM model. Its ultrasonic pressure at the plate front surface will be extracted from 2D RIM prediction and imported to 2D FE solid plate model, which is a 2D plate FE model with free stress boundary at back surface and absorbing region at two ends to simulate a plate with infinity length. This solid FE model will be solved to obtain the displacement field in the plate. The back surface normal displacement is extracted, and used as the input of the 2D RIM for the prediction of the acoustic field at an air-coupled ultrasonic receiver. The final output signal is the integration of the ultrasonic pressure incident at the receiver surface. The 2D RIM-FEM-RIM hybrid model will be validated with the 2D air-solid coupling FE model.

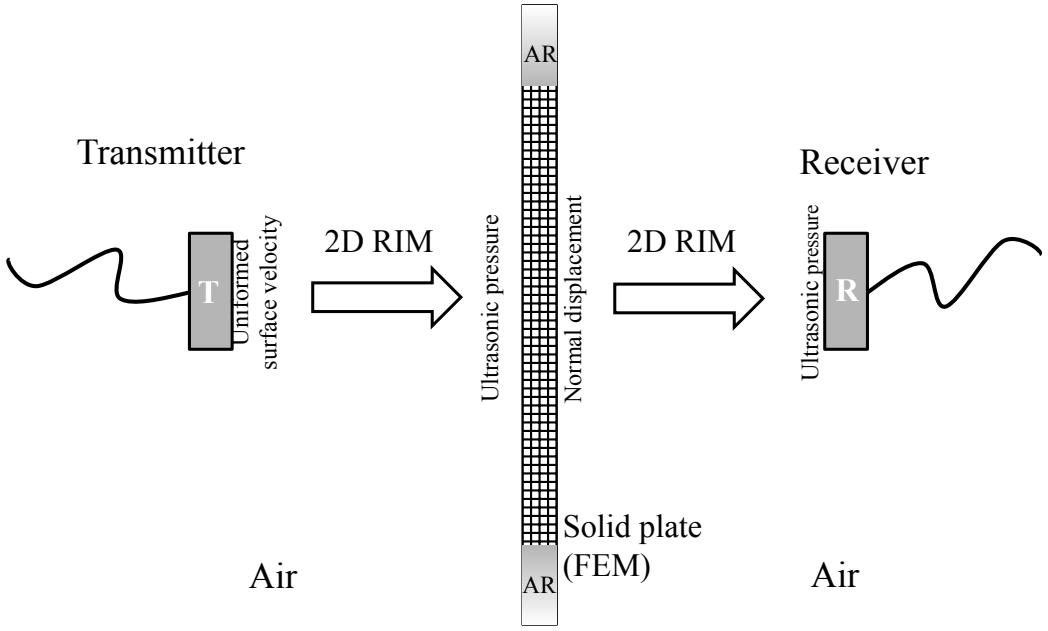

Figure B.2. Schematic diagram of 2D RIM-FEM-RIM hybrid model.

In this section, an overall air-solid coupling 2D FE model is built firstly to simulate the whole acoustic process from the emitter to the receiver. This 2D air-solid coupling FE model takes into account the air-solid coupling condition at the boundaries and will be used as the starting point to built the 2D hybrid model and to validate the simulation results from the 2D formula of RIM. Based on this 2D FE model, the air sub domains are removed from the FE model, the roles of which will be replaced by the analytical 2D RIM model. The remaining solid 2D FE model will become part of the hybrid model for the calculation of the acoustic wave in 2D plate. The input of the 2D FE model is the acoustic field pressure at the front surface boundary (calculated with 2D RIM), and the

output is the displacement at the back surface, which would be the input variable of the 2D RIM for the prediction of the acoustic field to the receiver.

B.2.1 2D air-solid coupling FE model

The overall air-solid coupling FE model is built for the through-transmission plate mode, as the configuration shown in Figure B.3. A rectangular domain is separated into three sub domains: air domain (transmitter side), solid plate and air domain (receiver side). The surrounding of the domains are set with a proper thickness of the absorbing regions to simulate the infinite space in those directions and to avoid reflections from outer boundaries.

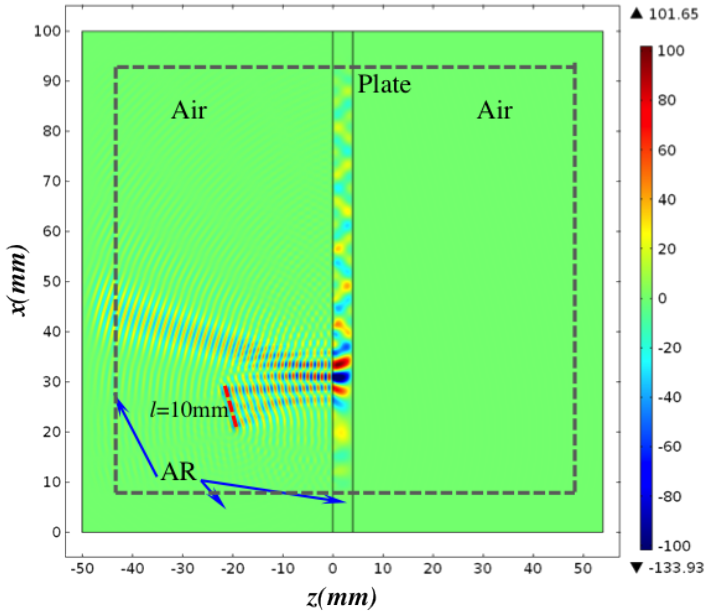

Figure B.3. Air-solid coupling 2D FE model for through-transmission plate inspection: the plate is surrounded by air domains and located between $z = 0mm$ and $z = 4mm$; the figure shows acoustic pressure in air (real part of complex pressure) and stress in solid.

A 2D transmitter with length $l = 10mm$ is modelled as a bulk force excitation defined within a narrow rectangular area in air domain. The width of this area is a wavelength of the acoustic wave in air, and length equals to the length of the transmitter, which is intended to be modelled. This 2D model is built in frequency domain, with a single frequency $f_0 = 250kHz$. The plate is perspex with thickness of $4mm$. Its mechanical properties are listed in Table 3.1.

Without loss of generality, the transducer is set with an oblique angle equal to 16.5° with respect to the normal plate. At the air-solid boundary, normal displacement and stress (*i.e.* acoustic pressure in air) are continuous. The absorbing regions are set around air domains and solid ends, according to the method which has been presented in Chapter 1.

The 2D Comsol [78] PDE formalism is shown in the following Equation B.5.

$$\begin{cases} -\nabla \cdot (c\nabla u) + au = f & in \quad \Omega \quad \text{(PDE)} \\ \boldsymbol{n} \cdot (c\nabla u) = g & on \quad \partial\Omega \quad \text{(Neumann condition)} \\ hu = r & on \quad \partial\Omega \quad \text{(Dirichlet condition)} \end{cases} \tag{B.5}$$

In air domain, the coefficient could be set as following:

$$\begin{aligned} c &= K_f \\ a &= -\rho\omega^2 \\ f &= \begin{cases} F & in \quad \text{Transmitter side} \\ 0 & in \quad \text{Receiver side} \end{cases} \end{aligned} \tag{B.6}$$

in which F is the bulk force imposed at the transmitter side air domain: bulk force is defined in a l-length and a wave length width narrow rectangular area; the value of F is prescribed to 0 at the other area of the air domain. And in 2D homogeneous solid, the PDE expression depends on space variables x_1 and x_2, which in our case, the variables are the coordinate variables (z, x): $x_1 \to z, x_2 \to x$. The displacement vector $\boldsymbol{u}$ contains two independdent component $\boldsymbol{u} = (u, v)^T$, where u is the displacement component along $x_1 = z$ and v is that along $x_2 = x$. Thus, both coefficients c and a in Equation B.5 are 2×2 matrices which could be presented as: $c = \begin{pmatrix} c_{11} & c_{12} \\ c_{21} & c_{22} \end{pmatrix}$, and $a = \begin{pmatrix} a_{11} & a_{12} \\ a_{21} & a_{22} \end{pmatrix}$. Generally, each components may be a matrix according to the number of dimensions and variables being solved. Associated with the relations for dynamic equilibrium and boundary conditions, the coefficients formalism [118] can be identified as:

$$\begin{aligned} c_{11} &= \begin{pmatrix} C_{1111} & C_{1121} \\ C_{1211} & C_{1221} \end{pmatrix} \quad c_{12} = \begin{pmatrix} C_{1112} & C_{1122} \\ C_{1212} & C_{1222} \end{pmatrix} \\ c_{21} &= \begin{pmatrix} C_{2111} & C_{2121} \\ C_{2211} & C_{2221} \end{pmatrix} \quad c_{22} = \begin{pmatrix} C_{2112} & C_{2122} \\ C_{2212} & C_{2222} \end{pmatrix} \\ a &= \begin{pmatrix} -\rho\omega^2 & 0 \\ 0 & -\rho\omega^2 \end{pmatrix} \end{aligned} \tag{B.7}$$

For orthotropic materials and when C_{ij} are expressed in the axis of symmetry, the non-zero elastic constants for 2D problem are given: $C_{11}, C_{22}, C_{12}, C_{66}$. Therefore, the coefficients c_{ij} could be written as:

$$\begin{aligned} c_{11} &= \begin{pmatrix} C_{11} & 0 \\ 0 & C_{66} \end{pmatrix} \quad c_{12} = \begin{pmatrix} 0 & C_{12} \\ C_{66} & 0 \end{pmatrix} \\ c_{21} &= \begin{pmatrix} 0 & C_{66} \\ C_{12} & 0 \end{pmatrix} \quad c_{22} = \begin{pmatrix} C_{66} & 0 \\ 0 & C_{22} \end{pmatrix} \end{aligned} \tag{B.8}$$

Considering the stiffness matrix is symmetric, so $C_{21} = C_{12}$. Then for isotropic solid, other symmetric rule would be considered: only two independent variables could fully express the stiffness matrix, the component C_{11} and C_{66} could be selected as the main constants, so that: $C_{22} = C_{11}$, $C_{12} = C_{11} - 2C_{66}$.

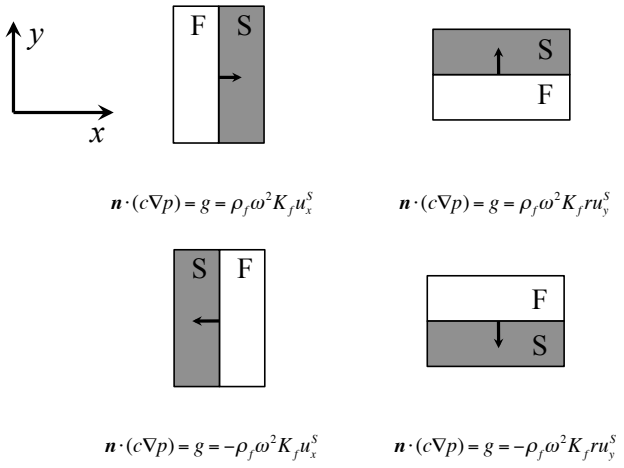

Figure B.4. 2D boundary conditions from fluid in air-solid coupling FE model.

For 2D air-solid-air sub-domains, the air-solid boundary conditions are similar to Equation 1.28 and Equation 1.30. So boundary conditions from fluid gives the Neumann condition as follows:

$$\boldsymbol{n} \cdot (c\nabla p) = g = \rho_f \omega^2 K_f \boldsymbol{n} \cdot \boldsymbol{u}^s \tag{B.9}$$

where $\boldsymbol{n}$ is the unit vector pointing from the solid to the fluid domain, and $\boldsymbol{u}^s$ is the displacement vector of the solid at the boundary. Boundary conditions from fluid are expressed in Figure B.9.

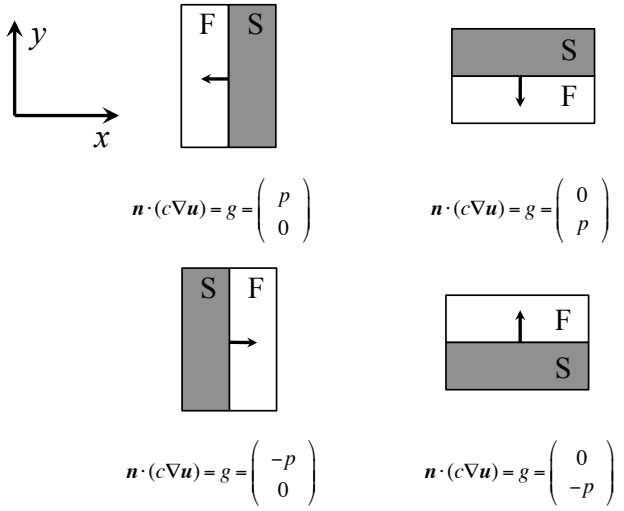

Figure B.5. 2D boundary conditions from solid in air-solid coupling FE model.

Boundary conditions from solid give the Neumann condition as follows:

$$\overline{\overline{\sigma}}\boldsymbol{n} = -p\boldsymbol{n} \tag{B.10}$$

The boundary conditions from solid are shown in Figure B.5.

The dimensions of the domains in this 2D air-solid coupling FE model are: air domain for air-coupled transmitter and receiver ($50mm \times 100mm$), solid plate domain ($4mm \times 100mm$). The model is set to be at single frequency of $f = 250kHz$. As the requirement of the improved VAR, the thickness of VAR in air is $1.5\lambda_a = 2.06mm$, and that in solid is $1.5\lambda_p = 16.17mm$. The model contains 251324 elements with free triangular meshing and 521880 of number of DOFs. It takes $34s$ with a stationary solver MUMPS.

B.2.2 2D RIM-FEM-RIM hybrid model building

The main idea of the 2D RIM-FEM-RIM hybrid model is to separate the air domain and solid domain in the air-solid coupling FE model (developed in the previous section) into three parts: acoustic field generated by transmitter (2D RIM); displacement field in 2D solid plate (FEM); acoustic field in air-coupled receiver (2D RIM). Since the very small wave length of acoustic wave in air, the calculation volume of elements / DOFs becomes large for air borne acoustic wave FE model, especially for model with long distance between transducer and tested sample. While the acoustic field in air at a given position can be directly calculated and predicted with RIM method directly in the hybrid model. Thus this 2D RIM-FEM-RIM hybrid model combines the integral and FE method to take both their advantages to facilitate the 2D through-transmission plate inspection cases.

B.2.2.1 2D RIM model for transmitter

The acoustic pressure in air generated by a 2D transmitter is calculated with the 2D RIM, which can predict the pressure at any position in air directly without involving the space between them.

The 2D transducer can be simulated by considering a line source with variety velocity at its surface. In this model, the 2D transmitter is modelled with a uniformed piston as presented in Equation B.4. Figure B.6(a) demonstrates the acoustic pressure amplitude generated by a line piston transmitter. Following the same conditions shown in Figure B.3, the acoustic field distribution of a line transmitter with $l = 10mm$ and extracted the complex acoustic pressure number along the air-plate interface, as the dashed line in Figure B.6(a). The pressure amplitude along the interface is shown in Figure B.6(b).

For an oblique incidence of the acoustic wave between the two media, *i.e.* air and solid, which has been shown in Figure B.7. The acoustic pressure reflection R_p and transmission T_p coefficients [97] are:

$$R_p = \frac{z_{2n} - z_{1n}}{z_{2n} + z_{1n}}, \qquad T_p = \frac{2z_{2n}}{z_{2n} + z_{1n}} \tag{B.11}$$

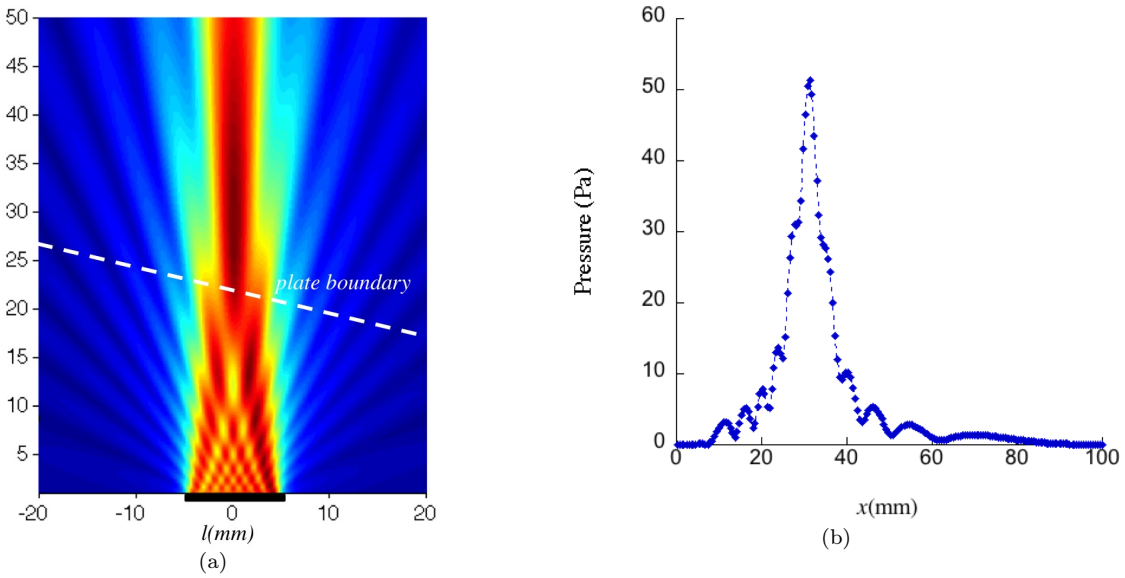

Figure B.6. 2D RIM model for a piston transmitter. (a): Ultrasonic pressure amplitude generated by a line transmitter with length $l = 10mm$, the dashed line across the field shows the air-plate interface position. (b): Acoustic pressure amplitude along air-plate interface.

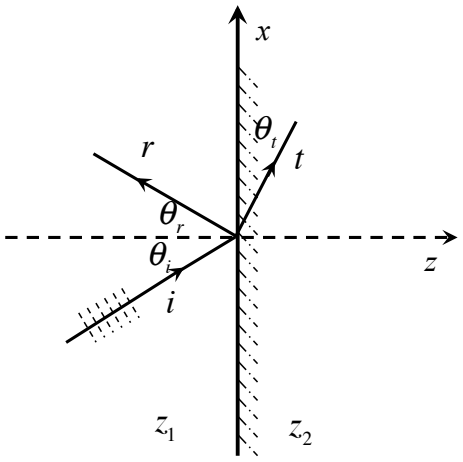

Figure B.7. Schematic of oblique incident of acoustic wave between two medium, *e.g.* air and solid.

where $z_{1n} = z_1/cos\theta_i$and $z_{2n} = z_2/cos\theta_t$are the ratio between the impedance and the incident angle and the transmission angle respectively. These two ratio can also be known as normal acoustic impedance. The particle velocity reflection R_v and transmission T_v coefficients are:

$$R_v = -\frac{z_{2n} - z_{1n}}{z_{2n} + z_{1n}}, \qquad T_v = \frac{2z_{1n}}{z_{2n} + z_{1n}} \tag{B.12}$$

Similar with the situation of normal incident, due to the very large impedance difference between them, *i.e.* $z_{2n} \gg z_{1n}$, the reflection and transmission coefficients becomes

$R_p \approx 1$ and $T_p \approx 2$. At the boundary, the particle velocity of incident wave and reflected wave are in reversed phase, while the acoustic pressures are in the same phase. In this approximative total reflective situation, the resultant velocity at air-solid boundary tends toward 0 while the resultant acoustic pressure tends to twice that of the incident wave, *i.e.* $p_b = 2p_{in}$, where p_b is the pressure at the boundary, p_{in} is the incident acoustic pressure shown in Figure B.6(b).

B.2.2.2 2D solid FE model

In the 2D hybrid model, the solid plate in FE model are placed in vacuum, which is set to be stress-free at its boundaries. In this situation, the vacuum is very close to that with the air-coupled, due to the very large impedance different between the air and solid. The normal stress in the solid, as those in 3D situations, can be written as Equation 3.17:

$$\overline{\overline{\sigma}}\boldsymbol{n} = -p_b\boldsymbol{n} = -2p_{in}\boldsymbol{n} \tag{B.13}$$

The schematic diagram of the implementation process of 2D RIM-FEM-RIM hybrid model is shown in Figure B.2. The complex pressure distribution in air along the boundary of the air-solid interface is regarded as the input of pressure force on the solid interface. Since the characteristic impedance between air and solid is quite different in order, $Z_{air} \ll Z_{solid}$ as shown in Table 3.1, the pressure input at the plate front interface is twice of the pressure in air [72]. Thus the the Neumann boundary condition term g has to be set equal to the normal stress, *i.e.*

$$\boldsymbol{g} = \begin{pmatrix} g_1 \\ g_2 \end{pmatrix} = \begin{pmatrix} 0 \\ -2p_{in} \end{pmatrix} \tag{B.14}$$

This boundary condition is applied at the front surface of the solid FE model. While the back surface of the solid plate is set to be stress free. The solid FE model is calculated with FE package COMSOL, with which the solid PDE module is introduced in this calculation following Equation B.7∼Equation B.8.

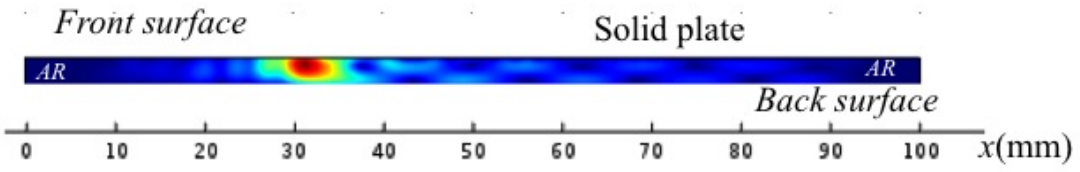

Figure B.8. Stress amplitude in plate calculated with FEM model by imposing the acoustic pressure in air input from 2D RIM model.

The normal stress along z in the solid is shown in Figure B.8. The solid FE model contains 8774 elements with free triangular meshing and the number of DOFs is 36314. So the time-consuming on the calculation of the model is $4s$, which is very fast and efficient than the full air-solid FE model.

B.2.2.3 2D RIM for receiver

The complex normal displacement at the plate back surface has extracted from the 2D solid FE model as the input data for 2D RIM model. By applying Equation B.4 to the displacement output from the FEM model, the pressure amplitude at the receiver side can be obtained and is shown in Figure B.9, which gives the predicted through-transmission acoustic field generated by the vibration at the back surface of the solid plate. By integrating the pressure at the receiver surface, the output signal from the transducer receiver can be obtained from this 2D RIM-FEM-RIM hybrid model.

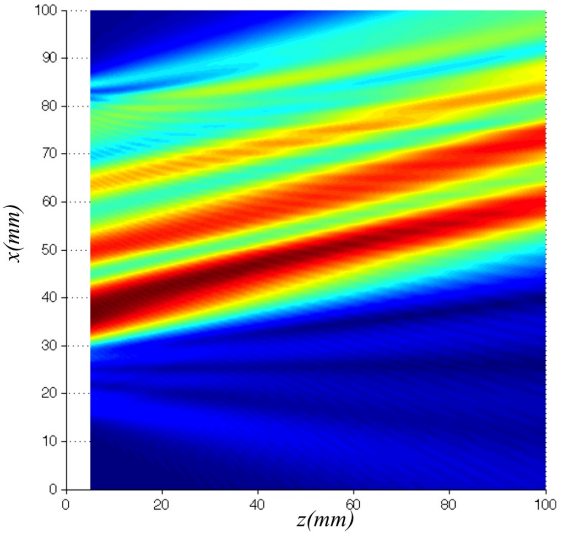

Figure B.9. Through-transmission ultrasonic pressure amplitude at the receiver side predicted by 2D RIM model.

B.2.3 2D RIM-FEM-RIM hybrid model validation

The validation of this 2D RIM-FEM-RIM hybrid model can be realised by comparing the predicted acoustic pressure at the receiver with that by the air-solid coupling FE model in Figure B.3. As the input of the FE models, the pressure (real part of complex pressure) along the plate front surface are shown in Figure B.11(a). The solid normal displacement at the back surface is shown in Figure B.11(b) (real part of complex normal displacement).

The comparison of the displacement at the plate back interface between two models is shown in Figure B.11(a), the distribution of which agrees well between these two models. The comparison of the pressure amplitude along direction normal to the plate between two models is shown in Figure B.11(b), which gives the predicted pressure calculated with the FE model and the hybrid model. The agreement between the pressure distribution predictions validates the availability of the RIM-FEM-RIM hybrid method.

This hybrid numerical method adopts the advantages of both analytical method in fluid and FEM in solid, thus avoid the time-consuming calculation of field in air comparing

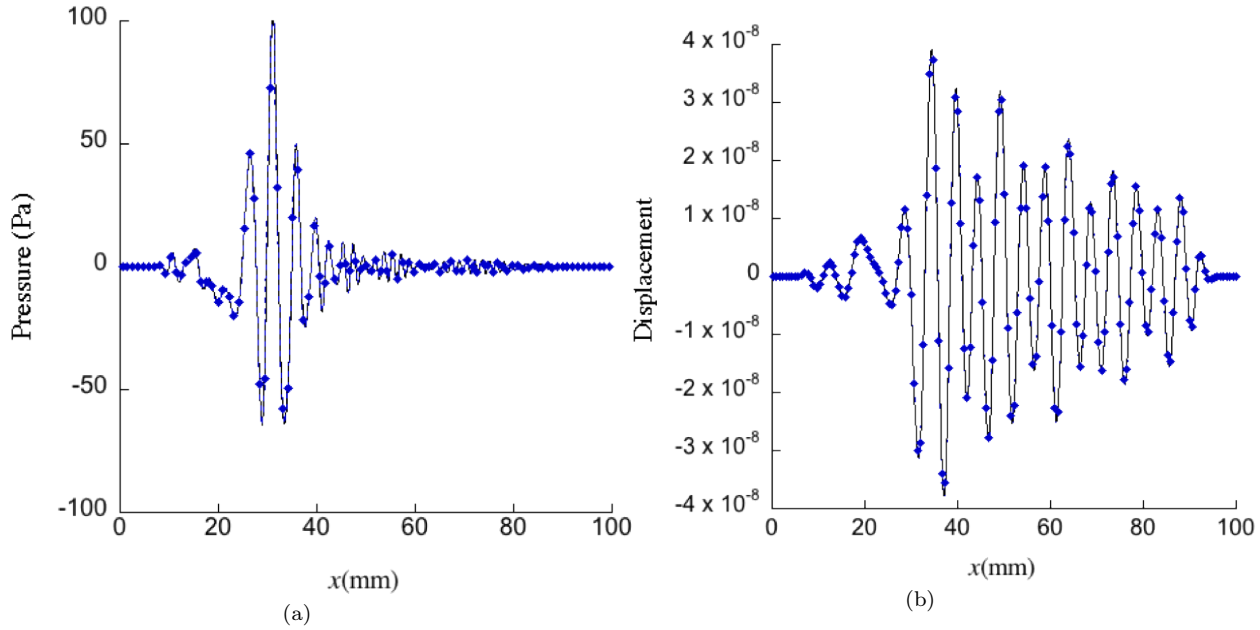

Figure B.10. Comparison of the pressure at front surface (a) and normal displacement at back surface (b) between the FEM model (dashed diamond −♦−) and RIM-FEM-RIM hybrid model (solid line −).

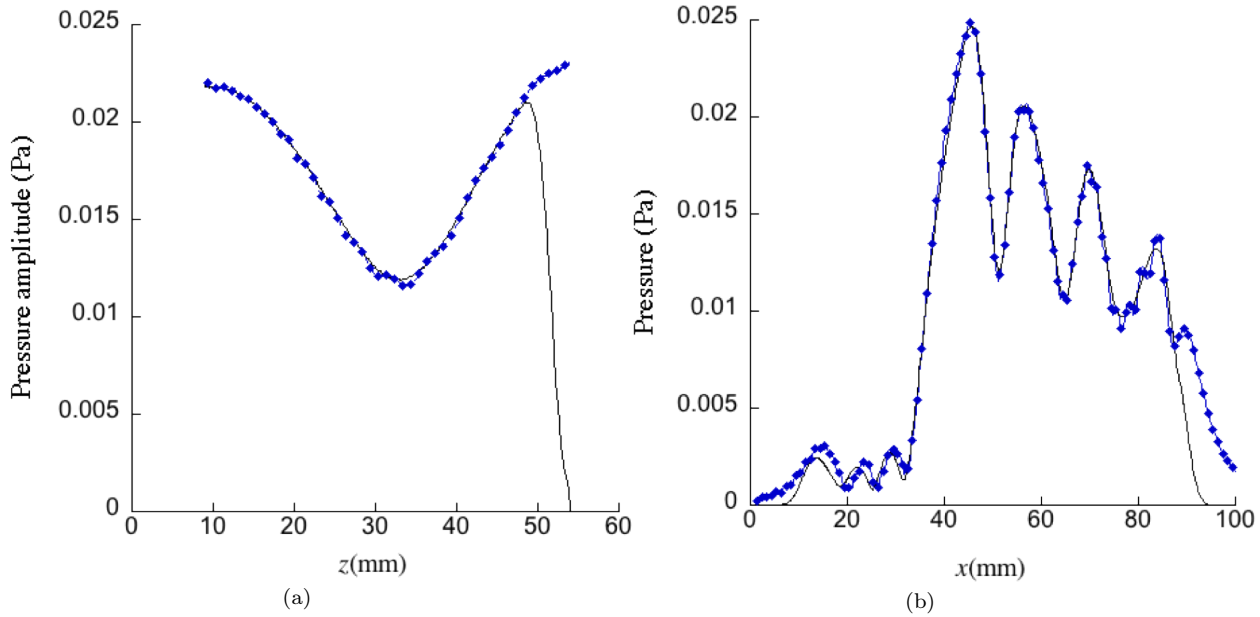

Figure B.11. Comparison of the the pressure amplitude on-axis (a) (along z direction from the centre point of plate) and along direction parallel to the plate at distance $z = 35mm$ (b) between the FEM model (dashed diamond −♦−) and RIM-FEM-RIM hybrid model (solid line −).

with the whole FE model. Since the wavelength of ultrasound in air is small even in lower frequency, the meshing step of FE model in air following the Shannon sampling theorem must be at least $\lambda_{air}/4 \sim \lambda_{air}/5$ for 2^{nd} order elements, to guarantee the precision of FE calculation. The total number of degrees of freedom(DoF) might be quite huge in air for large dimensional model. For 3D ultrasonic air-coupled problems, the calculation of ultrasonic NDT problem in air domain becomes impossible for the huge amount of DoF. Therefore this hybrid model is necessary and essential for the numerical calculation of air-coupled problems.

Appendix C

Hankel functions

Hankel function is a linearly independent solutions to Bessel's equation. There are two types of Hankel functions or known as Bessel function of the third kind, defined in Equation C.1. Usually, the Hankel functions are used to express outward and inward propagating cylindrical wave solutions of the cylindrical wave equation, respectively.

$$\begin{aligned} H_n^{(1)}(x) &= J_n(x) + jY_n(x) \\ H_n^{(2)}(x) &= J_n(x) - jY_n(x) \end{aligned} \tag{C.1}$$

where $J_n(x)$ is a Bessel function of the first kind and $Y_n(x)$ is a Bessel function of the second kind (also known as Neumann function). Hankel functions of the first kind and second kind can be represented as a contour integral using:

$$\begin{aligned} H_n^1(x) &= \frac{1}{i\pi}\int_0^\infty \frac{e^{(x/2)(t-1/t)}}{t^{n+1}}dt \\ H_n^2(x) &= \frac{1}{i\pi}\int_{-\infty}^0 \frac{e^{(x/2)(t-1/t)}}{t^{n+1}}dt \end{aligned} \tag{C.2}$$

The asymptotic forms for the Hankel functions are:

$$\begin{aligned} H_n^{(1)}(x) &\sim \sqrt{\frac{2}{\pi x}}e^{j(x-\frac{n\pi}{2}-\frac{\pi}{4})}, \quad -\pi < arg(x) < 2\pi \\ H_n^{(2)}(x) &\sim \sqrt{\frac{2}{\pi x}}e^{-j(x-\frac{n\pi}{2}-\frac{\pi}{4})}, \quad -2\pi < arg(x) < \pi \end{aligned} \tag{C.3}$$

The asymptotic forms for the Hankel functions permit us to write approximation forms for the complex terms under a constant phase angle $arg(x)$ within its limits.

Bibliography

[1] D. O. Thompson and D. E. Chimenti. *Quantitative Nondestructive Evaluation*. Springer, 2012.

[2] R. E. Green Jr. Non-contact ultrasonic techniques. *Ultrasonics*, 42(1–9):9–16, 2004.

[3] R. Hanke, T. Fuchs, and N. Uhlmann. X-ray based methods for non-destructive testing and material characterization. *Nuclear Instruments and Methods in Physics Research Section A: Accelerators, Spectrometers, Detectors and Associated Equipment*, 591(1):14–18, 2008.

[4] Y.-K. Zhu, G.-Y. Tian, R.-S. Lu, and H. Zhang. A review of optical NDT technologies. *Sensors*, 11(8):7773–7798, 2011.

[5] H. Shinoda, T. Nakajima, K. Ueno, and N. Koshida. Thermally induced ultrasonic emission from porous silicon. *Nature*, 400(6747):853–855, 1999.

[6] V. Berezhinski. Electromagnetic NDT state of the art : background and prospects. *Bulletin*, 78:55–65, 1999.

[7] J.-B. Ihn and F.-K. Chang. Pitch-catch active sensing methods in structural health monitoring for aircraft structures. *Structural Health Monitoring*, 7(1):5–19, 2008.

[8] M. Schickert, M. Krause, and W. Müller. Ultrasonic imaging of concrete elements using reconstruction by synthetic aperture focusing technique. *Journal of Materials in Civil Engineering*, 15(3):235–246, 2003.

[9] P. Purnell, T.H. Gan, D.A. Hutchins, and J. Berriman. Noncontact ultrasonic diagnostics in concrete: A preliminary investigation. *Cement and Concrete Research*, 34(7):1185–1188, 2004.

[10] B. Hosten and M. Castaings. Finite elements methods for modeling the guided waves propagation in structures with weak interfaces. *The Journal of the Acoustical Society of America*, 117(3):1108–1113, 2005.

[11] M. B. Drozdz. *Efficient finite element modelling of ultrasound waves in elastic media*. Ph.D. thesis, Imperial College London, 2008.

[12] N. Benech, S. Catheline, J. Brum, T. Gallot, and C.A. Negreira. 1-d elasticity assessment in soft solids from shear wave correlation: the time-reversal approach. *IEEE Transactions on Ultrasonics, Ferroelectrics and Frequency Control*, 56(11): 2400–2410, 2009.

[13] Zhao Y., Shen Z., Lu J., Ni X.-W., and Cui Y.-P. Numerical simulation of laser-induced rayleigh wave and its interaction with sub-surface void in solid. In *2010 Symposium on Photonics and Optoelectronic (SOPO)*, pages 1–6, 2010.

[14] M. Castaings, D. Singh, and P. Viot. Sizing of impact damages in composite materials using ultrasonic guided waves. *NDT & E International*, 46:22–31, 2012.

[15] J. H. Friedl, T. A. Gray, P. Khandelwal, and T. Dunhill. Ultrasonic phased array inspection of seeded titanium billet. *AIP Conference Proceedings*, 700(1):809–816, 2004.

[16] E. Jasiūnienė, R. Raišutis, R. Šliteris, A. Voleišis, and M. Jakas. Ultrasonic NDT of wind turbine blades using contact pulse-echo immersion testing with moving water container. 2008.

[17] M.-H. Lu, Y. P. Zheng, Q.-H. Huang, C. Ling, Q. Wang, L. Bridal, L. Qin, and A. Mak. Noncontact evaluation of articular cartilage degeneration using a novel ultrasound water jet indentation system. *Annals of Biomedical Engineering*, 37(1): 164–175, 2009.

[18] J.-P. Monchalin. Laser-ultrasonics: From the laboratory to industry. *AIP Conference Proceedings*, 700(1):3–31, 2004.

[19] H. K. Ann, H. M. Kim, K. Y. Jhang, I. K. Park, N. G. Kwag, and C. M. Lee. Detection of laser excited lamb wave using air-coupled transducer and wave mode identification using wavelet transform. *AIP Conference Proceedings*, 760(1):1018–1025, 2005.

[20] G. M. Graham and I. C. Ume. Automated system for laser ultrasonic sensing of weld penetration. *Mechatronics*, 7(8):711–721, 1997.

[21] H. Gao, S. M. Ali, and B. Lopez. Inspection of austenitic weld with EMATs. *AIP Conference Proceedings*, 1211(1):1175–1181, 2010.

[22] G. Villain, X. Derobert, O. Abraham, O. Coffec, O. Durand, L. Laguerre, and V. Baltazart. Use of ultrasonic and electromagnetic NDT to evaluate durability monitoring parameters of concretes. In *NDT & E 2009*, pages pp 343–348, France, 2009.

[23] B. Hosten and M. Castaings. Parabolic mirror and air-coupled transducer for multimodal plate wave detection. *AIP Conference Proceedings*, 657(1):1243–1250, 2003.

[24] L. Pizarro, D. Certon, M. Lethiecq, and B. Hosten. Airborne ultrasonic electrostatic transducers with conductive grooved backplates: tailoring their centre frequency, sensitivity and bandwidth. *Ultrasonics*, 37(7):493–503, 1999.

[25] T. E. G. Alvarez-Arenas. Acoustic impedance matching of piezoelectric transducers to the air. *IEEE Transactions on Ultrasonics, Ferroelectrics and Frequency Control*, 51(5):624–633, 2004.

[26] A. Safari and E. K. Akdoğan. *Piezoelectric and Acoustic Materials for Transducer Applications*. Springer, 2008.

[27] A. Leleux. *Contrôle non destructif de composites par ondes ultrasonores guidées, générées et détectées par multiéléments*. Ph.D. thesis N ° d'ordre: 4623, Université Bordeaux 1, 2012.

[28] J. D. Achenbach. Quantitative nondestructive evaluation. *International Journal of Solids and Structures*, 37(1–2):13–27, 2000.

[29] D. A. Hutchins, W. M. D. Wright, and D. W. Schindel. Ultrasonic measurements in polymeric materials using air-coupled capacitance transducers. *The Journal of the Acoustical Society of America*, 96(3):1634–1642, 1994.

[30] W. A. Grandia and C. M. Fortunko. NDE applications of air-coupled ultrasonic transducers. In *1995 IEEE Ultrasonics Symposium, 1995. Proceedings*, volume 1, pages 697–709 vol.1, 1995.

[31] A. Neild, D.A. Hutchins, T.J. Robertson, L.A.J. Davis, and D.R. Billson. The radiated fields of focussing air-coupled ultrasonic phased arrays. *Ultrasonics*, 43(3): 183–195, 2005.

[32] L. Schmerr and J.-S. Song. *Ultrasonic nondestructive evaluation systems: models and measurements*. Springer, 2007.

[33] L. F. Brown. Design considerations for piezoelectric polymer ultrasound transducers. *IEEE Transactions on Ultrasonics, Ferroelectrics and Frequency Control*, 47 (6):1377–1396, 2000.

[34] G. Hayward and A. Gachagan. An evaluation of 1–3 connectivity composite transducers for air-coupled ultrasonic applications. *The Journal of the Acoustical Society of America*, 99(4):2148–2157, 1996.

[35] V. Bovtun, J. Döring, M. Wegener, J. Bartusch, U. Beck, A. Erhard, and V. Borisov. Air-coupled ultrasonic applications of ferroelectrets. *Ferroelectrics*, 370(1):11–17, 2008.

[36] W. Galbraith and G. Hayward. Development of a PVDF membrane hydrophone for use in air-coupled ultrasonic transducer calibration. *IEEE Transactions on Ultrasonics, Ferroelectrics and Frequency Control*, 45(6):1549–1558, 1998.

[37] G. Hayward, G. Benny, R. Banks, and W. Galbraith. The radiation field characteristics of piezoelectric polymer membrane transducers when operating into air. *IEEE Transactions on Ultrasonics, Ferroelectrics and Frequency Control*, 47(6):1438–1447, 2000.

[38] A. Gachagan, G. Hayward, S.P. Kelly, and W. Galbraith. Characterization of air-coupled transducers. *IEEE Transactions on Ultrasonics, Ferroelectrics and Frequency Control*, 43(4):678–689, 1996.

[39] O. Oralkan, A. S. Ergun, J. A. Johnson, M. Karaman, U. Demirci, K. Kaviani, T. H. Lee, and B. T. Khuri-Yakub. Capacitive micromachined ultrasonic transducers: next-generation arrays for acoustic imaging? *IEEE Transactions on Ultrasonics, Ferroelectrics and Frequency Control*, 49(11):1596–1610, 2002.

[40] M. Rafiq and C. Wykes. The performance of capacitive ultrasonic transducers using v-grooved backplates. *Measurement Science and Technology*, 2(2):168, 1991.

[41] M. I. Haller and B. T. Khuri-Yakub. A surface micromachined electrostatic ultrasonic air transducer. In *1994 IEEE Ultrasonics Symposium, 1994. Proceedings*, volume 2, pages 1241–1244 vol.2, 1994.

[42] T. J. Robertson, D. A. Hutchins, and D. R. Billson. Capacitive air-coupled cylindrical transducers for ultrasonic imaging applications. *Measurement Science and Technology*, 13(5):758, 2002.

[43] D. Tuzzeo and F. L. di Scalea. Noncontact air-coupled guided wave ultrasonics for detection of thinning defects in aluminum plates. *Research in Nondestructive Evaluation*, 13(2):61–77, 2001.

[44] A. Octavio, R. L. O'Leary, S. M. Whiteley, Ó. Martínez-Graullera, C. J. Martín-Arguedas, L. Gómez-Ullate, and F. M. de Espinosa. Air-coupled linear and sparse cMUT array manufactured using MUMPs process. *Microsystem Technologies*, 17 (10-11):1635–1644, 2011.

[45] D. Certon, F. Teston, and F. Patat. A finite difference model for cMUT devices. *IEEE Transactions on Ultrasonics, Ferroelectrics and Frequency Control*, 52(12): 2199–2210, 2005.

[46] O. Bou Matar, L. Pizarro, D. Certon, J. P. Remenieras, and F. Patat. Characterization of airborne transducers by optical tomography. *Ultrasonics*, 38(1):787–793, 2000.

[47] N. Sénégond, F. Teston, D. Royer, C. Meynier, and D. Certon. High voltage time domain response of cMUT membrane: Laser interferometry measurements. *Physics Procedia*, 3(1):1011–1016, 2010.

[48] M. Castaings and B. Hosten. Air-coupled measurement of plane wave, ultrasonic plate transmission for characterising anisotropic, viscoelastic materials. *Ultrasonics*, 38(1–8):781–786, 2000.

[49] W. Ke. *Simulation 3D de la génération et de la réception d'ondes guidées : application à la détection de défauts dans des structures composites.* Ph.D. thesis N° d'ordre: 3805, Université Bordeaux 1, 2009.

[50] K. K. Park and B. T. Khuri-Yakub. 3-d airborne ultrasound synthetic aperture imaging based on capacitive micromachined ultrasonic transducers. *Ultrasonics*, 53 (7):1355–1362, 2013.

[51] D. W. Schindel, D. A. Hutchins, and W. A. Grandia. Capacitive and piezoelectric air-coupled transducers for resonant ultrasonic inspection. *Ultrasonics*, 34(6):621–627, 1996.

[52] H. Carr, W. S. H. Munro, M. Rafiq, and C. Wykes. Developments in capacitive transducers. *Nondestructive Testing And Evaluation*, 10:3–13, 1992.

[53] D. W. Schindel and D. A Hutchins. Capacitance devices for the controlled generation of ultrasonic fields in liquids. In *Ultrasonics Symposium, 1991. Proceedings., IEEE 1991*, pages 301–304 vol.1. IEEE, 1991.

[54] M. J. Anderson. Broadband electrostatic transducers: Modeling and experiments. *The Journal of the Acoustical Society of America*, 97(1):262–272, 1995.

[55] C. Biateau, B. Hosten, and D. Roziere. Measurement of air-coupled transducer characteristics for ultrasonic non-destructive evaluation. *AIP Conference Proceedings*, 615(1):921–928, 2002.

[56] D. W. Schindel, A. G. Bashford, and D. A. Hutchins. Focussing of ultrasonic waves in air using a micromachined fresnel zone-plate. *Ultrasonics*, 35(4):275 – 285, 1997.

[57] J. Song and D. E. Chimenti. Design, fabrication and characterization of a spherically focused capacitive air-coupled ultrasonic transducer. 2006.

[58] A. Octavio Manzanares and F. Montero de Espinosa. Air-coupled MUMPs capacitive micromachined ultrasonic transducers with resonant cavities. *Ultrasonics*, 52 (4):482–489, 2012.

[59] S. D. Holland, S. V. Teles, and D. E. Chimenti. Air-coupled, focused ultrasonic dispersion spectrum reconstruction in plates. *The Journal of the Acoustical Society of America*, 115(6):2866–2872, 2004.

[60] W. M. D. Wright and I. J. O'Sullivan. Ultrasonic tomographic imaging of air flow in pipes using an electrostatic transducer array. *AIP Conference Proceedings*, 657 (1):666–673, 2003.

[61] B. W. Drinkwater and P. D. Wilcox. Ultrasonic arrays for non-destructive evaluation: A review. *NDT & E International*, 39(7):525–541, 2006.

[62] D. M. Mills. Medical imaging with capacitive micromachined ultrasound transducer (cMUT) arrays. In *2004 IEEE Ultrasonics Symposium*, volume 1, pages 384–390 Vol.1, 2004.

[63] M. Akhnak, O. Martinez, L.G. Ullate, and F. Montero de Espinosa. 64 elements two-dimensional piezoelectric array for 3D imaging. *Ultrasonics*, 40(1–8):139–143, 2002.

[64] J. Mackerle. Finite-element modelling of non-destructive material evaluation, an addendum: a bibliography (1997–2003). *Modelling and Simulation in Materials Science and Engineering*, 12(5):799, 2004.

[65] A. Atalar. An angular spectrum approach to contrast in reflection acoustic microscopy. *Journal of Applied Physics*, 49(10):5130–5139, 1978.

[66] P. Wu, R. Kazys, and T. Stepinski. Analysis of the numerically implemented angular spectrum approach based on the evaluation of two-dimensional acoustic fields. part II. characteristics as a function of angular range. *The Journal of the Acoustical Society of America*, 99(3):1349–1359, 1996.

[67] N. Gengembre and A. Lhémery. Pencil method in elastodynamics: application to ultrasonic field computation. *Ultrasonics*, 38(1–8):495–499, 2000.

[68] P. Calmon, S. Mahaut, S. Chatillon, and R. Raillon. CIVA: an expertise platform for simulation and processing NDT data. *Ultrasonics*, 44, Supplement:e975–e979, 2006.

[69] K. Sha, J. Yang, and W.-S. Gan. A complex virtual source approach for calculating the diffraction beam field generated by a rectangular planar source. *IEEE Transactions on Ultrasonics, Ferroelectrics and Frequency Control*, 50(7):890–897, 2003.

[70] S. M. Kirkup. Computational solution of the acoustic field surrounding a baffled panel by the rayleigh integral method. *Applied Mathematical Modelling*, 18(7):403–407, 1994.

[71] B. Delannoy, H. Lasota, C. Bruneel, R. Torguet, and E. Bridoux. The infinite planar baffles problem in acoustic radiation and its experimental verification. *Journal of Applied Physics*, 50(8):5189–5195, 1979.

[72] M. J. Crocker. *Handbook of Acoustics*. John Wiley & Sons, 1998.

[73] B. B. Baker and E. T. Copson. *The Mathematical Theory of Huygens' Principle*. American Mathematical Society, 2003.

[74] M. Jessel. *Acoustique théorique*. Masson, 1973.

[75] R. Sanderson and S. Smith. The application of finite element modelling to guided ultrasonic waves in rails. *Insight*, 44(6):359–363, 2002.

[76] W. G. Strang and G. J. Fix. *An Analysis of the Finite Element Method*. Wellesley Cambridge Pr, 1973.

[77] I. Babuška, F. Ihlenburg, T. Strouboulis, and S. K. Gangaraj. A posteriori error estimation for finite element solutions of Helmholtz' equation. part I: the quality of local indicators and estimators. *International Journal for Numerical Methods in Engineering*, 40(18):3443–3462, 1997.

[78] COMSOL Inc. *Comsol Multiphysics: User's Guide*, 2013.

[79] W. Ke, M. Castaings, and C. Bacon. 3D finite element simulations of an air-coupled ultrasonic NDT system. *NDT & E International*, 42(6):524–533, 2009.

[80] B. Hosten and C. Biateau. Finite element simulation of the generation and detection by air-coupled transducers of guided waves in viscoelastic and anisotropic materials. *The Journal of the Acoustical Society of America*, 123(4):1963–1971, 2008.

[81] Y. Luo, H. Li, B. Q. Xu, and G. D. Xu. Spectral finite element method modeling of ultrasonic guided waves propagation in layered viscoelastic film/substrate materials. *Journal of Applied Physics*, 108(12):123505–123505–6, 2010.

[82] Y. Roh and B.T. Khuri-Yakub. Finite element analysis of underwater capacitor micromachined ultrasonic transducers. *IEEE Transactions on Ultrasonics, Ferroelectrics and Frequency Control*, 49(3):293–298, 2002.

[83] S. V. Tsynkov. Numerical solution of problems on unbounded domains. a review. *Applied Numerical Mathematics*, 27(4):465–532, 1998.

[84] G. R. Buchanan and M. Sallah. Some simplified methods for infinite elements. *Computational Mechanics*, 6(3):167–172, 1990.

[85] M. Castaings, C. Bacon, B. Hosten, and M. V. Predoi. Finite element predictions for the dynamic response of thermo-viscoelastic material structures. *The Journal of the Acoustical Society of America*, 115(3):1125–1133, 2004.

[86] J.-P. Berenger. A perfectly matched layer for the absorption of electromagnetic waves. *Journal of Computational Physics*, 114(2):185–200, 1994.

[87] T. Hagstrom. Radiation boundary conditions for the numerical simulation of waves. *Acta Numerica*, 8:47–106, 1999.

[88] W. L. Meyer, W. A. Bell, B. T. Zinn, and M. P. Stallybrass. Boundary integral solutions of three dimensional acoustic radiation problems. *Journal of Sound and Vibration*, 59(2):245–262, 1978.

[89] Mathworks. Matlab, 2013. URL `http://www.mathworks.fr/`.

[90] Avakas, 2013. URL `http://www.mcia.univ-bordeaux.fr/`.

[91] J. A. Archer-Hall, A. I. Bashter, and A. J. Hazelwood. A means for computing the kirchhoff surface integral for a disk radiator as a single integral with fixed limits. *The Journal of the Acoustical Society of America*, 65(6):1568–1570, 1979.

[92] D. A. Hutchins, H. D. Mair, P. A. Puhach, and A. J. Osei. Continuous-wave pressure fields of ultrasonic transducers. *The Journal of the Acoustical Society of America*, 80(1):1–12, 1986.

[93] M. Masmoudi. *Modélisation de la propagation d'ondes guidées, générées et détectées par transducteurs ultrasonores à couplage air : Application au CND de structures aéronautiques composites.* Ph.D. thesis N° d'ordre: 4483, Université Bordeaux 1, 2012.

[94] R. J. McGough, T. V. Samulski, and J. F. Kelly. An efficient grid sectoring method for calculations of the near-field pressure generated by a circular piston. *The Journal of the Acoustical Society of America*, 115(5):1942, 2004.

[95] I. N. Bronshtein, K. A. Semendyayev, Gerhard Musiol, and Heiner Mühlig. *Handbook of Mathematics.* Springer, 2007.

[96] T. Pritz. Frequency power law of material damping. *Applied Acoustics*, 65(11): 1027–1036, November 2004.

[97] P. M. Morse and K. U. Ingard. *Theoretical acoustics.* Princeton University Press, Princeton, N. J., 1986.

[98] H. E. Bass, L. C. Sutherland, A. J. Zuckerwar, D. T. Blackstock, and D. M. Hester. Atmospheric absorption of sound: Further developments. *The Journal of the Acoustical Society of America*, 97(1):680–683, 1995.

[99] A. Turo, J. Salazar, J. A. Chavez, H. B. Kichou, T. E. Gomez, F. Montero de Espinosa, and M. J. Garcia-Hernandez. Ultra-low noise front-end electronics for air-coupled ultrasonic non-destructive evaluation. *NDT & E International*, 36(2): 93–100, 2003.

[100] C. Bacon and J. Pouyet. *Mécanique des solides déformables*. Hermès Science Publications, Paris, 2000.

[101] B. Hosten, L. Moreau, and M. Castaings. Reflection and transmission coefficients for guided waves reflected by defects in viscoelastic material plates. *The Journal of the Acoustical Society of America*, 121(6):3409–3417, 2007.

[102] D. Appelö and G. Kreiss. A new absorbing layer for elastic waves. *Journal of Computational Physics*, 215(2):642–660, 2006.

[103] M. Kaltenbacher, M. Escobar, S. Becker, and I. Ali. Numerical simulation of flow-induced noise using LES/SAS and lighthill's acoustic analogy. *International Journal for Numerical Methods in Fluids*, 63(9):1103–1122, 2010.

[104] E. Bécache, A. S. Bonnet-Ben Dhia, and G. Legendre. Perfectly matched layers for the convected helmholtz equation. *SIAM Journal on Numerical Analysis*, 42(1): 409–433, 2004.

[105] P. Mattila, F. Tsuzuki, H. Vaataja, and K. Sasaki. Electroacoustic model for electrostatic ultrasonic transducers with v-grooved backplates. *IEEE Transactions on Ultrasonics, Ferroelectrics and Frequency Control*, 42(1):1–7, 1995.

[106] L. Pizarro. *Modélisation et développemnet de transducteurs ultrasonores capacitifs aériens à large bande*. Ph.D. thesis, Université François-Rabelais, Tours, France, 1999.

[107] D. R. Bacon. Primary calibration of ultrasonic hydrophone using optical interferometry. *IEEE Transactions on Ultrasonics, Ferroelectrics and Frequency Control*, 35(2):152–161, 1988.

[108] D. Royer and O. Casula. Quantitative imaging of transient acoustic fields by optical heterodyne interferometry. In *1994 IEEE Ultrasonics Symposium, 1994. Proceedings*, volume 2, pages 1153–1162 vol.2, 1994.

[109] S.-C. Wooh and Y. Shi. Optimum beam steering of linear phased arrays. *Wave Motion*, 29(3):245–265, 1999.

[110] Lecoeur electronics. Lecoeur, 2013. URL `http://www.lecoeur-electronique.com/`.

[111] E. G. Williams. *Fourier Acoustics: Sound Radiation and Nearfield Acoustical Holography.* Academic Press, 1999.

[112] P.-A. Gauthier, A. Berry, and W. Woszczyk. Sound-field reproduction in-room using optimal control techniques: Simulations in the frequency domain. *The Journal of the Acoustical Society of America*, 117(2):662–678, 2005.

[113] B. A. Auld. *Acoustic fields and waves in solids*, volume 1. Wiley New York, 1973.

[114] M. Castaings, B. Hosten, and T. Kundu. Inversion of ultrasonic, plane-wave transmission data in composite plates to infer viscoelastic material properties. *NDT & E International*, 33(6):377–392, 2000.

[115] J. L. Rose. *Ultrasonic Waves in Solid Media.* Cambridge University Press, 2004.

[116] J. F. Kelly and R. J. McGough. An annular superposition integral for axisymmetric radiators. *The Journal of the Acoustical Society of America*, 121(2):759–765, 2007.

[117] J. Assaad, J.-N. Decarpigny, C. Bruneel, R. Bossut, and B. Hamonic. Application of the finite element method to two-dimensional radiation problems. *The Journal of the Acoustical Society of America*, 94(1):562–573, 1993.

[118] L. Moreau. *Simulation de la diffraction d'ondes guidées ultrasonores par des défauts dans des plaques.* Ph.D. thesis N° d'ordre: 3543, Université Bordeaux 1, 2007.

Transducteurs ultrasonores capacitifs multiéléments à couplage air pour un contrôle non destructif à focalisation dynamique de matériaux – Modélisation, simulations numériques et expériences

Cette thèse porte sur le développement d'un traducteur ultrasonore multi-élément capacitif à couplage air (MEACUT) et son utilisation dans le domaine du contrôle non destructif (CND) de matériaux. Un modèle est employé pour simuler numériquement ce traducteur, et pour optimiser sa conception. Un prototype est ensuite fabriqué, puis caractérisé expérimentalement pour quantifier ses performances. Son originalité réside dans le fait qu'il possède une large bande passante en fréquence, tout en offrant la possibilité d'une focalisation variable. Ce prototype est alors employé pour la détection d'un endommagement causé par impact, dans une plaque composite. Il est clairement constaté que la résolution spatiale du procédé d'inspection employé (C-scan) est fortement améliorée grâce aux performances techniques du MEACUT. Enfin, un modèle hybride 3D est développé pour simuler, rapidement et intégralement, ce procédé de CND. Le très bon accord obtenu entre prédictions numériques et mesures expérimentales laisse présager que cet outil de simulation pourra servir à mettre au point d'autres expérimentations de CND, qui pourront à leur tour exploiter les performances du MEACUT.

Mots clés : Couplage air, Transducteur ultrasonique capacitif, Contrôle Non Destructif, Simulation par éléments finis, Méthode analytique, Modèle hybride, Plaque composite.

Multi-element air-coupled capacitive ultrasonic transducer with dynamic focusing for non-destructive testing of materials - modelling, numerical simulations and experiments

This thesis focuses on the development of a Multi-Element Air-coupled Capacitive Ultrasonic Transducer (MEACUT) and its use in the field of ultrasonic Non-Destructive Testing (NDT) of materials. An analytical Kirchhoff integation model (KIM) is developed and used to simulate the circular or annular transducers, and to optimize the dimension in order to obtain required acoustic field profile. An optimized annular MEACUT is then built and experimentally characterized to quantify its frequency response and dynamic focusing performance. Its turns out to be a broad frequency bandwidth while offering the possibility of dynamic focusing. This prototype is then used for the inspection of damage caused by impact in a composite plate. It is clearly found that the spatial resolution of the inspection process employed (C-scan) is greatly improved due to the local focusing performance MEACUT. Finally, a 3D hybrid model composed with Kirchhoff-FE-Rayleigh models is developed to simulate quickly and fully, the process of NDT. The good agreement obtained between numerical predictions and experimental measurements suggests that this simulation tool can be used to simulate and develop other NDT experiments, which may in turn exploit the performance of MEACUT.

Keywords: Air-coupled, capacitive ultrasonic transducer, Non-Destructive Testing, Finite Element Simulation, Analytical model, Hybrid model, Composite plate.